

UCSF

UC San Francisco Electronic Theses and Dissertations

Title

Flagellar length control in Chlamydomonas reinhardtii, experimental and mathematical approaches

Permalink

<https://escholarship.org/uc/item/62m0w561>

Author

Ludington, William B

Publication Date

2011

Peer reviewed|Thesis/dissertation

Flagellar length control in *Chlamydomonas reinhardtii*:
experimental and mathematical approaches

by

William B. Ludington

DISSERTATION

Submitted in partial satisfaction of the requirements for the degree of

DOCTOR OF PHILISOPHY

in

Cell Biology

in the

GRADUATE DIVISION

of the

UNIVERSITY OF CALIFORNIA, SAN FRANCISCO

Copyright 2011
by
William B. Ludington

Acknowledgements

I am grateful to many people for their time, patience, kindness and support.

Wallace Marshall's lab has been an ideal setting in which to do my graduate work. The intellectual freedom that Wallace provides broods a strong atmosphere of creativity and independence that is reflected in the breadth and depth of the science that comes out of his lab. Wallace gets excited about wild ideas, and as a result the lab is a very interesting place. For me these have been years where I have cherished the days, knowing that I would eventually have to move on.

Wallace doesn't so much teach us things as he does teach us to teach ourselves.

At times I have been stuck on what for me were hard problems, and at those times I wished that there was more direct mentoring. Eventually though, I have solved the problems on my own, and that has always been a reward worth waiting for.

Wallace's patience as a mentor allowed me these victories that built my confidence as a scientist, so I want to express my deep appreciation for that.

I am also grateful for Wallace's support in attending summer courses and conferences. The Santa Fe Institute's 2007 Complex Systems Summer School gave me one of the most influential intellectual experiences of my life. So I would also like to acknowledge the Santa Fe Institute and their NSF grant for putting on the course free of cost to students.

The Marshall lab has been a wonderful place to work because of the people here. When I came to the lab, I was drawn to the sense of excitement here that came from four girls (women?) who ran the show: Lani, Jessica, Kim and Elisa. They

set an awesome tone for the lab that has endured in their absence. As I listen to the Jingle Cats singing Meowy Christmas, I want you guys to know that I miss you and your legend lives on.

Scientifically, I have been very lucky to collaborate with Kim. She is a workhorse.

I also really appreciate the new side of the lab that the postdocs have cultivated. It has been one of collaboration and teamwork, and I have greatly benefitted from their mentoring. I would particularly like to thank Juliette and Susanne for their help in putting together manuscripts and presentations.

The UCSF community is a strong and friendly one and it's the reason I decided to come to school here. No place is more collegial. There are too many people to thank everyone, but I do in particular want to thank Liam, Onn, and Andrew for true, solid support through the good times and the rough times. I also want to thank Chris, Alex and Jason for including me in the crazy-science-offs over coffee. I wish we'd gotten to do some real science with the slime mold. It's still in spore form on my bench, so let me know.

Some people's families stress them out. Mine has been a great source of relaxation. Thank you all for lots of visits and lots of silliness. I also want to thank a lot of friends who are basically family at this point. You know who you are, and I feel really lucky that you're a part of my life. Apologies if you're actually reading this and wondering why you didn't get your name in here, but really, I thought you were above that. Yes, you in particular.

Many thanks also to my committee, Joe and Dyche. I have been very fortunate to have your guidance. You bring a lot of creativity and expertise everywhere you go, and I aspire to have a fraction of that one of these days.

Finally, I feel blessed with the love of the holy trinity: Dean Smith, Michael Jordan, and the Tarheel Spirit.

GO HEELS!

Acknowledgement of published material

Chapter 2 was published in similar form as “Automated analysis of intracellular motion using kymographs in 1, 2, and 3 dimensions” W.B. Ludington and W.F. Marshall. 2009. Three-Dimensional and Multidimensional Microscopy: Image Acquisition and Processing XVI. edited by Jose-Angel Conchello, Carol J. Cogswell, Tony Wilson, Proc. of SPIE Vol. 7184.

Abstract

Cells maintain organelles at precise size and orientation without a ruler or compass. In this dissertation I examine how these unintelligent, complex mixtures of molecules are able to correctly maintain the length of their cilia [or flagella] over a range of perturbing conditions. In other words, how do cells measure?

I treat the problem at three different spatial scales using the flagella of the proven model organism for mammalian cilia, *Chlamydomonas reinhardtii*.

Chlamydomonas cells possess a pair of ~12 micron flagella that they use for motility. The flagella are built and maintained from their distal tips by the active movement of precursor proteins to and from the cell body in the process known as intraflagellar transport (IFT). Using TIRF microscopy and computational methods, developed in Chapter 2, I found that the rate of IFT (amount of protein/second) sets the growth rate of the flagellum, as evidenced by higher IFT rate in lengthening flagella and lowered IFT rate in shortening flagella.

Furthermore, the IFT rate is set by the amount of IFT material localized at the flagellar base in a length-dependent manner. Surprisingly, I found that the dynamics of IFT particle entry into the flagellum are consistent with the mathematics of an avalanching system (Chapter 3).

From a whole cell systems perspective, it has been unclear whether cells have separate programs to directly shorten and lengthen their flagella or whether shortening and lengthening are part of an overall size control program. The main evidence for separate programs comes from experimental amputations of single

flagella in normal biflagellate cells and in cells that abnormally possess extra flagella. I repeated these classical experiments in more controlled conditions using microfluidic cell trapping and laser amputation of flagella (Chapter 4). I found by mathematical modeling that an overall size control program fits the data exceptionally well. The results indicate that flagella self-assemble but ultimately size is controlled through the cytoplasmic availability of precursor proteins. This finding provides a general model for size control in dynamic organelles. Using the mathematical model, I developed an experimental protocol to compute the turnover rate of proteins incorporated into the axoneme, the structural part of the flagellum (Chapter 5).

Finally, I derive quantitative versions of flagellar length control models and find evidence for a volumetric diffusion model, whereby organelle volume is sensed through a Ran-GTP gradient, such as is used to regulate nuclear import. This general model could apply to linear organelles like flagella as well as to spherical ones like the nucleus or non-uniformly shaped organelles such as the endoplasmic reticulum (Chapter 6).

Table of contents

Chapter 1	
Introduction.....	1
Chapter 2	
Automated analysis of intracellular motion using kymographs in 1, 2, and 3 dimensions.....	19
Chapter 3	
Avalanche-like behavior on ciliary length control.....	47
Chapter 4	
Microscopy methods for amputating single flagella from biflagellate <i>Chlamydomonas reinhardtii</i> cells and observing their subsequent recovery.....	103
Chapter 5	
A general model for dynamic organelle size control based on laser microsurgical perturbation studies of cilia.....	127
Chapter 6	
How a cell can measure length and volume.....	155
Appendix 1	
Changes in IFT speed do not affect flagellar length control.....	189

List of tables

Chapter 3

Table S1.....	99
---------------	----

Chapter 5

Table 1.....	186
--------------	-----

Table 2.....	187
--------------	-----

List of figures

Chapter 1

Figure 1.....	16
Figure 2.....	17
Figure 3.....	18

Chapter 2

Figure 1.....	39
Figure 2.....	40
Figure 3.....	41
Figure 4.....	42
Figure 5.....	43
Figure 6.....	44
Figure 7.....	46

Chapter 3

Figure 1.....	74
Figure 2.....	75
Figure 3.....	76
Figure 4.....	77
Figure S1.....	78
Figure S2.....	79
Figure S3.....	80
Figure S4.....	81
Figure S5.....	82
Figure S6.....	84
Figure S7.....	85
Figure S8.....	86

Chapter 4

Figure 1	119
Figure 2	120
Figure 3	121
Figure 4	122-123
Figure 5	124
Figure 6	125
Figure 7	126

Chapter 5

Figure 1	145-146
Figure 2	147
Figure 3	148
Figure 4	149
Figure 5	150
Figure 6	151
Appendix 1	152
Appendix 2	153

Chapter 6

Figure 1	182
Figure 2	183
Figure 3	184
Figure 4	185

This page intentionally left blank

Chapter 1: introduction

Avalanches, periodicity, and ciliary length control

A cell is a complex mixture of molecules. With no brain as guide, it assembles and maintains an elaborate spatial organization of organelles with precise size, shape and orientation. In some rudimentary way, this unintelligent collection of molecules is capable of counting and measuring. The subject of my dissertation is how the cell accomplishes the feat of measurement. I have focused my work on ciliary length control because this organelle reduces the spatial measurement problem to a linear one, with a structure readily quantifiable by traditional light microscopy.

Cilia are an apt example organelle for studying size control because of their prominence in human genetic disease. Cilia are the site of photoreceptor localization and essential for vision. They also regulate kidney function, transport mucous in the lungs and airways, and are essential for proper limb bud formation and neural tube development. Ciliary defects can thus be quite destructive, causing retinitis pigmentosa, polycystic kidney disease, many mucosal transport diseases in the lungs, as well as Bardet-Biedl syndrome, polydactyly, obesity, congenital heart defects, ectopic pregnancy, and mental retardation (Badano et al., 2006). The list is extensive because these organelles play a crucial role not only in transport of fluids but in cell-cell communication as well. Cell-cell communication requires the precise sensing of external stimuli, which the cell accomplishes by localizing receptors for those stimuli to the tip of the primary cilium, which is a non-motile version of the motile cilium. Many receptors, such as Sonic Hedgehog, rhodopsins, and a vast array of other G-protein coupled

receptors, localize to the primary cilium. Thus, without a cilium, the cell is not able to properly sense and respond to their external environment.

Due to its medical relevance, the study of mammalian ciliogenesis is a rapidly growing field. Because of its extremely high homology to mammalian motile cilia, easy culture, and robust genetics, the *Chlamydomonas reinhardtii* flagellum has become a prominent model system for studying ciliogenesis. Indeed, many of the most fundamental discoveries in this field have come from the cell biology, biochemistry, and genetics in *Chlamydomonas*, a biflagellate, green alga. The studies I present in this dissertation are all carried out in *Chlamydomonas* flagella, but the results presumably apply more broadly to mammalian motile and non-motile cilia.

Cilia and flagella are composed of 3 basic types of proteins, grouped according to their function (note: there is also a considerable amount of membrane, which could play an important role in length control, but I do not treat that here). (1) Structural components form a filamentous 9+2 (typically motile) or 9+0 (typically non-motile) radially symmetric geometry, which is known as the “axoneme.” The main structural feature, obvious in an electron microscopy cross section of the organelle, is 9 doublet microtubules arranged radially around a central structure with the plus (+) ends of the microtubules located at the distal tip of the organelle. In the 9+2 cilia, this central structure includes 2 singlet microtubules, absent in the 9+0 cilia. Normal *Chlamydomonas* flagella are of the motile 9+2 configuration, so I will use “flagella” to refer to these throughout the rest of this text, except where indicated. The other structural components include radial spoke

proteins, dyneins, monomeric actin, and many accessory proteins. The structural proteins must be transported to the flagellar tip for assembly. (2) This transport is accomplished by the second group of proteins, the intraflagellar transport (IFT) proteins (Figure 1). While the structural proteins reside in permanent positions within the axoneme, the IFT proteins are constantly moving. They accomplish this movement using motor proteins: heterotrimeric kinesin II to travel to the tip and cytoplasmic dynein I to travel to the base. The IFT proteins form stoichiometric, geometrically precise “particles”, also known as “trains” (Pigino et al., 2009). In addition to the motor proteins mentioned, there are around twenty IFT proteins that help form the IFT particles and hold the structural cargo on the journeys to and from the flagellar tip. (3) The last group of proteins are membrane proteins. They reside in the flagellum, are transported by IFT proteins, but do not play a prominent role in ciliogenesis, as far as it is currently known. However, there is a brief discussion of a possible ciliogenesis role for flagellar membrane channels in Chapter 5, which was proposed by Joel Rosenbaum.

Though the topic of this dissertation is flagellar growth, maintenance, and shortening, a lot is already known about the processes (Cole and Snell, 2009). First, a basal body must be docked at the plasma membrane in order for ciliogenesis to begin (Almuedo-Castillo et al., 2011). Next, all flagellar proteins must be produced in the cytoplasm. There is no protein production in flagella as there is in mitochondria and chloroplasts (Rosenbaum and Child, 1967). Third, flagellar proteins must localize to the basal body and be attached to IFT particles (Deane et al., 2001). Fourth, the IFT particles must traffic to the flagellar tip,

pulled by the heterotrimeric kinesin II (Kozminski et al., 1995). At the flagellar tip, the particles release their cargo and are remodeled (Iomini et al., 2001). The cargo of structural components is assembled onto the axoneme. IFT particles then reform in a different, smaller configuration, with the dynein motors attaching to the axoneme, and they return to the flagellar base, presumably carrying cargo (*reviewed by* Cole and Snell, 2009).

Though the assembly process depends on IFT, there is also known to be a disassembly process, which has been measured by shutting down the anterograde, kinesin-driven, transport using temperature-sensitive mutants (Adams et al., 1982; Huang et al., 1977; Marshall et al., 2005). Using these methods, the disassembly process was measured at roughly 0.02 microns per minute. However, the rate may be as high as ~0.5 microns per minute, as it has been measured during flagellar resorption before mitosis (Parker, 2008). The disassembly rate has also been measured at ~0.4 microns per minute when cells are recovering from amputation of a single flagellum (Rosenbaum et al., 1969). As mentioned earlier, *Chlamydomonas* has two flagella. Rosenbaum *et al* in 1969 reported that amputation of a single flagellum of the pair resulted in shortening of the remaining flagellum at roughly 0.4 microns per minute until the two flagella became equal length (Figure 2). Thus, there may be a continuous disassembly process even when the flagella are at steady state length. The disassembly process would explain why there is continuous IFT traffic even at steady state length.

In proposing these ideas to explain flagellar length control, Marshall and Rosenbaum (Marshall and Rosenbaum, 2001) introduced the “balance point”

model, accounting for flagellar growth, maintenance, and shortening with a single mathematical formula. The main feature of the model is that the steady state flagellar length is determined by the interplay between the flagellar growth rate (due to anterograde IFT traffic) and the disassembly rate (due to passive breakdown of axoneme structure at the flagellar tip). Thus, at steady state length, the growth rate equals the disassembly rate. The main prediction of the model, that there is turnover of axonemal components even at steady state length, was confirmed by Marshall *et al* (Marshall et al., 2005) in *Chlamydomonas*, and had been shown previously by Stephens (Stephens, 1997; Stephens, 2000) for sea urchin motile cilia. Marshall *et al* (2001) found experimental evidence that the disassembly rate was constant over all flagellar lengths. Therefore, in order to modulate flagellar length, the cell must be able to change the intraflagellar transport rate (i.e. how many IFT particles per second are dumping cargo at the flagellar tip). Some sort of entry gate limits the injection of new particles into the flagellum (Dentler, 2005), therefore, the IFT rate is actually set by the injection rate. Chapters 1 and 2 of this dissertation treat the measurement of the injection rate and the analysis of how the injection process arises respectively.

Some controversy arose after Marshall *et al* (2001; 2005) proposed their model. They showed that the growth rate must decrease as a function of flagellar length and presented microscopy and western blot data that IFT content in the flagella agreed with this prediction of the model. However, Dentler (2005) presented experimental data that the frequency of IFT injection was roughly constant as a function of flagellar length. Marshall *et al* had guessed that the decrease in IFT

injection rate as a function of increasing flagellar length arose due to modulation of injection frequency, and Dentler (2005) showed this guess to be wrong.

However, Dentler's observation does not invalidate the balance point model. In order to test whether the IFT injection rate could indeed control flagellar length, I imaged the process by TIRF microscopy and quantified not only the injection frequency, but also the size of the injections. In work with Ben Engel in the Marshall lab, we published the initial observations (Engel et al., 2009) that injection size determined the flagellar growth rate. I then developed improved microscopy methods to standardize the IFT intensity quantification and computational methods to quantify the injection rate from IFT movies without observer bias. These methods were published in SPIE Microscopy 2009 conference proceedings (Ludington and Marshall, 2009) and appear as Chapter 1 in this dissertation. Further analysis of injection rate revealed that avalanche-like dynamics appear to control the injection rate. Rather than length control arising due to the regulation of each IFT particle entering the flagellum (Dishinger et al., 2010), length control occurs through regulation of the accumulation of IFT particles at the flagellar base. The complex injection dynamics observed occur due to avalanche-like dynamics (Bak, 1996) as IFT particles interact at the entry pore. This work is presented in Chapter 2 and it provides a new understanding of how the flagellar growth rate and IFT particle size are controlled.

Chapters 3, 4 and 5 treat length control at the level of the whole cell. There is still a raging debate on whether ciliogenesis, ciliary maintenance, and ciliary shortening are three distinct programs that are activated separately or whether

they are all part of a single program that is capable of three distinct behaviors depending on cellular conditions. I sought to understand the flagellar length control system as a whole using ordinary differential equations to describe the system and asking whether the model can explain all experimental observations. I first integrated the injection rate data into the mathematical model proposed by Marshall *et al* (2001; 2005) and added an equation to track a dynamic cytoplasmic pool of axonemal precursor material (Figure 3). These modifications run into the same problem as the original model: they fail to predict a behavior known as “overshoot.” They also fail to predict a finding by Baldwin *et al* (Baldwin *et al.*, 1984) that in cells with more than 2 flagella, the extra flagella do not respond to amputation of the other flagella.

To explain what is meant by “overshoot” and “failure to respond to amputation”, it is important to first explain the experimental approach used. One basic way to test a model that has a stable equilibrium is to perturb the system and ask whether the model predicts the same return to equilibrium as experiments. In the case of *Chlamydomonas* with its two flagella, the perturbation to the system is to amputate one flagellum from the pair, creating what is known as a “long-zero” cell (Figure 2). In the ensuing recovery to equilibrium, the long flagellum shortens at roughly 0.4 microns per minute as the amputated flagellum regenerates. When the flagella are roughly equal length, the shortening long flagellum begins to grow again at the same rate as the regenerating amputated flagellum. The growth rate decreases as the flagella become longer, up to the point when they reach steady state length, which is around 12 microns, and the growth rate has asymptotically

reached zero. That is the normal case. However, in the overshoot case, Rosenbaum *et al* (1969) reported that the long flagellum shortens to a length less than that of the regenerating amputated flagellum. Eventually, the flagella equilibrate lengths before returning to steady state length. The “overshoot” thus refers to “overshortening.”

In the case of the cells that have more than the normal 2 flagella, Baldwin *et al* (1984) noted that in *vfl3* cells, amputation of one or more flagella did not result in shortening of the remaining flagella, thus the “failure to respond to amputation”.

Marshall and Rosenbaum’s (2001) mathematical model only explains the “normal” case. Therefore I set out to study the overshoot behavior and the behavior of cells with more than 2 flagella. The methods and initial results for this study are described in Chapter 3. I collaborated with Linda Shi and Qingyuan Zhu of Michael Berns’ lab at UCSD using laser ablation to amputate flagella. The previous papers used squishing of cells between coverslips to pop off flagella. Laser ablation proved much less invasive for the cells. However, *Chlamydomonas* are highly motile, swimming on the order of 100 microns per second. In order to keep them still and healthy, I developed a microfluidic trapping chamber with the CellASIC company. The resulting chamber allows imaging of up to 100 cells for over 24 hours.

In Chapter 4, I present the experimental results and how they fit with the mathematical model. The experiments showed that the previously reported results might have been artifactual. In 100 amputations of normal wildtype cells, I

observed no overshoot. I also observed shortening in unamputated flagella in 5/5 *vf12* cells as well as in 2/2 incompletely divided wildtype cells that had 4 flagella each. These findings indicate that the model does indeed show all of the dynamics of wildtype cells. I then used the model to calculate the flagellar disassembly constant at 0.5 microns per minute. This result agrees with previous measurements of the disassembly rate in premitotic cells. It also indicates that a single program controls three behaviors currently thought to be controlled by distinct pathways, i.e. flagellar growth a.k.a. ciliogenesis, flagellar maintenance, and flagellar disassembly. The model also indicates a general size control system for dynamic organelles, whereby the organelle semi-autonomously self-assembles, but ultimate control over size rests with the cytoplasmic availability of precursor proteins.

Last, in Chapter 5, I propose a theoretical model by which the cell actually measures ciliary length. The model is based on a rather robust diffusion gradient and measures organelle volume rather than length specifically. It is thus generalizable to other organelles. I also derive mathematical versions of several other proposed models, including “time of flight,” “ion channels,” and constant injection rate. I compare the model predictions with experimental evidence of the IFT injection rate and conclude that the diffusion gradient gives the best agreement with experimental evidence. This model thus shows how an unintelligent bag of matter can solve the measurement problem in a general way.

Finally, there is a brief appendix, which explains why the popular technique of measuring IFT speed does not give a useful indication of ciliary defects. IFT

speed simply cannot affect growth rate, unless a very specific model (“time of flight”), which is statistically unlikely (discussed in Chapter 5), determines the accumulation of IFT material at the basal body based on the IFT speed.

References

- Adams, G.M., B. Huang, and D.J. Luck. 1982. Temperature-Sensitive, Assembly-Defective Flagella Mutants of CHLAMYDOMONAS REINHARDTII. *Genetics*. 100:579-586.
- Almuedo-Castillo, M., E. Saló, and T. Adell. 2011. Dishevelled is essential for neural connectivity and planar cell polarity in planarians. *PNAS*.
- Badano, J.L., N. Mitsuma, P.L. Beales, and N. Katsanis. 2006. The ciliopathies: an emerging class of human genetic disorders. *Annu Rev Genomics Hum Genet*. 7:125-148.
- Bak, P. 1996. How nature works: the science of self-organized criticality. Springer-Verlag, New York, NY.
- Baldwin, D.A., M.R. Kuchka, b. chojnacki, and J.W. Jarvik. 1984. Approaches to flagellar assembly and size control using stumpy- and short-flagella mutants of Chlamydomonas reinhardtii. *In* Molecular biology of the cytoskeleton. D.W.C. Gary G. Borisy, Douglas B. Murphy, editor. Cold Spring Harbor Laboratory, Cold Spring Harbor, New York. 245-255.
- Cole, D.G., and W.J. Snell. 2009. SnapShot: Intraflagellar transport. *Cell*. 137:784-784e781.
- Deane, J.A., D.G. Cole, E.S. Seeley, D.R. Diener, and J.L. Rosenbaum. 2001. Localization of intraflagellar transport protein IFT52 identifies basal body

transitional fibers as the docking site for IFT particles. *Curr Biol.* 11:1586-1590.

Dentler, W. 2005. Intraflagellar transport (IFT) during assembly and disassembly of *Chlamydomonas* flagella. *J Cell Biol.* 170:649-659.

Dishinger, J.F., H.L. Kee, P.M. Jenkins, S. Fan, T.W. Hurd, J.W. Hammond, Y.N.-T. Truong, B. Margolis, J.R. Martens, and K.J. Verhey. 2010. Ciliary entry of the kinesin-2 motor KIF17 is regulated by importin-beta2 and RanGTP. *Nat Cell Biol.* 12:703-710.

Engel, B.D., W.B. Ludington, and W.F. Marshall. 2009. Intraflagellar transport particle size scales inversely with flagellar length: revisiting the balance-point length control model. *J Cell Biol.* 187:81-89.

Huang, B., M.R. Rifkin, and D.J. Luck. 1977. Temperature-sensitive mutations affecting flagellar assembly and function in *Chlamydomonas reinhardtii*. *J Cell Biol.* 72:67-85.

Iomini, C., V. Babaev-Khaimov, M. Sassaroli, and G. Piperno. 2001. Protein particles in *Chlamydomonas* flagella undergo a transport cycle consisting of four phases. *J Cell Biol.* 153:13-24.

Kozminski, K.G., P.L. Beech, and J.L. Rosenbaum. 1995. The *Chlamydomonas* kinesin-like protein FLA10 is involved in motility associated with the flagellar membrane. *J Cell Biol.* 131:1517-1527.

- Ludington, W., and W. Marshall. 2009. Automated analysis of intracellular motion using kymographs in 1, 2, and 3 dimensions. *Proceedings of SPIE*. 7184.
- Marshall, W., and J. Rosenbaum. 2001. Intraflagellar transport balances continuous turnover of outer doublet microtubules: implications for flagellar length control. *Journal of Cell Biology*. 155:405-414.
- Marshall, W.F., H. Qin, M. Rodrigo Brenni, and J.L. Rosenbaum. 2005. Flagellar length control system: testing a simple model based on intraflagellar transport and turnover. *Mol Biol Cell*. 16:270-278.
- Parker, J. 2008. Co-ordinate regulation of cilia and the cell cycle in *Chlamydomonas reinhardtii*. *summit.sfu.ca*.
- Pigino, G., S. Geimer, S. Lanzavecchia, E. Paccagnini, F. Cantele, D. Diener, J. Rosenbaum, and P. Lupetti. 2009. Electron-tomographic analysis of intraflagellar transport particle trains in situ. *Journal of Cell Biology*. 187:135-148.
- Rosenbaum, J.L., and F.M. Child. 1967. Flagellar regeneration in protozoan flagellates. *J Cell Biol*. 34:345-364.
- Rosenbaum, J.L., J.E. Moulder, and D.L. Ringo. 1969. Flagellar elongation and shortening in *Chlamydomonas*. The use of cycloheximide and colchicine

to study the synthesis and assembly of flagellar proteins. *J Cell Biol.*
41:600-619.

Stephens, R.E. 1997. Synthesis and turnover of embryonic sea urchin ciliary
proteins during selective inhibition of tubulin synthesis and assembly. *Mol
Biol Cell.* 8:2187-2198.

Stephens, R.E. 2000. Preferential incorporation of tubulin into the junctional
region of ciliary outer doublet microtubules: a model for treadmilling by
lattice dislocation. *Cell Motil Cytoskeleton.* 47:130-140.

Figures

Figure 1: Intraflagellar transport cartoon

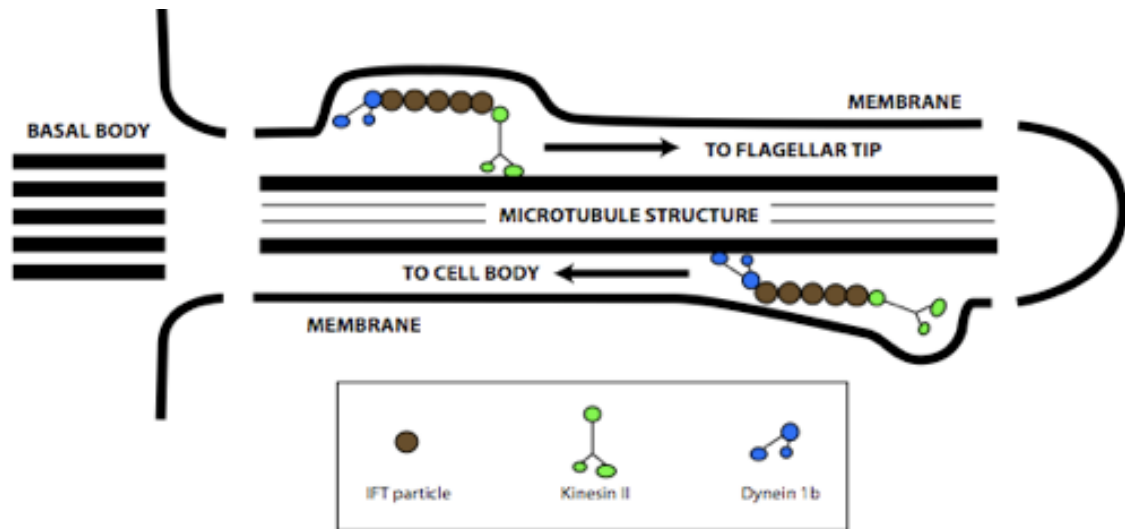


Figure 2: the long-zero response

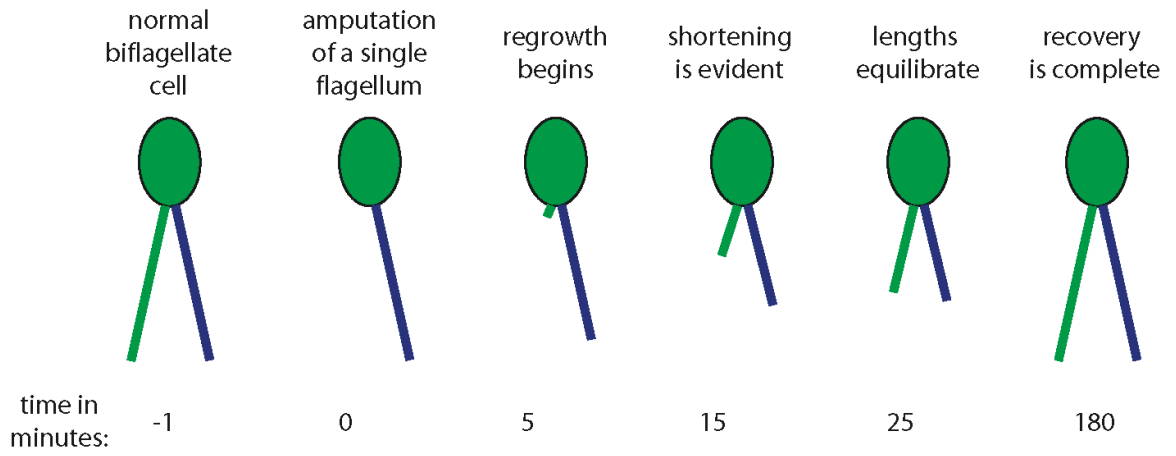
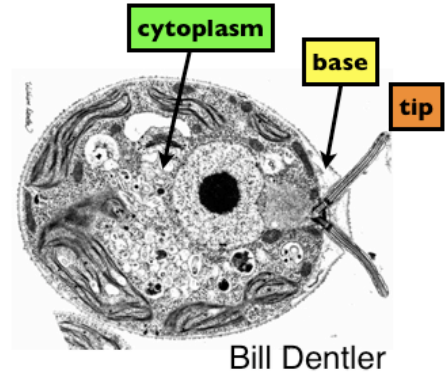
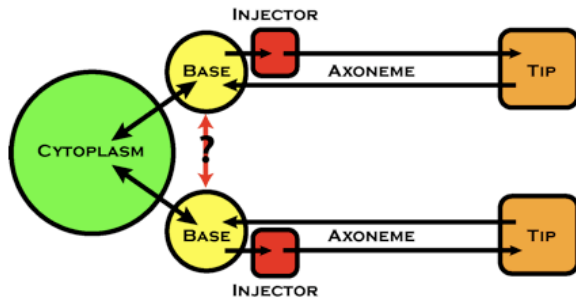


Figure 3: schematic upon which the mathematical modeling was based. Electron micrograph was produced by Bill Dentler.



Chapter 2

Automated analysis of intracellular motion using kymographs in 1, 2, and 3 dimensions.

Synopsis:

This chapter details the TIRF microscopy and automated computational kymograph analysis algorithms built to analyze intraflagellar transport in *Chlamydomonas reinhardtii*

Abstract:

In this paper we use kymographs and computational image processing to convert 3-D video microscopy data of intracellular motion into 1-D time series data for further analysis. Because many standard tools exist for time series analysis, this method allows us to produce robust quantitative results from otherwise visual data. The kymograph-based approach has an additional advantage over standard particle-tracking and flow-based image quantification algorithms in that we can average out camera noise over the spatial axis of the kymograph, allowing a higher gain setting and increased signal to noise. The method has the disadvantage that it removes all spatial information. For this reason we see this method as a complement to rather than a replacement of standard tracking algorithms.

The standard problem we are trying to address in our work is how fluorescent proteins in one cellular compartment are injected into another cellular compartment. The proteins travel at constant speed along a fixed, linear spatial path once they enter the second compartment, so a 2-D kymograph produced from a trace along this fixed, linear path will tell us about the injection history into this second compartment (Fig. 1).

Our algorithm works by first taking a Radon transform of the input 2-D kymograph. We next make a back projection of each projection from the Radon transform to make synthetic kymographs. The angle with the best correlation between the original kymograph and the back-projection determines the dominant speed of the moving particles as well as the angle of the 1-D projected time series.

Time series are then analyzed with standard tools to determine the peak size distribution, the peak interval distribution, the autocorrelation and the power spectrum.

1. INTRODUCTION

The kymograph or ‘wave graph’ is simply a time series recording of a process on the physical axes of space and time. Essentially, it provides a way to visually analyze the history of a process. The first kymographs were instruments used in medicine to record changes in a patient’s blood pressure in the 19th century¹.

More recently video kymography has been developed to apply the same concept to study larynx movement in a reference frame from a high speed camera². With recent advances in video microscopy, kymography has been applied to the study of intracellular movement as well³. While the visual features of a kymograph can reveal much about the study subject, often some quantification of the kymograph can reveal more subtle aspects of the underlying system. This quantification is typically carried out by a user, hand-tracing the features of the kymograph.

Two main problems arise when quantifying kymograph data in this manner: first, the user can exhibit a bias in determining which features to include and which to ignore. A single user can have a different bias on different days, and two users can easily have a different bias. Second, automated microscopes can easily produce more data than a user has time to quantify by hand. Thus there is a need for automated kymograph processing algorithms. An automated computational algorithm solves the first problem of user bias because it always exhibits the same bias on every dataset. The second problem of large datasets is a great benefit to an automated algorithm because it allows better statistical confidence in making observations.

In our work we examine the movement of fluorescently-labeled intraflagellar transport particles in live cells. Because these particles travel at roughly 2 microns per second, we need a frame rate of roughly 30 frames per second in order to accurately capture their movement. This introduces the problem of capturing enough light in a single frame in order to register the particle's location. Even using total internal reflection microscopy (TIRF⁴), which produces very high signal to noise, we have to use a high gain setting on our EMCCD camera in order to record particles at all. Thus we have a relatively high amount of noise in our data, which generally precludes the use of standard particle tracking algorithms, except in the case of the brightest particles. When we want to capture the full behavior of the system, we make a 2-D kymograph, because even the dim particles make traces that are detectable by eye. In order to accurately measure the intensity value of a single particle by this method, we draw a hand trace along the particle's path on the kymograph. Because measuring the intensity of a particle in one frame is highly inaccurate due to camera noise, we measure the average intensity along the trace, allowing us to substantially increase our signal to noise. Recently, we have begun examining the time interval distribution between particles (peak interval distribution) in order to investigate the mechanism governing their release from one cellular compartment into another. Calculating this distribution requires a large dataset, therefore, we have developed a computational algorithm for data extraction. Our method approximates the hand-tracing method by reducing the dimensions of the input kymograph from the 3D input movie (2 spatial dimensions and 1 time dimension) to the 1-D output time

series data that can be analyzed by standard methods⁵. The method we describe here requires hand tracing to reduce the 3-D input video to a 2-D kymograph but we are currently working on a computational approach to this step as well. In the body of this manuscript we detail the methods, discuss our approach and its performance, and demonstrate its outputs on a sample dataset.

2. METHODS

2.1 Imaging and initial kymograph generation

The analysis presented here utilizes kymographs generated by TIRF imaging of *Chlamydomonas reinhardtii* intraflagellar transport particles tagged with GFP (Fig. 1). Briefly, cells were adhered to glass coverslips, and time-lapse images were acquired on a Nikon TE2000-E inverted microscope using a through-the-objective TIRF system (100x 1.45NA) and NIS-Elements v2.3 at roughly 30 frames per second on a cooled Photometrics QuantEM:512SC EMCCD camera with linear gain. Controls for laser intensity show that some minor variation exists between days but that pixel intensity correlates with number of GFPs (data not shown). After imaging, kymographs were produced using 10 pixel width hand-traced line segments in Metamorph v7.5.1.0. Frame rate, pixel size, and flagellar length were recorded for each kymograph. Cell movement during imaging was removed using a cross-correlation function.

2.2 Kymograph processing algorithm

The kymograph processing algorithm (KPA) (Fig. 2; Fig. 3) takes as its input a cropped kymograph of a clear region of the flagellum at least 12 pixels wide and 170 pixels long (minimums: 1.3 microns by 5.3 seconds; means: 4 microns, 22 seconds, N=128). The algorithm outputs the particle injection time series based on anterograde

transport using a mean projection over the spatial axis of the kymograph along the angle of the particle traces. In order to find the angle of particle traces, the

algorithm takes advantage of the fact that all particles moving in the same direction in any given flagellum have the same speed.

The central feature of the algorithm is the Radon transform⁶, which is essentially an iterative projection through the image from every angle. In order to determine the angle with the best alignment, we first take the Radon transform (Fig. 3) of the input kymograph. This gives us a series of 1-dimensional projections as a function of the projection angle. We next make a back-projection of each angle's projected time series from the Radon transform, which gives us a synthetic kymograph (Fig. 3). We then find the correlation coefficient between the input kymograph and each back projection, giving us a correlation score for each rotation angle (Fig. 4a). The maximum score determines the best-fit rotation angle (Fig. 4a). Rotation angles that do not produce a correlation coefficient above $r=0.50$ are rejected from the analysis.

Alternately we use an orthogonal method to find the kymograph rotation angle (Fig 4b). The best fit rotation angle should produce the greatest difference between maxima and minima in the projection. In this method we deconstruct the projection at each angle from the Radon transform into peaks and troughs. The best angle maximizes the function $n*(p-t)$, where n is the number of peaks detected, p is the median peak height, and t is the median trough height. This function we use weights the difference between p and t by the number of peaks detected so that projection angles that detect few large peaks or many small peaks give a lower score than angles that detect an intermediate number of peaks with the greatest difference in peak height and peak trough in the projection. By this

dual approach we could reliably find the angle of rotation to create a projection aligned with the kymograph traces. However, for most datasets, we find the first method to be superior.

We calculate the detected speed of the kymograph traces by the tangent of the rotation angle multiplied by the frame rate and the pixel size. The projection is then converted into a time series using the frame rate to get the correct time scale. Linear interpolation resampling then standardizes the sample interval to 32 Hertz, which is greater than the camera speed. In this manner the injection time series are all calibrated to the same sampling rate.

2.3 Synthetic kymographs by back-projection of time series

We produce synthetic kymographs for comparison with the input kymographs by taking a back-projection of our time series. Essentially, this involves making a 2-D projection of the 1-D time series along the angle of the original projection. If there were no spatial variation in the original kymograph, this method would exactly reproduce the original input kymograph (see Fig. 3a).

2.4 Time series processing approach

For the IFT particle intensity, the local background makes a large contribution to the total intensity, therefore we used a multi-faceted approach to validate that the trends we observe in particle intensity are not indicative of background but rather of the actual anterograde IFT particles themselves. By examining the correlation between input kymographs and synthetic kymographs, we compared (1) absolute thresholding with adaptive thresholding and found that adaptive thresholding by

using a fraction of the time series mean as a cutoff threshold produces the most reliable results over a range of experiments. We compared (2) linear detrending with mean detrending and found that linear detrending does a better job of correcting for the trend in the time series because a decrease in intensity due to photobleaching accounts for the largest trend. We also compared (3) global minimum subtraction with local minimum subtraction and found that because local background due to errors in kymograph tracing and flagellar movement out of the trace region account for the majority of background, local minimum subtraction produces better results. Our final algorithm uses an adaptive threshold, linear detrending, and local background subtraction (see ‘Time series processing parameters’). We specify the adaptive threshold by the time series mean divided by a fixed parameter. In order to set this adaptive threshold parameter, we took advantage of the fact that the TIRF microscopy technique produces an exponential illumination field. Because the particles we are imaging tend to be distributed uniformly through the illumination field, we expect to see an exponentially distributed peak size distribution when we look at all injection sizes from our time series. We therefore examined a range of threshold parameters (mean/parameter) and found that the value 2.0 maximizes the fit of the injection size distribution to an exponential distribution (Fig. 5).

2.5 Time series processing parameters

Each time series is pre-processed using the above-mentioned steps prior to data extraction. In stepwise fashion, we remove single time step fluctuations using a median filter (3 pixel window width), use linear detrending, use a local minimum

filter (1.09 s window width, which is the median injection interval), and finally use a moving average filter (0.38 s window width; determined by correlation analysis of back-projections). The use of these processing algorithms is crucial to accurately determining the peak interval because minor background fluctuations that produce false peaks will tend to cause the true peak intervals to be broken into smaller intervals.

2.6 Injection area versus injection height

We next analyze the time series to determine the peak heights and the time intervals between peaks (Fig. 2). To accurately calculate the size of a time series peak, we must sum the area under the time series from the start to the stop of the particular particle injection. The particles we image are thought to be linear arrays of smaller subunits⁷, therefore a larger injection will occur over a longer amount of time. However, by summing the peak area from one trough to the next, we could introduce an artificial correlation between the peak size and the peak interval. Therefore, an alternate way to determine injection size would be to measure the maximum intensity, e.g. the peak height, of the injection. Assuming that injections are linear arrays of constant-intensity subunits, this method relies on the constructive interference between neighboring subunits to give a measure of the injection size. Two obvious shortcomings of such a method are that it underestimates the injection size and is more prone to error due to single time point intensity fluctuations. Because there are strengths and weaknesses of both methods, we rely primarily on a compromise between the two, summing the area of the peak where the peak height is above 70% of the maximum height. This

peak measure should more-accurately reflect the real injection size, but we also used injection height in order to validate all major trends we observed and found that it gave similar results. Peak size calculated by area is highly correlated with peak size calculated by height ($r=0.95$, $p<0.0001$, $N=48$).

Note that when presenting aggregate data for peak size and frequency, we use the median rather than the mean because in our dataset these parameters have skewed distributions, hence the median provides a more robust statistic for low sample numbers.

2.7 Validation of automated analysis

In addition to using synthetic kymographs, we also verified that the algorithm yields equivalent results to hand-tracing of clear kymograph traces (Fig. 6a).

2.8 *In vitro* dynein motility assay control experiment

We verified performance of the algorithm using video images of dual-GFP-labeled dynein walking on sea urchin sperm axonemes stuck to a cover glass, which was generously provided by Julia Kardon of the Vale lab at UCSF. The identical Nikon microscope setup was tuned to give an equivalent laser angle of incidence to our experimental scenario. This control allowed us to examine a robust *in vitro* analogy to our *in vivo* scenario. The results show no axoneme length dependence of any parameters, no correlation between the time interval preceding a peak and the peak size ($r=0.05$, $p<0.05$), and an exponentially distributed peak size distribution ($\gamma=1.03$).

2.9 Note on automated kymograph analysis algorithms

All code was written and executed in MATLAB R2007a (Mathworks). Elements of the Time Series Analysis, Image Processing, and Statistics Toolboxes (Mathworks) were utilized in development of the algorithms.

We note that a different kymograph image processing algorithm has previously been applied to IFT by Piperno and colleagues³. This algorithm, however, was only a procedure to enhance the visibility of IFT kymograph traces and facilitate manual analysis. It did not directly produce quantitative time series data as our method does. We also note that other methods exist for analyzing motion of particles in microscopy images, such as single particle tracking algorithms, and these have been highly successful in studies of cytoskeletal dynamics⁸. Such methods should also be applicable to analysis of our data and it will be interesting to consider the relative merits of such approaches in comparison to the kymograph analysis used here.

3. RESULTS AND DISCUSSION

3.1 Algorithm performance

The KPA does a good job of finding the speed of moving particles (Fig. 6a), though the efficacy of the algorithm decreases as the kymograph width decreases (Fig. 6b). Therefore, when running the algorithm without user checks on rotation angle output, the kymograph width must be 30 pixels or greater. On our camera, this corresponds to a length of around 3 microns. Below that width, user verification of rotation angles becomes necessary.

3.2 Computation time

We ran all of our analysis on a 2GHz Intel-based MacIntosh laptop with 2GB RAM in native MATLAB R2007a. The time for either Radon transform-based algorithm to process one kymograph is on the order of 1 minute, depending on the kymograph size. This processing time can be decreased to around 20 seconds by restricting the possible angles to a reasonable range.

3.3 Sample data analysis

We analyzed a sample set of 48 kymographs using back-projection-based angle finding. Total computational time was 50 minutes using an unrestricted angle range. The results are given in Figure 7. A novel finding using this approach is that the interval time preceding a peak is correlated with the resulting injection size ($r=0.53$, peak size calculated by height rather than area). There was significantly lower correlation with either of the adjacent time intervals, suggesting that a renewal process may govern the injection apparatus⁹ (Fig. 7a).

We also examined the peak interval distribution (PID), finding a significant fit to a gamma distribution with the gamma parameter equal to 5 (Fig. 7b). This suggests that if a renewal process does indeed govern the injection apparatus, there may be 5 independent events that must take place before an injection occurs⁹.

3.4 Strengths and limitations of the methods

Our methods reliably produce quantitative measures of intracellular particle traffic from video data. In addition to the obvious strengths of all high throughput image processing techniques, one of the great advantages of this method is that by spatially averaging out camera noise, we can use higher EMCCD gain settings and therefore faster frame rates for digital image acquisition.

However, the method is limited in several ways. First, all particles on a kymograph must be moving at equivalent speed in order to be detected. This weakness precludes the general applicability of this method to analysis of diverse kymograph data. Second, kymographs must be made over a region at least 30 pixels long in order for the algorithm to be able to run without user validation. This additional constraint on the method restricts the application of this method even further. However, we note that we have begun the use of other transforms, such as the wavelet transform¹⁰ in order to extract variable speed particle traces from kymographs.

3.5 Role of automated kymograph analysis in quantitative cell dynamics

It has become increasingly easy to visualize live intracellular dynamics with the advent of GFP tagging and of microscopy techniques such as TIRF and speckle imaging that readily allow visualization of moving particulate objects⁸. With the automation of microscopes and increases in data storage capacity, we can now acquire large sets of visual data. In order to extract the maximum information from such large datasets, automated methods to analyze dynamics are absolutely critical. Moreover, it is important to have methods that do not require user intervention. Kymographs in particular are often analyzed by having a user trace a line parallel to a moving particle, but this is potentially susceptible to inadvertent user bias as well as to differences from one user to another in terms of which objects are classified as bona fide traces. An automated algorithm will always give the same result when run on the same starting dataset, thus removing the danger of user-specific variability.

Perhaps more importantly, automated quantitative analysis of large datasets allows statistical analysis to be performed to detect subtle features of the data, such as interval distributions¹¹. We view this particular example as an illustration of the general trend in biological microscopy to move beyond mere imaging and to view multidimensional microscopy datasets as a rich source of numerical information to be mined by quantitative methods and compared with predictions of mathematical models.

4. ACKNOWLEDGEMENTS

We thank Kurt Thorn and the Nikon Imaging Center at UC San Francisco for invaluable microscopy resources and assistance. We thank Julia Kardon for help acquiring test-images of in vitro dynein motility used for verifying algorithm performance. We also thank Joshua Mueller, Mary Porter, Hongmin Qin, Joel Rosenbaum, Karl Letchreck and George Witman for generously sharing strains and antibodies, as well as members of the Marshall lab for careful reading of the manuscript. This work was funded by the W. M. Keck Foundation Distinguished Young Scholars Program (W. Marshall), the Searle Scholar Program (W. Marshall) and an NSF Graduate Research Fellowship (W. Ludington).

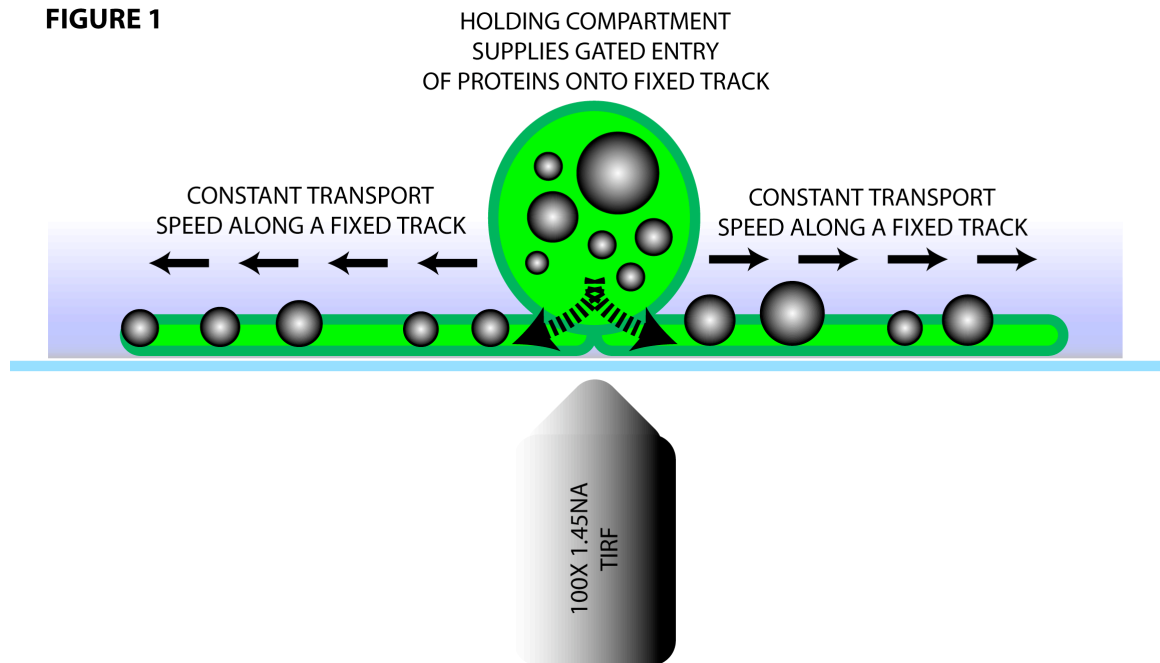
5. REFERENCES

- [1]. Zimmer HG. "The contributions of Carl Ludwig to cardiology." *Can J Cardiol.* 15:323-9. (1999).
- [2]. Qiu Q, Schutte HK. "A new generation videokymography for routine clinical vocal fold examination." *Laryngoscope.* 116:1824-8. (2006).
- [3]. Piperno, G., E. Siuda, S. Henderson, M. Segil, H. Vaananen, and M. Sassaroli. "Distinct mutants of retrograde intraflagellar transport (IFT) share similar morphological and molecular defects." *J. Cell Biol.* 143:1591-601. (1998).
- [4]. Axelrod, D. "Total internal reflection fluorescence microscopy in cell biology." *Traffic.* 2:764-774. (2001).
- [5]. Shumway, RH and Stoffer, DS. [Time Series Analysis and Its Applications: With R Examples] Springer: New York. (2006).
- [6]. Deans, Stanley R. *The Radon Transform and Some of Its Applications.* John Wiley & Sons: New York. (1983).
- [7]. Cole, D. G., D. R. Diener, A. L. Himelblau, P. L. Beech, J. C. Fuster, and J. L. Rosenbaum. "*Chlamydomonas* kinesin-II-dependent intraflagellar transport (IFT): IFT particles contain proteins required for ciliary assembly in *Caenorhabditis elegans* sensory neurons." *J. Cell Biol.* 141:993-1008. (1998).
- [8]. Valloton, P., Ponti, A., Waterman-Storer, C.M., Salmon, E.D., and Danuser, G. "Recovery, visualization, and analysis of actin and tubulin polymer flow in live cells: a fluorescent speckle microscopy study." *Biophys. J.* 85: 1289-1306. (2003).

- [9]. Parzen, E. [Stochastic processes]. Holden-Day, Inc. San Francisco. (1962).
- [10]. Candes EJ, Demanet, L, Donoho, DL, Ying, L. "Fast Discrete Curvelet Transforms." Proc. SPIE wavelets XI, San Diego. (2005).
- [11]. Odde, D.J., and Buettner, H.M. "Autocorrelation function and power spectrum of two-state random processes used in neurite guidance." Biophys. J. 75: 1189-96. (1998).

Figures:

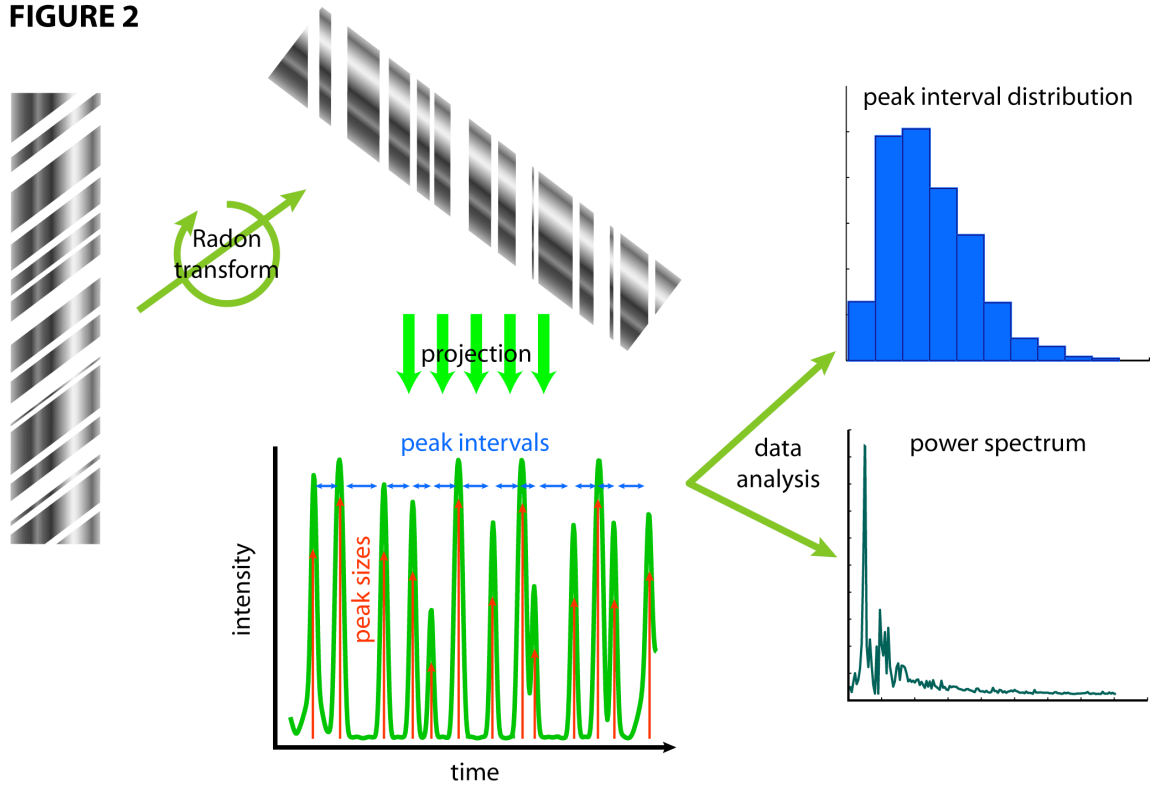
Figure 1: Experimental setup.



A cell sits on the coverglass in the TIRF field and GFP-tagged proteins are imaged. The tagged proteins form aggregate particles which are injected from the holding compartment onto fixed tracks. While on the fixed tracks, the aggregate particles move at constant speed. Kymographs are made by hand-tracing a line segment along the fixed tracks.

Figure 2: Automated kymograph analysis algorithm

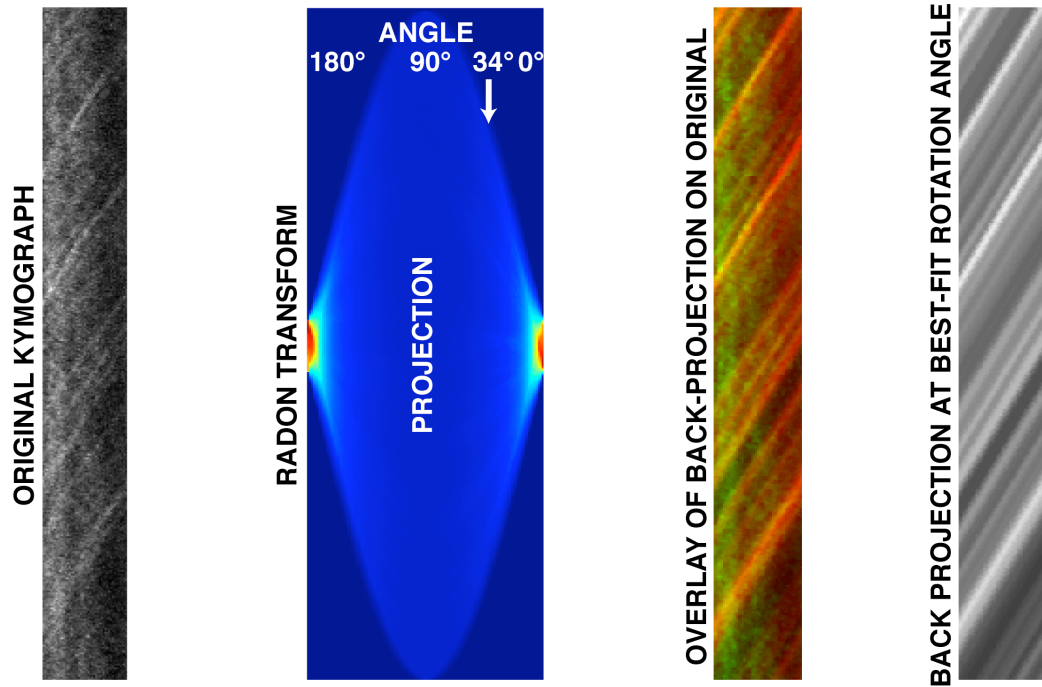
FIGURE 2



A radon transform is used to detect the dominant speed of moving particles on the input kymograph. The projection along the direction of this dominant speed produces a time series of the injection behavior. The time series is then analyzed directly using the power density spectrum or else deconstructed into peak sizes and peak intervals for further analysis.

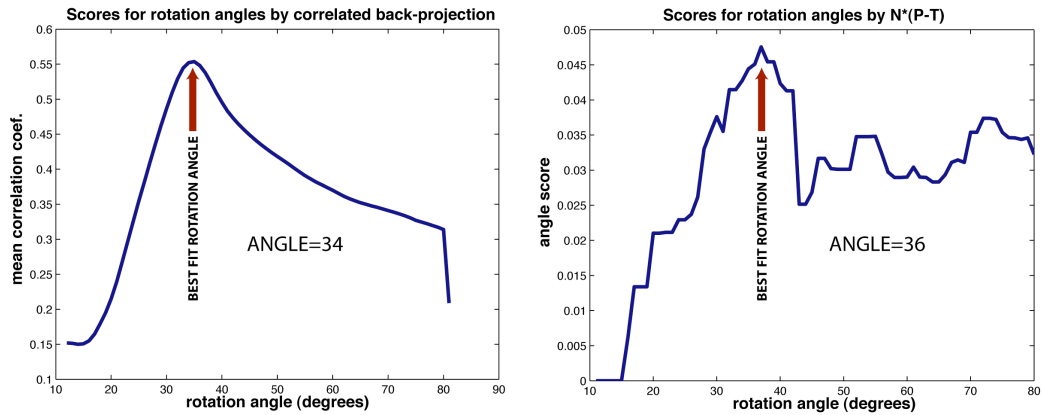
Figure 3: Sample kymograph processing steps.

FIGURE 3



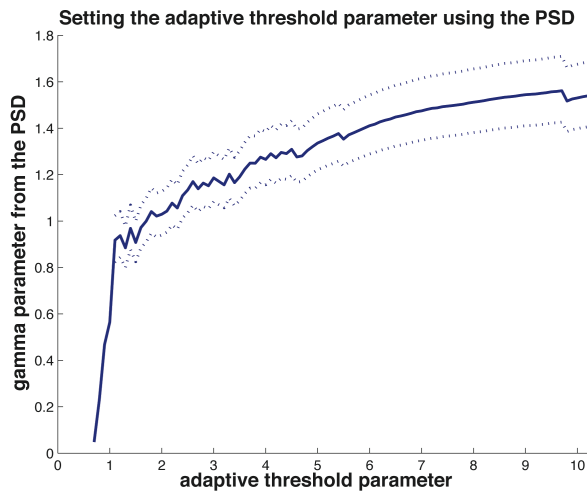
From left to right: an input kymograph has a high level of noise due to high gain setting on the EMCCD camera; the first step in the processing algorithm computes the Radon transform of the kymograph, which is a series of 1-D projections as a function of the projection angle. The best-fit angle is indicated at 34 degrees; the best fit angle was found by the correlation of the input kymograph with its back-projection (see Fig. 4). The overlay is shown here, with original (green) and back-projection (red); the back-projection of the best-fit rotation angle is shown on the far right. It is used to make the time series of particle injections.

Figure 4: Sample rotation angle scoring for the kymograph in Fig. 3.



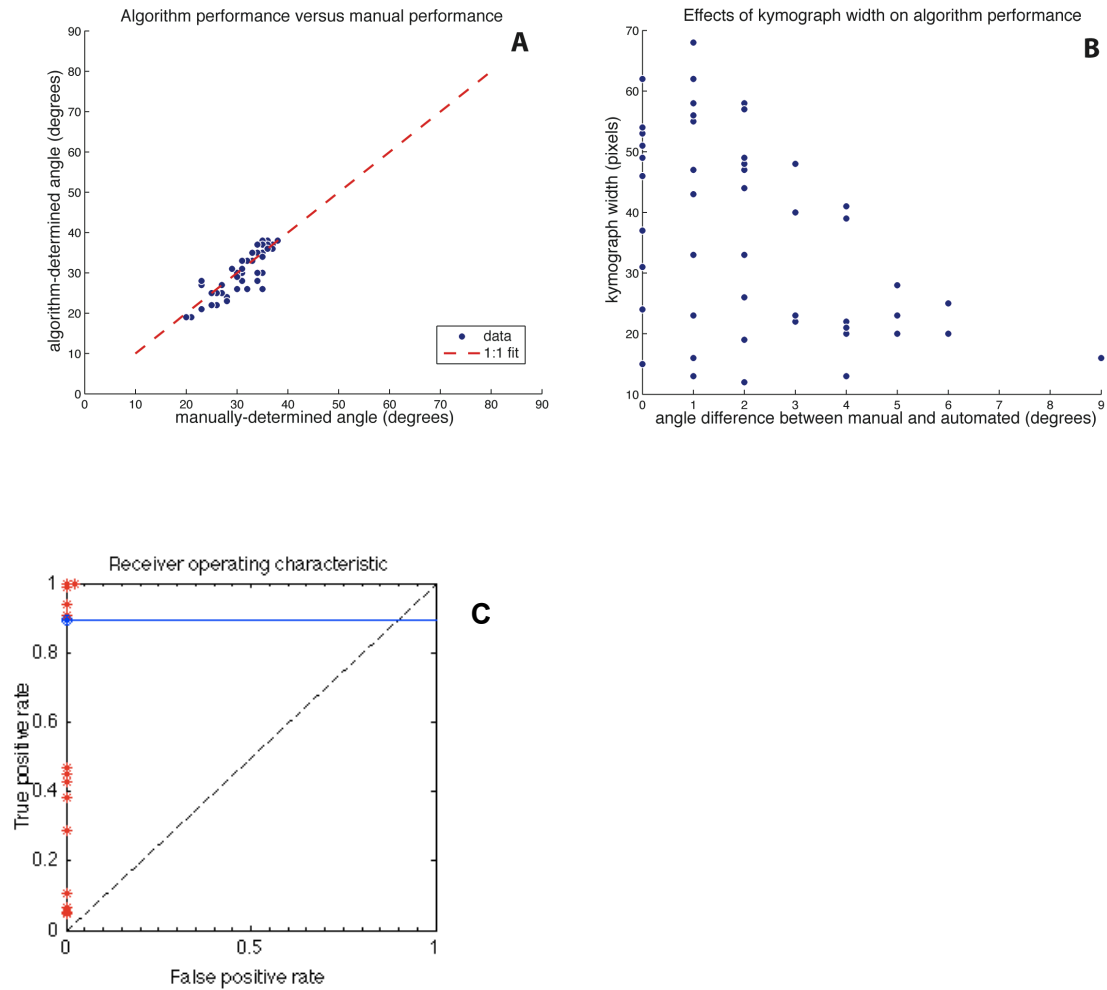
Left: the back-projection-based angle-fitting algorithm produces a smooth best-fit angle function. The mean correlation coefficient between input kymograph and back projection is shown as a function of the rotation angle. 34 degrees is the best fit. **Right:** the method of finding the best-fit angle by maximizing the function, n times (p minus t), where n is number of peaks, p is median peak height, and t is median trough height, produces a rougher, best-fit angle function but none-the-less gives an accurate rotation angle.

Figure 5: Setting the adaptive threshold parameter.



We set the adaptive threshold parameter by finding the best-fit of the peak size distribution to an exponential distribution. The logic for this approach is that the TIRF illumination field decays exponentially away from the coverglass, therefore when our algorithm is tuned correctly, the PSD should be exponential.

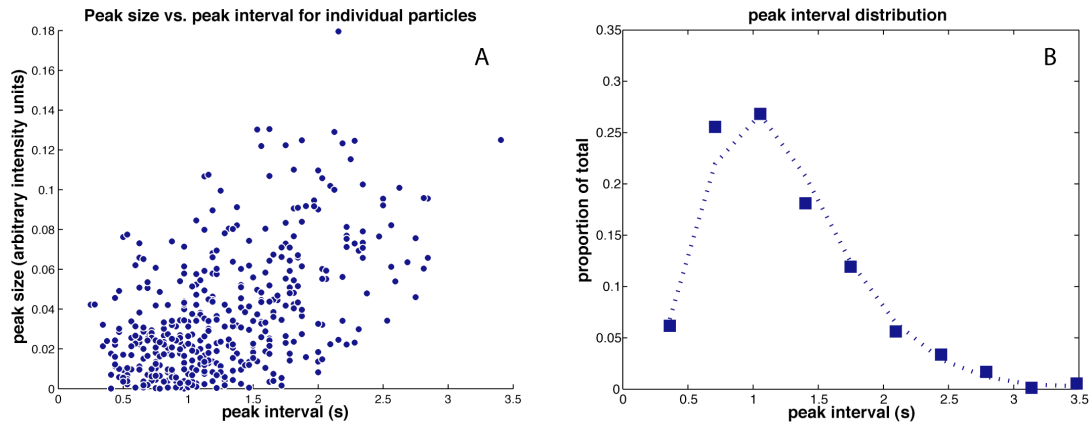
Figure 6: Algorithm performance.



(A) By-eye rotation angle measurements plotted against algorithm-determined angle measurements. (B) The width of the input kymograph is a primary determinant of the error in rotation angle determination. It is hard to detect a difference between rotation angles that differ by 5 degrees or less. (C) Receiver-operating-characteristic (ROC). Synthetic kymographs were constructed in order to test the quality of the algorithm (see Chapter 2 for further details on synthetic kymograph construction). An extremely low false positive rate gives an atypical ROC. False positives were calculated as the number of false hit detections divided

by the total number of detections. True positives were calculated as the number of true hit detections divided by the actual number of hits. The signal-to-noise ratio in the synthetic kymographs was varied in order to produce the results shown.

Figure 7: Sample data from intracellular transport of fluorescent proteins.



48 kymographs were analyzed with a total of 403 moving particles detected.

Mean speed of particles on the kymographs was 1.9 microns per second. (A) The size of an injection peak tends to be larger the longer the time interval before the injection occurs ($r=0.53$, $N=403$). (B) The peak interval distribution has a good fit to a gamma distribution with gamma parameter 5.01 ($N=403$).

Chapter 3

Avalanche-like behavior in ciliary length control

Authors: **WB Ludington¹, KA Wemmer¹, KF Lehtreck², GB Witman², WF Marshall¹**

1. Dept. of Biochemistry and Biophysics, University of California, San Francisco, CA 94158
2. Dept. of Cell Biology, University of Massachusetts Medical School, Worcester, MA 01655

Synopsis:

Using methods presented in Chapter 1, I analyze intraflagellar transport particle injection behavior and show that the process has avalanche-like properties. This analysis combined with quantification of standard fluorescence microscopy of the flagellar base during ciliogenesis suggests that flagellar length is regulated by adjusting the amount of IFT material accumulate at the flagellar base rather than regulating each injection of material into the flagellum.

Abstract:

Cilia and flagella are microtubule-based organelles that make a filamentous projection from the cell body. Length defects in these organelles cause a broad range of congenital human disease ranging from polydactyly, polycystic kidneys, and obesity to hydrocephaly, blindness, and mental retardation (Badano et al., 2006). Many of these defects arise from mutations in the intraflagellar transport (IFT) proteins, which deliver cargo from the cell body to the flagellar tip for assembly (Cole and Snell, 2009; Pazour and Rosenbaum, 2002). The process controlling injections of IFT trains into the flagellar compartment is, therefore, crucial to ciliogenesis. Extensive biochemical and genetic analyses have determined the molecular machinery of IFT and how trains are licensed for entry. However, these studies do not explain how the machinery sets the injection rate and thus the ciliary length. Here, we provide evidence that IFT injections result from avalanche-like releases from the accumulated load of IFT material at the flagellar base and that the key regulated feature of length control is the recruitment of IFT material to the flagellar base. We used TIRF microscopy of IFT proteins in live cells to quantify the size and frequency of injections over time (Ludington and Marshall, 2009). The injection dynamics reveal a negative correlation between injection size and frequency as well as rich behaviors such as quasiperiodicity and bursting. These behaviors are tied to the size of the localized load of IFT material awaiting injection at the flagellar base and indicate that IFT injection dynamics are mathematically consistent with avalanche-like behavior (Bak et al., 1987). Our results provide new insight into how ciliary length is

regulated, suggesting that misregulation of IFT protein localization rather than defective entry control causes length defects. Importantly, our findings break the problem of length control into two distinct parts: (1) accumulation control and (2) entry control, and they show how changes in accumulation affect entry. From a biochemical perspective, the results suggest that investigators focus on the proteins regulating length-dependent accumulation in addition to entry control. The results also demonstrate how a simple physical mechanism can control organelle size.

Introduction

Cells use cilia and flagella for a variety of purposes including fluid flow and cell-cell signaling (Badano et al., 2006). Ciliary length defects generate a wide range of congenital human diseases. Many of these defects arise from mutations in the intraflagellar transport (IFT) proteins, which are required to build and maintain the length of the cilium [or flagellum] (Pazour and Rosenbaum, 2002). The IFT proteins form stoichiometric aggregates called IFT trains that haul cargo to the ciliary tip for assembly (Cole and Snell, 2009). IFT trains first localize to the basal body (Deane et al., 2001) then enter the cilium as a group in an injection event. Understanding how the IFT injection process works is critical to understanding ciliary length control because the injection rate sets the overall amount of transport.

Previous reports observed periodic IFT injection and suggested that a periodic regulator gates the entry of new IFT trains, indicating that a biochemical clock may be at the heart of IFT injection regulation. Consistent with this hypothesis, Craige *et al* and Dishinger *et al* performed elegant biochemical and genetic experiments that suggest proteins may be licensed for entry into the ciliary/flagellar compartment by a mechanism similar to nuclear import (Craige et al., 2010; Dishinger et al., 2010). These studies, however, do not explain how the injection dynamics (e.g. timing and magnitude of injections) or the injection rate (mean amount of material/second) arise. Furthermore, the recent finding that an increased injection size in regenerating flagella corresponds to a lowered injection frequency presents a problem for the biochemical oscillator hypothesis because an

oscillator should modulate frequency and amplitude separately rather than compensating for increased amplitude with decreased frequency. We therefore took a different approach.

Results and Discussion

To gain insight into how the injection dynamics and the overall injection rate arise in the IFT system, we examined time series of IFT injections into the cilium. We used total internal reflection fluorescence (TIRF) microscopy of GFP-tagged IFT proteins in *Chlamydomonas reinhardtii* flagella for all of our studies (Engel et al., 2009; Ludington and Marshall, 2009) because of the available genetic mutants with abnormal flagellar length and the ease of flagellar imaging: cells adhere to the coverglass with their flagella, which lay entirely within the near-TIRF excitation field (Fig. 1a). Examination of the time series revealed some apparent periodicity (Dentler, 2005) (Fig. 1b) but also significant bursting activity ($p=0.001$, 11/40, Binomial statistic, Supplementary Fig. 1) as well as long term correlations in injection timing (Hurst exponent =0.61, SEM 0.03).

To quantify the periodicity of IFT trains, we computed the power (squared amplitude) in the signal at each frequency (Fig. 1c, Supplementary Fig. 2a). Power is concentrated in the low frequencies (centered around 1 Hz) but drops off at high frequencies. The broad peak in the power spectrum indicates that the injections are periodic but not strictly so. We therefore examined the power spectrum in a rolling window across each time series to determine whether the periodicity is a transient phenomenon (Schaffer et al., 1993) (Supplementary Fig. 3). In 100% of our kymographs, significant periodicity ($p<0.05$) occurs at 1 Hz for at least 71.5% of the time (robust Fisher's G-test). More specifically, we observe onset and decay of periodicity in the time series showing that injections transition between periodic and aperiodic regimes (Supplementary Fig. 3). For a

cell, this quasiperiodic behavior indicates regularity but not consistency, suggesting that a true biochemical clock does not set the system dynamics (Hogenesch and Herzog, 2011).

Avalanche-like systems (Bak et al., 1987) represent a class of generic systems that can show quasiperiodic behavior. Avalanches are characterized by discrete, intermittent events, which often show long term correlations (Politzer, 2000) (e.g. evidenced by bursting and a Hurst exponent >0.5). These generic behaviors are found in wide-ranging examples in nature, from sand pile avalanches (Jaeger et al., 1989) and stick-slip systems (Ciliberto and Laroche, 1994) such as earthquakes to network connectivity, evolution, and spread of epidemics (Jensen, 1998). In physical examples a continuous loading strain leads to a discontinuous release of the strain (Fig. 2a). These systems typically show a correlation between the amount of strain released and the time intervals between release events (Shimazaki and Nakata, 1980).

We therefore examined the relationship between injection magnitudes and the time intervals between injections. Consistent with the observed periodicity, we see significant positive correlations with magnitude for both the time preceding an event and the time following an event (Fig. 2b,c, Supplementary Fig. 4b,c), matching the behavior of stick-slip systems that are both time and slip predictable. The correlation is stronger for the time preceding an event, suggesting that the system has more noise in accumulation of material than in release of material (Weldon et al., 2004).

An increase in injection size corresponds to an increase in the time interval, i.e. a decrease in injection frequency (Engel et al., 2009) (Supplementary Fig.4a; injection size: 125 vs. 316 normalized intensity units, $n=76$, $p=1.6E-5$, one-tailed T-test; mean injection frequency: 1.43 Hz vs. 0.869 Hz, $p=4.6E-5$, one-tailed T-test). At first glance this is somewhat surprising because this decrease in frequency offsets some of the increase in size. However, for an avalanching system, increasing the input rate of material can increase the diameter of the pile, which results in larger but less-frequent injections (Jaeger and Nagel, 1992) (Fig. 2a). Therefore, the relationship between frequency and magnitude may be fixed as a natural consequence of a simple physical system.

Regardless of the diameter of the pile, an avalanching system should maintain the correlation between injection timing and magnitude independent of other variables, such as flagellar length. By contrast, alternate models suggest that timing and magnitude should be decoupled if the injector sets these parameters independent of one another based on the flagellar length (Dentler, 2005; Engel et al., 2009). Therefore, we examined how the injection dynamics (i.e. timing and magnitude) vary in response to three distinct biochemical and genetic perturbations that alter flagellar length. Consistent with an avalanching system, the perturbations did not change the injection dynamics from wildtype (Fig. 3a,b). If a biochemical oscillator dictated the timing and magnitude of the individual injection events, then one would not necessarily expect the injection dynamics to be preserved when these pathways are perturbed.

Strikingly, while the perturbations we examined did not change the injection dynamics, they did change the injection rate as a function of flagellar length. When we measured IFT in wildtype cells, we found a decrease in injection rate with increasing flagellar length (Engel et al., 2009) (Fig. 3c), which matches the length kinetics seen in regenerating flagella: flagella grow faster the shorter they are and full-length flagella do not grow at all. In the perturbations to flagellar length we found injection rates that cannot correct for the altered flagellar length but rather could cause it, suggesting that a perturbed injection rate itself may cause the length change: the lengthened flagella inject as if they were regenerating, and the shortened flagella inject as if they were full length.

The avalanching system hypothesis makes another important prediction: the injection dynamics arise from the size of the accumulated load of IFT material (i.e. small, frequent injections arise from small accumulated loads, while large, infrequent injections arise from large accumulated loads; Fig. 2a). Therefore, we examined the IFT material accumulated at the flagellar base (Deane et al., 2001) to determine whether we could detect evidence for such a relationship. We compared rapidly regenerating versus full-length flagella, which have large, infrequent injections and small, frequent injections respectively (Engel et al., 2009) (Supplementary Fig. 4). Consistent with an avalanching system, we found that more material accumulates at the base of the regenerating flagella (Fig. 4; Supplementary Fig. 6). This observation indicates that the injection dynamics are proportional to the recruitment of material to the flagellar base. Thus, rather than regulating each individual IFT train injection as some biochemical evidence

suggests, the system may regulate just the accumulated load of IFT material at the base. We note that this finding is not inconsistent with the biochemical evidence but rather indicates that two biochemical processes are actually at work: (1) entry licensing and (2) the length-dependent accumulation of IFT material at the flagellar base. Furthermore, we believe that the work of Dishinger *et al* (Dishinger *et al.*, 2010) suggests a compelling hypothesis that a RanGTP concentration gradient could actually provide the cell with a flagellar length sensor, which would serve to set the length-dependent accumulation.

From all of our experimental evidence, the avalanche model provides a maximally parsimonious explanation for the behavior seen in cells with perturbed length control. We confirmed this by generating a computational model of avalanche-like behavior in a low-Reynolds number environment (Supplementary Fig. 5a-c) (Burrige and Knopoff, 1967; Huang and Turcotte, 1990).

It was suggested to us (C. Tang *pers. comm*) that a simpler, alternate physical model for the injection timing is one of traffic jams (Kuznetsov and Hooman, 2008). In this model, individual IFT trains block each other's movement as they enter the flagellum, and a higher density of trains leads to more bunching (Sugiyama *et al.*, 2008). We examined a computational model of this system (Chowdhury *et al.*, 2005) but found no agreement with our data (Supplementary Fig. 5d-f). The key difference in the two models is that the avalanche model allows the storage of potential energy in the system for release at a later time step, whereas the traffic model allows no storage of energy. Several alternate

biochemical models also fail to agree with our results (Supplementary Table 1). Only the avalanche model recapitulates the observed relationships in our data.

The presence of avalanche-like behavior suggests a storage of potential energy at the flagellar base, similar to how a transiently stable configuration of sand grains can increase above the angle of repose in a sand pile (Jaeger et al., 1989; Jaeger and Nagel, 1992) (Fig. 2a), which brings up the question of how this energy is stored. Though the molecular details cannot be known at present, there is precedent for potential energy being stored in networks of cytoskeletal filaments and motors (Mahadevan and Matsudaira, 2000). For example, tension could build up in the tubulin cytoskeleton as kinesin II motors step without available space in which to drag their cargo, due to molecular crowding or to the Cep290 constriction of the flagellar membrane at the entry site (Craigie et al., 2010).

Notably, our findings explain why the injection frequency counteracts the injection magnitude when the injection rate increases. A biochemical oscillator would increase magnitude, frequency, or both. But in the IFT injector, injection frequency decreases as injection magnitude increases. This behavior is a natural consequence of an avalanching system due to the increased size of the accumulated load of material at the flagellar base (Fig. 2a). Previous studies have focused on regulation of IFT train entry into the flagellum (Craigie et al., 2010; Dishinger et al., 2010), a clearly important feature. Our findings indicate that in order to understand how length is controlled, we should additionally ask how the recruitment of IFT material to the base is set. Our findings suggest that the *lf4*

gene and lithium treatment both affect IFT train recruitment to the flagellar base rather than entry into the flagellum (Fig. 3).

Avalanche-like systems have been described in all areas of nature, ranging from experimental sand pile avalanches to mountain snow avalanches, from magnetic turbulence in plasmas to spots on the sun, from simple sliding blocks to earthquakes, and from spread of epidemic disease to mass extinction events.

Avalanche-like systems display discrete, intermittent events with long terms correlations, i.e. memory in the system. Our data show that the IFT injection system shows these qualities. Avalanche-like systems are also known by their persistent '1/f' noise, as evidenced by a power spectrum with a slope of -1, but small-scale systems are prone to finite-size effects, which cause the power spectrum to fall below the -1 slope at low and high frequencies (Bak et al., 1987).

We estimate that at a maximum the IFT injector can hold on the order of 100 particles and thus falls in the realm of finite size effects. Therefore, we are not surprised that the IFT injector does not show this characteristic spectrum.

We also note that because such avalanche-like systems have the potential for periodic behavior, they offer the cell a physical mechanism by which to generate regularity. Avalanching systems could therefore serve as an evolutionary starting point for a biochemical oscillator to develop from. Oscillators are ubiquitous in cells, regulating such diverse functions as the cell cycle, cardiac muscle contraction, and diverse aspects of metabolism (Brandman and Meyer, 2008).

While oscillators are ubiquitous, they are often composed of many coordinated parts, raising the question of how they could have arisen in evolution. Our

findings suggest that avalanching oscillators can arise spontaneously by a simple physical mechanism.

Methods summary: The KAP-GFP rescue of the *fla3* mutant was described previously by Mueller *et al* (Mueller *et al.*, 2005), and an *lf4*/KAP-GFP/*fla3* strain was produced by mating and PCR-based genotyping. The *lf4* strain used was allele *lf4*-V86, a gift from the Dieckmann lab. An IFT20-GFP rescue of the null IFT20 mutant was produced as described previously (Lechtreck *et al.*, 2009). All strains were grown on TAP agar plates and then transferred to M1 liquid media under continuous light before fixation or live cell imaging. LiCl (Sigma) was used as described (Wilson and Lefebvre, 2004). Cycloheximide (Sigma) was prepared as a 10mg/mL stock in ethanol and diluted to a 10 µg/mL working concentration. Cells were deflagellated by passing log-phase culture through an insulin syringe (28 gauge, 1cc).

Live cell imaging was performed on a Nikon te2000 microscope with a 100x 1.49 NA TIRF oil lens and 488 nm laser illumination with a 514 nm dichroic mirror and a 525 nm filter. Images were recorded at 29.7 frames per second on a Photometrics QuantEM EMCCD camera with 0.156 microns per pixel. The calibration technique is in the online methods. Kymographs were made using Nikon elements (v3.1) and converted to IFT injection time series using custom MATLAB software as described previously (Ludington and Marshall, 2009) with specific parameters for smoothing and background subtraction that are indicated in the online methods section.

Methanol fixation was as described previously (Feldman and Marshall, 2009). Fixed samples were imaged on a Deltavision microscope at 100x. Z-stacks were acquired with a 0.2 micron z-step. Deconvolution was performed using

Deltavision software. Custom software was written in MATLAB to delineate and quantify the area at the flagellar base. Samples were compared by one-way ANOVA and then multiple pairwise comparisons were made using Bonferroni's correction for alpha.

Statistical tests were performed in MATLAB using the Statistical Analysis Toolbox.

References

- Ahdesmaki, M., H. Lahdesmaki, and O. Yli-Harja. 2007. Robust Fisher's test for periodicity detection in noisy biological time series. *Genomic Signal Processing and Statistics, 2007. GENSIPS 2007. IEEE International Workshop on*:1-4.
- Badano, J.L., N. Mitsuma, P.L. Beales, and N. Katsanis. 2006. The ciliopathies: an emerging class of human genetic disorders. *Annu Rev Genomics Hum Genet.* 7:125-148.
- Bak, P., C. Tang, and K. Wiesenfeld. 1987. Self-organized criticality: An explanation of the 1/f noise. *Physical Review Letters.* 59:381-384.
- Berman, S.A., N.F. Wilson, N.A. Haas, and P.A. Lefebvre. 2003. A novel MAP kinase regulates flagellar length in *Chlamydomonas*. *Curr Biol.* 13:1145-1149.
- Brandman, O., and T. Meyer. 2008. Feedback loops shape cellular signals in space and time. *Science.* 322:390-395.
- Burridge, R., and L. Knopoff. 1967. Model and theoretical seismicity. *Bulletin of the Seismological Society of America.* 57:341-371.
- Chowdhury, D., A. Schadschneider, and K. Nishinari. 2005. Physics of transport and traffic phenomena in biology: from molecular motors and cells to organisms. *Physics of Life reviews.* 2:318-352.

- Ciliberto, S., and C. Laroche. 1994. Experimental evidence of self organized criticality in the stick-slip dynamics of two rough elastic surfaces. *Journal de Physique I*. 4:223-235.
- Cole, D.G., and W.J. Snell. 2009. SnapShot: Intraflagellar transport. *Cell*. 137:784-784e781.
- Craige, B., C.-C. Tsao, D.R. Diener, Y. Hou, K.-F. Lehtreck, J.L. Rosenbaum, and G.B. Witman. 2010. CEP290 tethers flagellar transition zone microtubules to the membrane and regulates flagellar protein content. *J Cell Biol*. 190:927-940.
- Deane, J.A., D.G. Cole, E.S. Seeley, D.R. Diener, and J.L. Rosenbaum. 2001. Localization of intraflagellar transport protein IFT52 identifies basal body transitional fibers as the docking site for IFT particles. *Curr Biol*. 11:1586-1590.
- Dentler, W. 2005. Intraflagellar transport (IFT) during assembly and disassembly of *Chlamydomonas* flagella. *J Cell Biol*. 170:649-659.
- Dishinger, J.F., H.L. Kee, P.M. Jenkins, S. Fan, T.W. Hurd, J.W. Hammond, Y.N.-T. Truong, B. Margolis, J.R. Martens, and K.J. Verhey. 2010. Ciliary entry of the kinesin-2 motor KIF17 is regulated by importin-beta2 and RanGTP. *Nat Cell Biol*. 12:703-710.

- Engel, B.D., W.B. Ludington, and W.F. Marshall. 2009. Intraflagellar transport particle size scales inversely with flagellar length: revisiting the balance-point length control model. *J Cell Biol.* 187:81-89.
- Feldman, J.L., and W.F. Marshall. 2009. ASQ2 encodes a TBCC-like protein required for mother-daughter centriole linkage and mitotic spindle orientation. *Curr Biol.* 19:1238-1243.
- Gardner, M.K., B.L. Sprague, C.G. Pearson, B.D. Cosgrove, A.D. Bicek, K. Bloom, E.D. Salmon, and D.J. Odde. 2010. Model Convolution: A Computational Approach to Digital Image Interpretation. *Cell Mol Bioeng.* 3:163-170.
- Hogenesch, J.B., and E.D. Herzog. 2011. Intracellular and intercellular processes determine robustness of the circadian clock. *FEBS Lett.* 585:1427-1434.
- Huang, J., and D. Turcotte. 1990. Evidence for chaotic fault interactions in the seismicity of the San Andreas fault and Nankai trough. *Nature.* 348:234-236.
- Jaeger, H., C.-H. Liu, and S.R. Nagel. 1989. Relaxation at the angle of repose. *Physical Review Letters.* 62:40-43.
- Jaeger, H.M., and S.R. Nagel. 1992. Physics of the granular state. *Science.* 255:1523-1531.

- Jensen, H.J. 1998. Self-organized criticality: emergent complex behavior in physical and biological systems. Cambridge University Press, New York.
- Kuznetsov, A., and K. Hooman. 2008. Modeling traffic jams in intracellular transport in axons. *International Journal of Heat and Mass Transfer*. 51:5695-5699.
- Lehtreck, K.-F., E.C. Johnson, T. Sakai, D. Cochran, B.A. Ballif, J. Rush, G.J. Pazour, M. Ikebe, and G.B. Witman. 2009. The *Chlamydomonas reinhardtii* BBSome is an IFT cargo required for export of specific signaling proteins from flagella. *The Journal of Cell Biology*. 187:1117-1132.
- Ludington, W., and W. Marshall. 2009. Automated analysis of intracellular motion using kymographs in 1, 2, and 3 dimensions. *Proceedings of SPIE*. 7184.
- Magleby, K.L., and B.S. Pallotta. 1983. Burst kinetics of single calcium-activated potassium channels in cultured rat muscle. *J Physiol (Lond)*. 344:605-623.
- Mahadevan, L., and P. Matsudaira. 2000. Motility powered by supramolecular springs and ratchets. *Science*. 288:95-100.
- Mueller, J., C.A. Perrone, R. Bower, D.G. Cole, and M.E. Porter. 2005. The FLA3 KAP subunit is required for localization of kinesin-2 to the site of

- flagellar assembly and processive anterograde intraflagellar transport. *Mol Biol Cell*. 16:1341-1354.
- Nakamura, S., H. Takino, and M.K. Kojima. 1987. Effect of lithium on flagellar length in *Chlamydomonas reinhardtii*. *Cell Struct Funct*. 12:369-374.
- Pazour, G.J., and J.L. Rosenbaum. 2002. Intraflagellar transport and cilia-dependent diseases. *Trends Cell Biol*. 12:551-555.
- Politzer, P. 2000. Observation of avalanchelike phenomena in a magnetically confined plasma. *Physical Review Letters*. 84:1192-1195.
- Rosenbaum, J.L., J.E. Moulder, and D.L. Ringo. 1969. Flagellar elongation and shortening in *Chlamydomonas*. The use of cycloheximide and colchicine to study the synthesis and assembly of flagellar proteins. *J Cell Biol*. 41:600-619.
- Schaffer, W., B. Kendall, C. Tidd, and L. Olsen. 1993. Transient periodicity and episodic predictability in biological dynamics. *Journal of Mathematics Applied in Medicine and Biology*.
- Shimazaki, K., and T. Nakata. 1980. Time-predictable recurrence model for large earthquakes. *Geophysical Research Letters*. 7:279-282.
- Sugiyama, Y., M. Fukui, M. Kikuchi, K. Hasebe, A. Nakayama, K. Nishinari, S. Tadaki, and S. Yukawa. 2008. Traffic jams without bottlenecks—

experimental evidence for the physical mechanism of the formation of a jam. *New Journal of Physics*. 10:1-7.

Tokunaga, M., N. Imamoto, and K. Sakata-Sogawa. 2008. Highly inclined thin illumination enables clear single-molecule imaging in cells. *Nat Methods*. 5:159-161.

Weldon, R., K. Scharer, T. Fumal, and G. Biasi. 2004. Wrightwood and the earthquake cycle: What a long recurrence record tells us about how faults work. *GSA TODAY*.

Wilson, N., and P. Lefebvre. 2004. Regulation of flagellar assembly by glycogen synthase kinase 3 in *Chlamydomonas reinhardtii*. *Eukaryotic Cell*. 3:1307-1319.

Supplementary Information is located at the end of the manuscript

Acknowledgements: We thank J. Azimzadeh, L. Holt, C. Tang, H. Madhani, W. Shou, J. Burton, D. Mullins, M. Chan, S. Rafelski, H. Ishikawa, E. Kannegaard, P. Crofts, B. Engel, Z. Apte, and M. Slabodnick for helpful comments on the manuscript and M. Porter and C. Dieckman for providing strains. We thank K. Thorn, A. Thwin, and the Nikon Imaging Center at UCSF for technical expertise on microscopy. Funding for this work was provided by NSF grant 0416310, NIH grant R01 GM097017, the W.M. Keck Foundation Distinguished Young Scholars Program, the Herbert Boyer Junior Faculty Endowed Chair Award (W.F.M.), and NSF Graduate Research Fellowship Program (W.B.L.). Some of this work was supported by the Santa Fe Institute through NSF grant 0200500, entitled “A Broad Research Program in the Sciences of Complexity”.

Author contributions: W.B.L designed and performed experiments, wrote analysis software, performed analysis, and wrote the manuscript. K.A.W. made GFP-labeled strains and did genetic analysis of the strains. K-F.L made GFP-labeled strains and provided advice. G.B.W. provided advice. W.F.M. oversaw and advised the project.

Figure legends:

Figure 1: The IFT train injector produces avalanche-like behavior.

a, TIRF microscopy produces movies of GFP-labeled IFT train movement, which are then converted to kymographs of movement along the flagellar axis. **b**, A median projection across the kymograph at angle θ (theta, red on kymograph), the predominant angle of train movement, produces a smoothed time series of injections. Behaviors such as bursting (orange) and periodicity (blue) are evident.

c, The injector shows quasiperiodicity. We used the time series with a length >50 seconds ($N=37$) to compute the averaged power spectrum. The average is representative of the individual power spectra. The white region shows the relevant portion of the spectrum. Gray shaded regions are frequencies in which the spectrum does not reflect the dwell times between successive injections. The gray regions correspond to effects due to non-adjacent injections (low frequency) and shape of individual peaks in the time series (high frequency).

Figure 2: Measured IFT injection dynamics match dynamics of avalanching systems.

a, In an experimental sand pile, a continuous incoming feed of granules produces a quasiperiodic, discontinuous series of avalanches. In a larger pile, the avalanches are larger and less frequent (Jaeger and Nagel, 1992). **b**, Mean injection magnitude versus the time since the previous injection shows that longer time intervals are associated with larger injections. **c**, Mean injection magnitude

versus the time until the next injection shows that longer times after an injection are associated with larger injections. Error bars are SEM.

Figure 3: Pharmacological and genetic perturbations of the injector do not change injection dynamics but do modify the length-dependent injection rate.

We used the *lf4* mutation (Berman et al., 2003) and lithium treatment (Nakamura et al., 1987) to study the effects of long flagella on the IFT injector, and we used cycloheximide (Rosenbaum et al., 1969) to study the effects of short flagella. **a**, We found no effect on the injection dynamics. We plotted magnitude of each injection event, measured by GFP intensity, versus the time since the previous injection event. The control trend line (solid black) for injection magnitude as a function of accumulation time represents all the data sets well: control (N=130 events; blue dots), CHX (N=55 events; green dots), LiCl (N=72 events; red dots), and *lf4* (N=57 events; yellow dots). **b**, Box and whisker plot of the residual in injection dynamics due to the perturbations. However, examining the injection rate as a function of flagellar length showed a drastic effect on the normal length-dependent injection rate: **c**, Control trend (n=168 flagella; blue dots, black solid line with extrapolation dashed) shows a decrease in the injection rate for longer flagella. Cycloheximide (n=18 flagella; CHX, green dots) decreases the injection rate below the control trend. Lithium chloride (n=38 flagella; LiCl, red dots) and the *lf4* mutation (n=29 flagella; *lf4*, yellow dots) increase the injection rate above the control trend. **d**, A box and whisker plot of the residual for each data set to the

control (blue) trend line shows a significant decrease in CHX (green) and a significant increase in LiCl (red) as well as with the *lf4* mutation (yellow) by multiple pairwise comparison using Bonferroni's correction for alpha (asterisks, ***, indicate $p < 0.0001$). Box and whisker plots: top and bottom of each colored box represent the 25th and 75th percentile respectively. The horizontal line within the box is the median. Whiskers extend to the last data point within 1.5 times the interquartile range. Red crosses represent outlier values.

Figure 4: IFT dynamics are linked to IFT train localization intensity at the flagellar base.

a, an enlarged view of the flagellar base region shows that higher intensity staining for kinesin-II occurs at the base of the regenerating flagella (R) in cells that have a steady state-length flagellum (S) and a regenerating flagellum. Color bar indicates stain intensity ranging from lowest (blue) to highest (dark red). Inset (upper left) gives the cellular context for the magnified views. **b**, the ratio of integrated kinesin-II stain between the flagellar bases of regenerating and steady state length flagella was quantified in 22 control cells with two equal length flagella (ratio in control cells is the lower intensity base to the higher intensity base), 23 single cells with unequal length flagella (ratio in unequal length flagella is the longer flagellum base to the shorter flagellum base), and in 15 view frames comparing one cell with two regenerating flagella to another cell with two steady state length flagella (ratio is the mean steady state base to the mean regenerating

base). Error bars are SEM. In every single case, the regenerating flagella had higher intensity staining at their bases (38/38, $p < 1E-12$, binomial statistic).

Figure 1

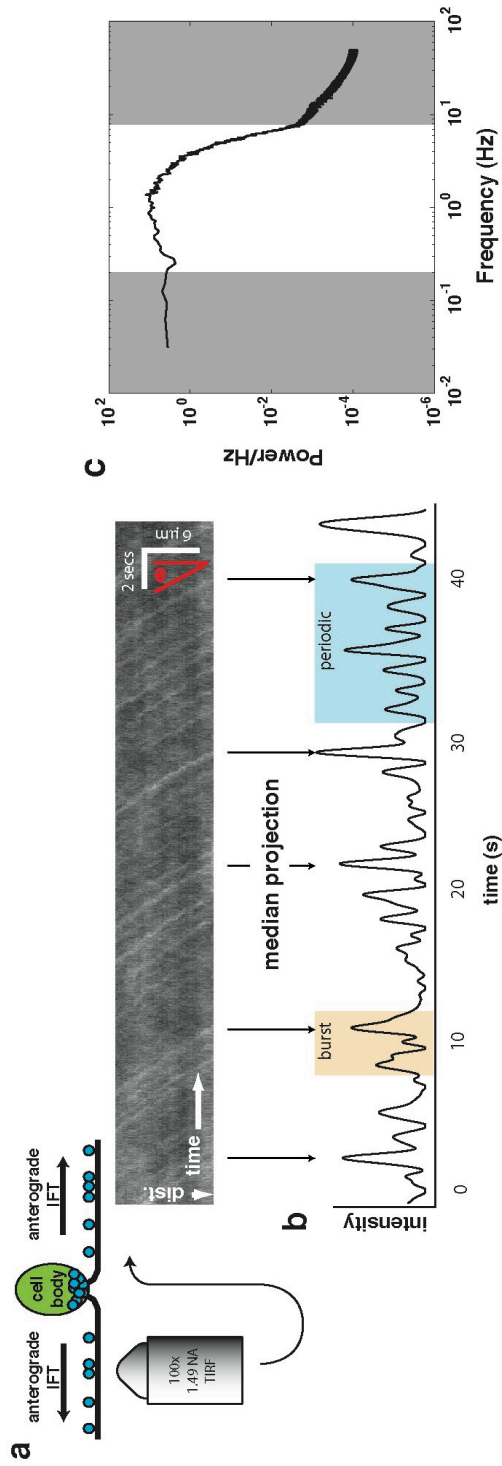


Figure 2

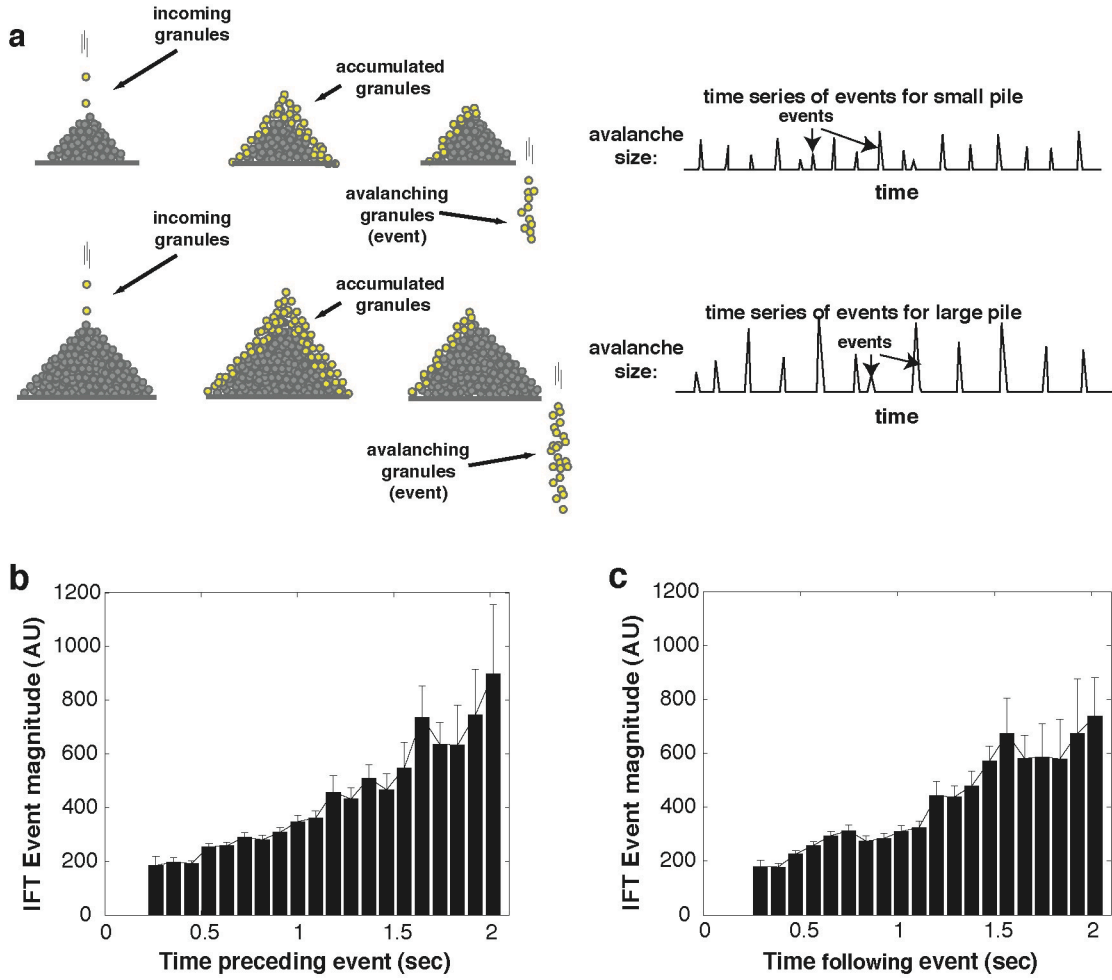


Figure 3

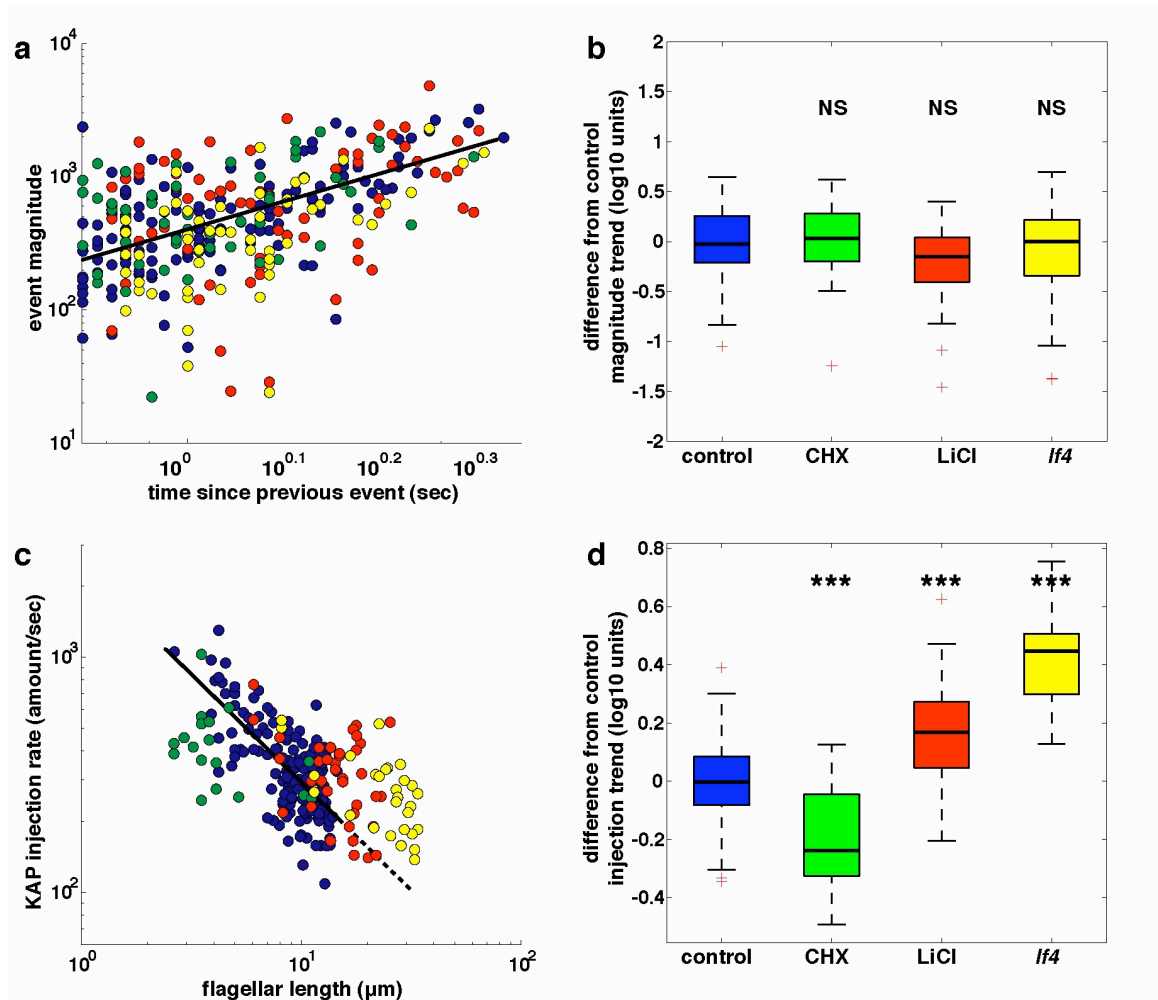
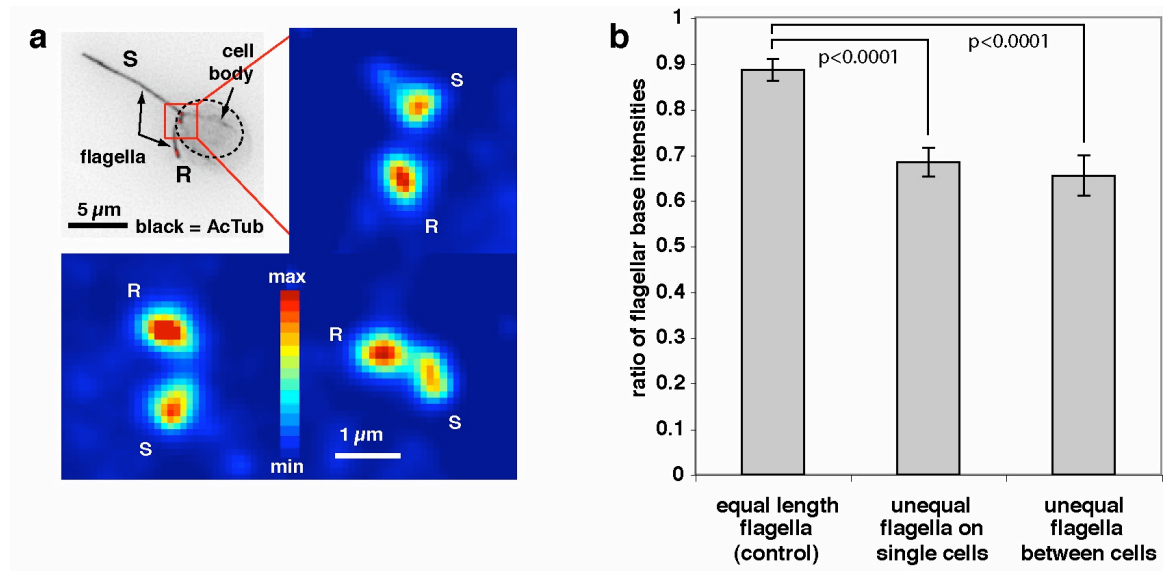
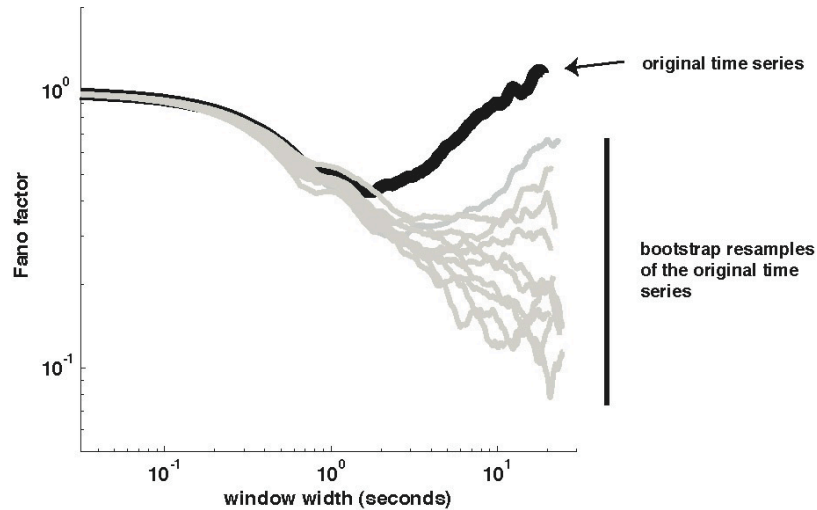


Figure 4



Supplementary Information

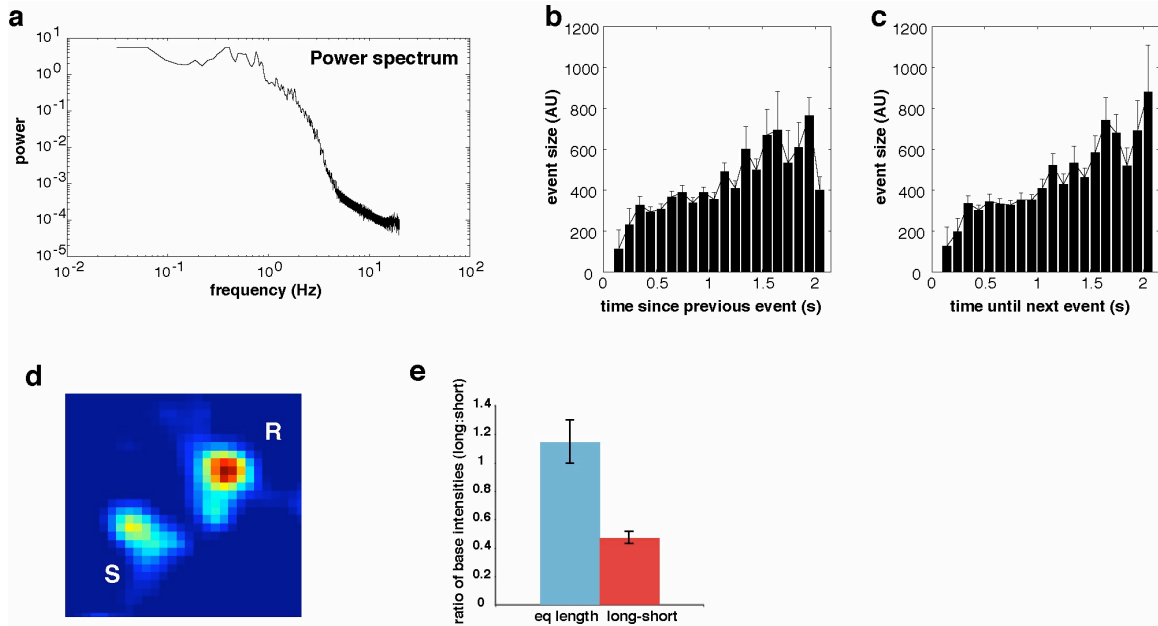
Supplementary Figure 1:



Supplementary Figure 1: Analysis of bursting in IFT:

The Fano factor (i.e. variance in event number divided by mean event number) for a sample injection series (black line) shows an increase at longer time windows. For each time series, 10 bootstrap resamples of the actual injection series (gray lines) were compared with the actual series (black line). The figure gives an example case. An increase in the Fano factor for longer time windows indicates that the injections do not occur as a Poisson process. Therefore, the adjacent events that we observe in an injection series may influence one another.

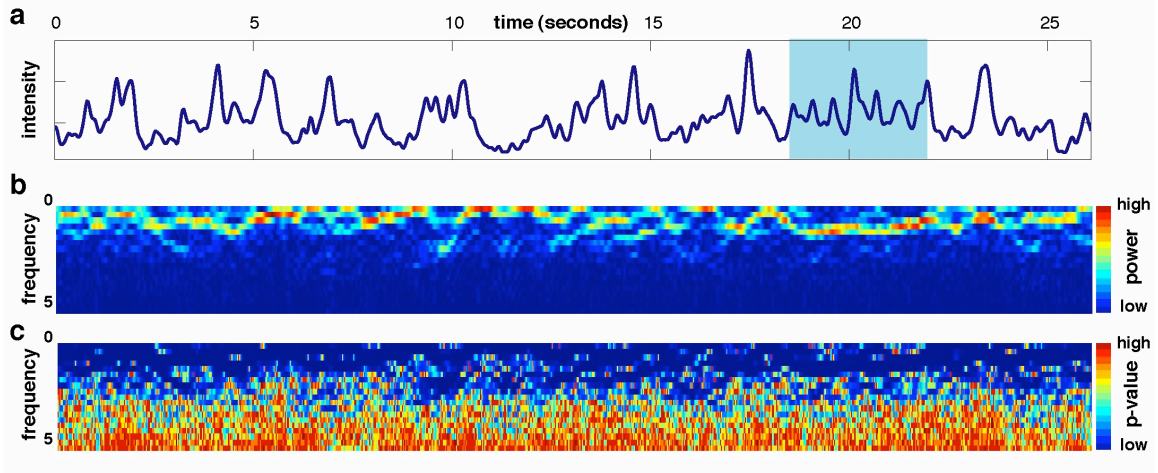
Supplementary Figure 2:



Supplementary Figure 2: GFP-tagged IFT20 shows the same injection behavior as GFP-tagged kinesin II:

a, the power spectrum was calculated by methods used in Fig. 2a. The behavior is similar to behavior seen in the kinesin II time series although false positive traces increase the apparent frequency. **b**, the event magnitude increases with longer time interval since the previous event ($r=0.24$; $p=0$; $N=1367$ events). **c**, the event magnitude is also correlated with the time interval until the next event ($r=0.25$; $p=0$; $N=1297$). **d**, IFT20 accumulates in greater quantities at the base of regenerating flagella ('R') than at the base of steady-state length flagella ('S'). Intensity is represented from highest (dark red) to lowest (dark blue). **e**, quantified intensity ratio of S:R for 5 cells with unequal length flagella and 8 cells with equal length flagella. Error bars show SEM.

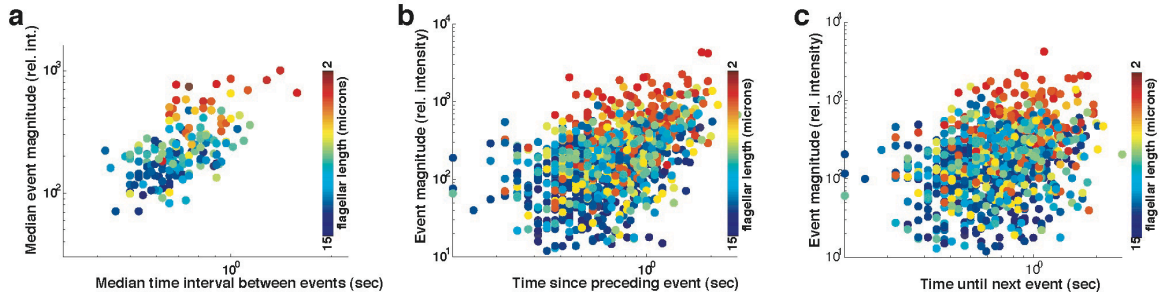
Supplementary Figure 3:



Supplementary Figure 3: Periodicity is transient:

a, the time series analyzed in figure 1. Note the consistent periodic window from ~18-22 seconds (shaded in blue). **b**, the power spectrum was calculated on a rolling 2 second window for the time series shown. The x-axis is time in the time series. The y-axis is frequency. Color indicates power with blue being the lowest and red being the highest. Again, note the consistent periodicity at ~1 Hz for the window from 17-22 seconds. **c**, significant frequencies were calculated using a robust version of Fisher's G-test³⁷. Blue = low, significant p-values. Red = high, non-significant p-values. Note that every time series analyzed (N=218) had significant periodicity at 1 Hz for at least 71.5% of the time.

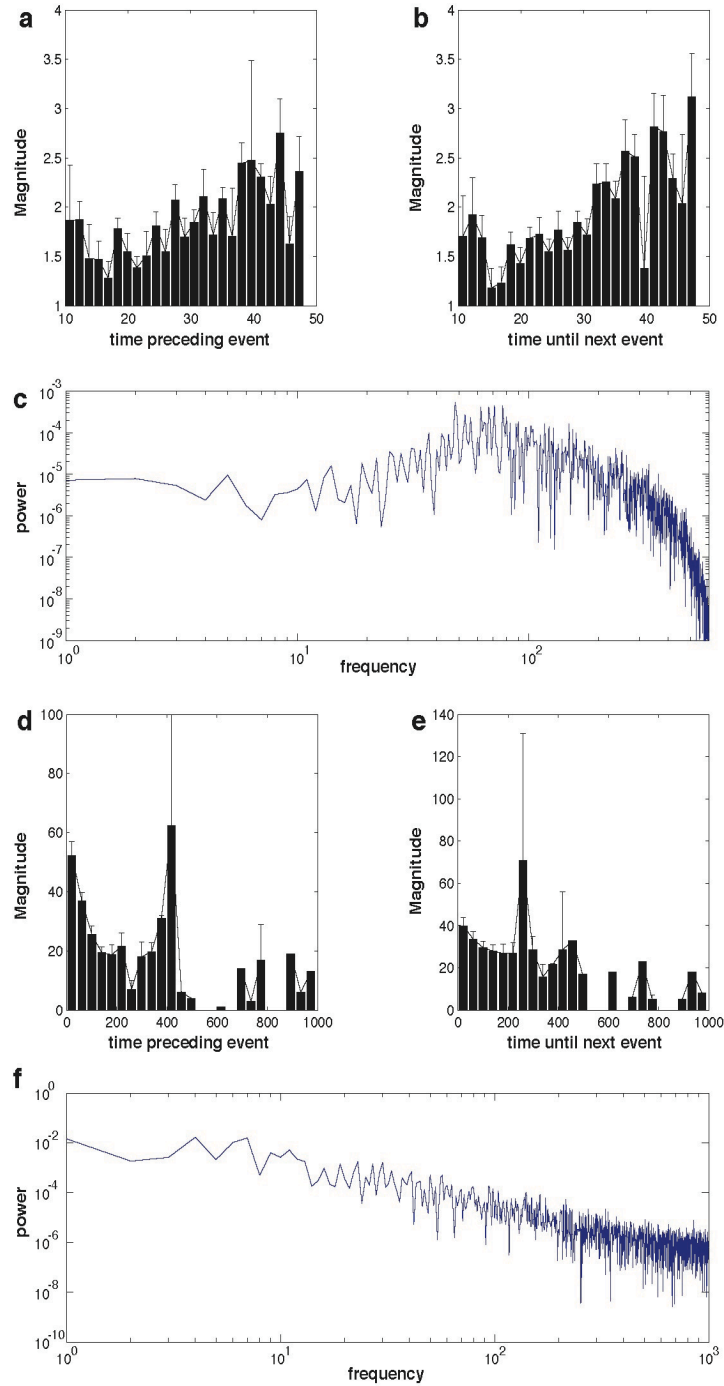
Supplementary Figure 4



Supplementary Figure 4: Injection behavior is length-dependent⁶:

a, median injection event size versus median time interval between injection events on a flagellum-by-flagellum basis (168 flagella). **b**, event magnitude versus time interval since the previous injection for non-burst-integrated data on an injection-by-injection basis. **c**, event magnitude versus the time interval until the following injection for non-burst-integrated data on an injection-by-injection basis for non-burst-integrated data. Flagellar lengths are color coded with blue for long and red for short (see color scale).

Supplementary Figure 5:

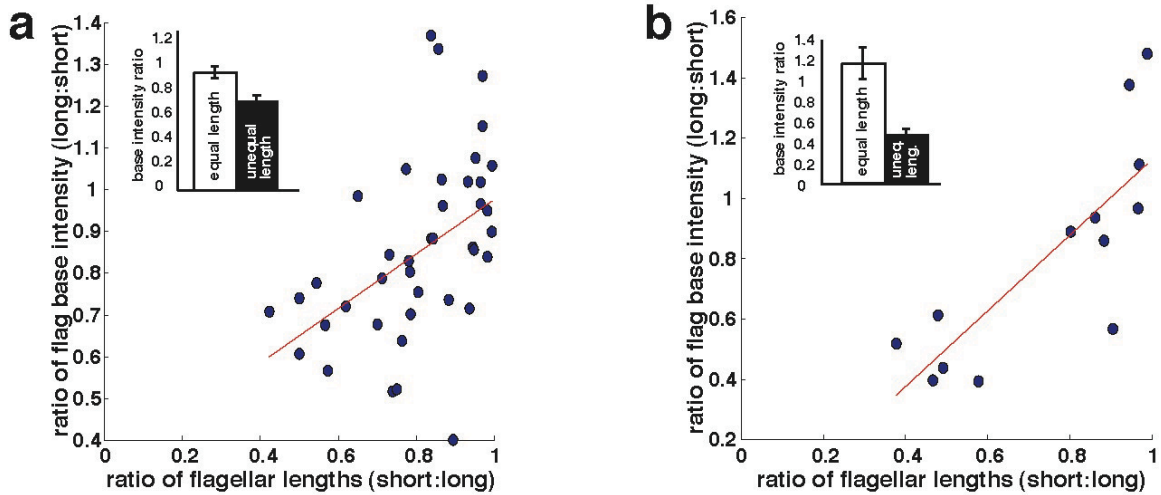


Supplementary Figure 5: Comparison of avalanche and traffic-jam models:

An avalanche model, which stores potential energy, shows similar trends to the data whereas a traffic model, which lacks energy storage, does not match the data.

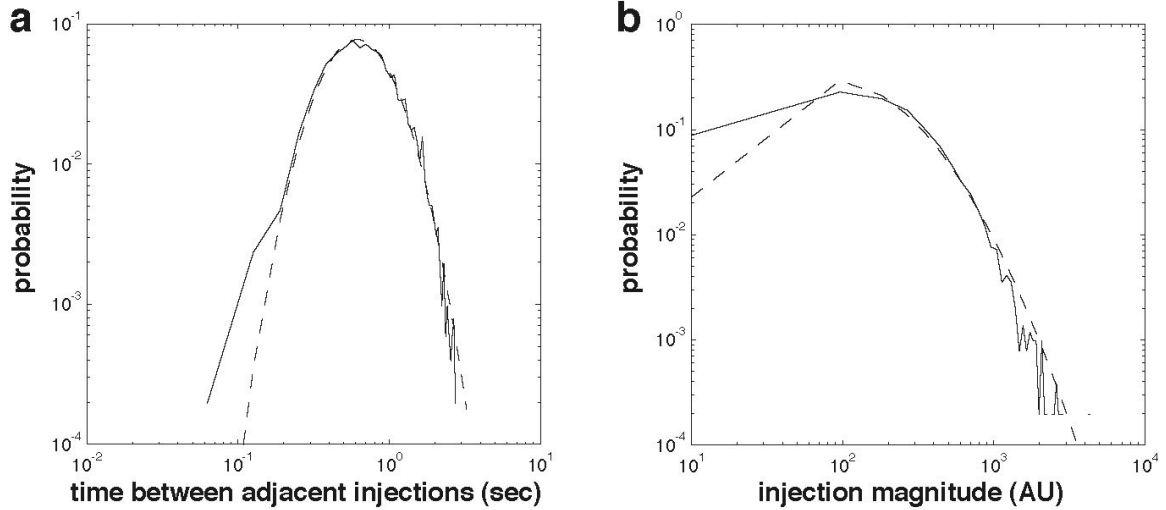
a, in the avalanche model, the event magnitude versus the time interval preceding a release shows increasing event magnitude with increasing time before the release event. **b**, the same trend is seen for the event magnitude versus the time until the next event **c**, the avalanche model event spectrum shows a broad peak, resembling experimental measures of sandpile data⁸, and is similar to the kinesin II and IFT20 data sets. **d** by contrast, in the traffic model, the event magnitude versus the time interval preceding a release shows a slight decrease in magnitude with increasing time before a release event. **e** similarly the same lack of a trend is seen for the magnitude versus time interval following a release event. **f**, the traffic model event spectrum shows no periodicity and, instead, shows power law decay ($\alpha = -1.78$).

Supplementary Figure 6



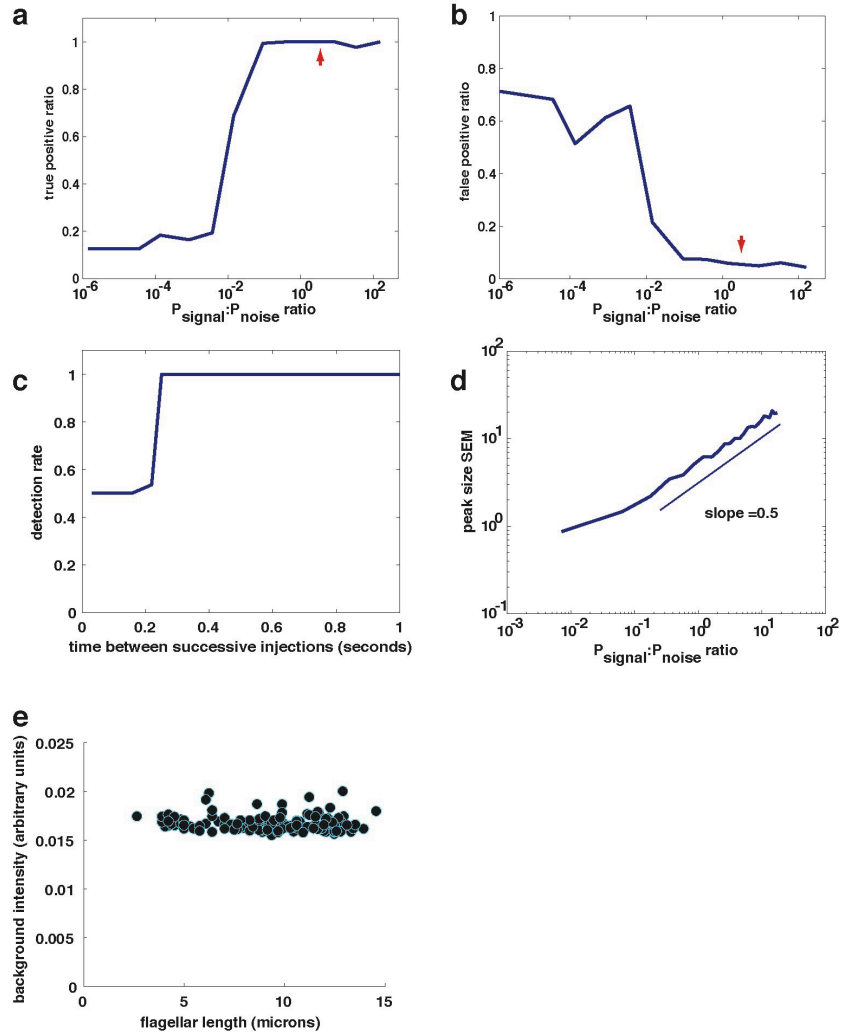
Supplementary Figure 6: More IFT material accumulates at the base of faster-growing flagella: **a**, the accumulated load of kinesin-II is greater at the base of the shorter flagellum in single cells with unequal-length flagella. Inset shows the difference in accumulation where groups have been divided based on a length ratio of 0.8. **b**, the accumulated load of IFT20 is greater at the base of the shorter flagellum in single cells with unequal-length flagella. Inset shows the difference in accumulation where groups have been divided based on a length ratio of 0.8.

Supplementary Figure 7:



Supplementary Figure 7: Distributions of intervals and magnitudes for non-burst-integrated injection events. **a**, the distribution of time intervals between adjacent injections (solid line) fits well with a lognormal distribution (dashed line). **b**, the distribution of injection magnitudes (solid line) fits well with a lognormal distribution (dashed line) at larger magnitudes. However, it is a much broader distribution than the time interval distribution and is dominated by its tail, whereas the intervals distribution is narrow and dominated by its center.

Supplementary Figure 8



Supplementary Figure 8: Kymograph processing algorithm performance evaluated using model convolution: we made synthetic kymographs, varying the signal:noise ratio from $1.4E-6$ to 156, and then evaluated **a**, the ratio of true positive, and **b**, false positive calls, as a function of the signal:noise ratio. The algorithm functions well above a signal:noise ratio of 0.1. We estimate the actual

signal:noise ratio to be 2.5 (red arrows). Based on these performance tests, we should see 5% false positives and 100% true positives. We calculate the false positive ratio as the number of wrong calls divided by the total number of calls. The true positive ratio is the number of correct calls divided by the number of possible correct calls. **c**, to evaluate the time resolution, we evaluated the algorithm performance over varying input frequencies to determine how close together injections can be before they are merged into a single event by the algorithm. Synthetic kymographs were made with doublet injections 1 second apart. The spacing between the peaks in a doublet was varied from 0.03 seconds to 1 second. The algorithm performs well for intervals 0.25 seconds and above, while shorter intervals cause the adjacent injections to be merged into a single event. **d**, we also calculated the standard error in estimating injection size as a function of the signal:noise ratio. As injections get larger, the error in estimating their absolute size increases as the signal:noise ratio to the $\frac{1}{2}$ power. **e**, The background intensity subtracted is roughly constant as a function of flagellar length ($r=-0.09$, $p>0.24$, $N=168$ flagella).

Materials and methods

Strains and cell culture:

Results reported in the main body of the paper were derived from a KAP-GFP rescue of the *fla3* mutant, generously provided by Mary Porter (Mueller et al., 2005). A backcross to CC125 (Chlamydomonas Stock Center) showed no strain-dependent effects (data not shown), and an *lf4*/KAP-GFP/*fla3* strain was produced by mating and PCR-based genotyping. The *lf4* strain used was allele *lf4*-V86, a generous gift from the Dieckmann lab. The strain was verified by genomic PCR, and absences were found in the 5' region and throughout the coding region.

An IFT20-GFP rescue of the null IFT20 mutant was described (Lechtreck et al., 2009). The IFT20 strain showed a similar injection trend for injection magnitude versus time preceding and time following an injection as was seen with KAP-GFP (Supplementary Fig. 2), but the strain showed a less steep variation in injection rate as a function of flagellar length because the increased intensity of retrograde IFT trains makes background subtraction less precise. Similar features to the KAP-GFP strain were observed for bursting and periodicity in this strain (Supplementary Fig. 2).

All strains were grown on TAP agar plates and then transferred to M1 liquid media under continuous light for 12-36 hours before fixation or live cell imaging. Lithium chloride (Sigma) was prepared in a 1 molar stock in M1 media and used at a 25 mM working concentration in M1. Cells were incubated for 1 hour in LiCl before imaging. Cycloheximide (Sigma) was prepared as a 10mg/mL stock in

ethanol and diluted to a 10 $\mu\text{g}/\text{mL}$ working concentration. Cells were incubated a minimum of 10 minutes in cycloheximide before imaging. A 1:1000 ethanol in M1 media control showed no significant effect on IFT traffic by methods of Fig. 3 (Akaike information criterion gave 100% probability of a single trend line for both comparisons; Student's T-test for distance from the control trend line gave $p>0.25$).

Fixation:

Methanol fixation was performed as previously described (Feldman and Marshall, 2009). In Fig. 3, cells were stained with primary anti-GFP and secondary anti-mouse, labeled with rhodamine. In Supplementary Fig. 5, cells were incubated with anti-GFP (unlabeled) and imaged in the FITC channel for GFP with no secondary stain. Similar results in the FITC channel were achieved by methanol fixation and overnight incubation in 10% block with no primary antibody (data not shown).

Live cell deflagellation and flagellar regeneration:

Cells were deflagellated by passing log-phase culture through an insulin syringe (28 gauge, 1cc) in M1 culture media. 0.5mL of culture was first drawn rapidly into the syringe, causing cavitation of the media. The culture was then forced rapidly from the syringe back into a 1.5mL Eppendorf tube. For long-zero experiments, regeneration proceeded for 15 minutes in the Eppendorf tube before fixation. For TIRF microscopy, cells regenerated on the coverslip.

Live cell Imaging:

Live cell imaging was performed on a Nikon te2000 microscope with a 100x 1.49 NA TIRF oil lens and 488 nm laser illumination through an optical fiber with a near-TIRF illumination field. Emitted light from the sample was reflected to the camera using a 514 nm dichroic mirror and a 525 nm filter. Images were recorded at 29.7 frames per second on a Photometrics QuantEM EMCCD camera with 157 nm per pixel. In a set of experiments to control for effects of the illumination field, an identical microscope setup with a Yokogawa C-22 spinning disk was used. TIRF and spinning disk confocal imaging gave similar trends for the injection magnitude versus the time intervals preceding and following an injection, although we did not make a statistical comparison because the two illumination fields produce different injection intensities.

The TIRF field was calibrated for each imaging session by adhering 100nm orange fluorescent beads (Phosphorex Inc) to a coverslip and then setting the TIRF angle to give a mean bead intensity of 75% the maximum fluorescence intensity detected (minimum 45 beads per view frame). To accomplish this, we imaged the beads over a range of 50 laser angles from below TIR (all light reflected) to above TIR where all of the light is transmitted. The mean bead intensity was calculated at each angle using custom MATLAB software. Then, the mean bead intensity versus laser angle was plotted. The curve shows a characteristic increase up to a maximum and subsequent sharp drop off in intensity as the laser angle increases significantly above TIR. We found empirically that by setting the angle to give a mean bead intensity of 75% the

maximum, we could exclude the cell bodies from the illumination field while getting clear illumination of the entire flagellum. Tokunaga *et al* (Tokunaga et al., 2008) described this technique of near TIR illumination at length. This method produces roughly constant flagellar background intensity over a range of flagellar lengths (Supplementary Fig. 8e).

Cells were allowed to adhere their flagella to the coverglass and then imaged at 29.7 frames per second. The KAP-GFP cells were imaged under two slightly different microscope configurations (RAM in the control computer was increased and the dichroic mirror was replaced). The first set contains 168 control flagella, 18 cycloheximide-treated flagella, and 39 lithium chloride-treated flagella, while the second set contains 50 control flagella and 29 *lf4* flagella.

Because the replacement dichroic mirror produces very slightly higher signal:noise, we made an equivalent adjustment in the image processing background removal and smoothing parameters in order to allow direct overlay of the two control sets. We compared the two control data sets by the methods in Fig. 3 and found no significant difference. Using the Akaike Information Criterion there is 100% chance that the two data sets are drawn from the same set, and by looking at the deviation from the control trend line for injection rate versus flagellar length, the deviations are not significantly different by two sample t-test ($p=0.66$). The larger data set was used for injection magnitude versus time preceding and following injection plots because more data points are available. The second set was taken with increased RAM. Therefore this set has longer time

series and, accordingly, these results are presented for power spectrum analysis. However, both sets give equivalent spectra (data not shown).

IFT kymograph analysis:

Kymographs were made using hand traces of the flagella in Nikon elements (v3.1) to delineate the initial position of the flagellum. Kymographs were then converted to IFT injection time series using custom MATLAB software with the algorithm in Fig. 1 (Ludington and Marshall, 2009), using the following specific parameters. We found empirically that the background was best approximated as a constant component plus a photobleaching component. The constant background was estimated as the kymograph minimum and subtracted from the time series (Supplementary Fig. 8e). We then estimated local background as the local time series minimum on a 1.5 second window and then normalized the time series to this local background to account for photobleaching. This step detrends the time series and serves as a high pass filter. The time series were then smoothed using 2 iterations of a running median filter with a window width of 3 pixels followed by 1 iteration with a running mean filter of window width 3 pixels.

Injection times were determined automatically as the local maxima in the time series. The minimum size injection that we scored was determined by comparing time series maxima to kymograph traces by eye to determine what intensity could reliably be scored as an injection. From this comparison we set the threshold peak intensity at 0.015 relative intensity units. Injection peak sizes were then calculated as the area under the peak while the time series intensity was greater than 0.68x

the local peak maximum. Injection sizes were then normalized to the minimum peak size and only injections greater than 10x the minimum injection intensity were counted in the analysis.

The parameters used were determined using the ratio of true positives and the ratio of false positives as a function of the signal:noise ratio to optimize results produced from synthetic data. The signal:noise ratio was calculated as the square of the ratio of signal amplitude to noise amplitude. Signal amplitude was calculated as the total signal amplitude from the smoothed time series, and noise amplitude was calculated as the total amplitude in the time series after subtracting the smoothed signal amplitude.

We next asked how the observed signal to noise ratio affects our analysis. To do so, we generated synthetic kymograph data sets using a model convolution approach (Gardner et al., 2010) by resampling the injection series from the real data, convolving the synthetic series by the point-spread function of the microscope, and then adding background and noise to the level measured empirically in the background of real flagella. We then built synthetic data sets over a range of signal:noise values representative of the real dataset (Supplementary Fig. 8). Over the range of measured signal:noise, the highest false positive rate was 6% and the lowest true positive rate was 98%, with a maximum total error of 8%. At the mean signal:noise of the data set, the true positive rate was 100% with 6% false positives. The algorithm tends to have a very high true positive hit rate due in part to the median projection across the kymographs.

Taking the median projection greatly reduces the rate at which noise obscures the true signal. Though this method is simple and robust, it does limit the type of kymographs that can be input: there must be a consistent IFT velocity for all trains over the entire flagellum for the entire course of the time series. Therefore, we manually selected time series where the IFT velocity was consistent over the entire kymograph.

In terms of total injected material detected, the algorithm detects 98.4% of the actual input from synthetic data when realistic noise is overlaid on the synthetic kymographs. However, on an injection-by-injection basis, the accuracy is lower, and this inaccuracy increases for larger magnitude injections (Supplementary Fig. 8d).

Missed observations by this analysis would appear as smaller magnitude injections for a longer time interval. Undoubtedly, some false negatives occur, but the magnitude versus preceding time interval plot suggests these are rare (see Supplementary Fig. 4b).

For Supplementary Table 1, in order to measure the amount of time the injector spends in the open versus closed state, for each time series we counted the open time as the time for each peak where the intensity remains above 68% of the peak maximum. For bursts, we counted the entire burst duration as open time. We counted the remainder of the time series as closed time. The ratio of open:closed time was then calculated for each time series and compared to the injection rate for each time series using Pearson's correlation coefficient. This result is

presented for the gated channel model in the discussion section ($r=-0.12$, $p=0.09$, $N=218$ flagella).

Burst integration:

Burst integration involves determining at what time resolution the actual events in a time series are occurring. To take the sand pile analogy, we could count individual grains in an avalanche as events, or we could count events as all of the grains that hit the scale within a certain threshold time interval (see Fig. 1a). For the sand pile, we want to count the avalanches as events, so we integrate grains to get a time series of avalanches. A technical problem occurs when the distribution of intervals between avalanches overlaps with the distribution of intervals between individual grains hitting the scale. This problem is common in ion channel time series, where channel-opening events of two different types overlap in their distributions. An optimal solution, in terms of trade-off between types of errors, is to find a cutoff interval threshold where the events lost from each of the distributions are equal (Magleby and Pallotta, 1983). In our data, we determined the threshold time interval of 0.26 sec by fitting a sum of two lognormal distributions to the interval time histogram, with the two distributions representing time intervals between bursts (greater mean) and between injections (lower mean). The threshold interval was then set where area in the tail of the within-burst distribution extending above the threshold was equal to the area in the tail of the between-burst distribution extending below the threshold. Injections

occurring less than the threshold time apart after the previous injection were then merged into the previous injection. Some time series began or ended in the middle of a burst. These time series were truncated to eliminate the partial bursts.

Power spectrum calculation:

For power spectrum calculation, we only analyzed time series that had a length of at least 50 seconds (N=37 time series). For Fig. 2a, the power spectrum of background-corrected time series was calculated directly using Fourier-based methods in MATLAB. For Supplementary Fig. 3, power and significance were assessed using an adaptation of the algorithm of Ahdesmaki *et al* (Ahdesmaki *et al.*, 2007).

Fixed cell imaging:

Fixed samples were imaged on a Deltavision microscope at 100x with filters for FITC and Rhodamine channels. Z-stacks were acquired with a 0.2 micron z-step. Deconvolution was performed using Deltavision software and z-stacks were made for further analysis.

Injector intensity quantification:

Custom software was written in MATLAB. Manual segmentation was used to identify cells and IFT injector regions. For each cell, background was subtracted from the z-stack as the mean intensity of the pixels in the 3D bounding box perimeter, and then pixels with intensity greater than one-eighth the maximum intensity were summed to give injector intensity. The one-eighth cutoff was

chosen because it consistently produced a good visual overlap with the injector region.

Intensity ratios in the control, single cell, and multiple cell comparison samples (Fig. 4, Supplementary Fig. 5) were compared by one-way ANOVA and then multiple pairwise comparisons were made using Bonferroni's correction for alpha.

Models:

A one-dimensional agent-based traffic model was formulated based on the molecular motor-based transport model presented in Chowdury *et al* (Chowdhury *et al.*, 2005). Briefly, a linear track of 500 motor binding positions was established. Motor are then selected at random to step forward one position along the track. Motors that reach the end of the track then enter a pool of motors that can enter the track at position 1. A motor only moves if the position in front of it is unoccupied. Jams develop randomly and jam magnitude is taken to be the number of contiguous motors in a jam after 100,000 time steps.

A one-dimensional Burridge-Knopoff spring-block model for earthquakes (Burridge and Knopoff, 1967), formulated based on the Huang and Turcotte model (Huang and Turcotte, 1990) was produced with simplified dynamics that would apply at low Reynolds number. Briefly, at each time step, the driving block moves forward by a set amount. The two sliding blocks are coupled to each other and to the driving block by springs. The sliding blocks experience friction with a uniform probability proportional to the length of their surface in contact with the floor. When the spring force exceeds the static frictional force constant on a

sliding block, the block moves based on the ratio of forces until the force drops below the sliding friction force constant. The output is the magnitude of the movements of one of the sliding blocks over time. The dynamics are similar to the original model when the loading rate is set in the higher range relative to the frictional component.

Statistics:

All statistical tests were performed in MATLAB using the Statistical Analysis Toolbox except where indicated. Akaike Information Criterion model selection tests were performed using custom MATLAB software to test whether one line or two lines give a better fit to 2D point scatters. All correlation values given are the standard Pearson product-moment correlation coefficient (r). P-values for correlation are for the test of whether the correlation is non-zero, where $p=0$ gives 100% certainty of a non-zero correlation.

Supplementary Table 1

Model	hypothesis	data in support	data against
(a) entry-gated pore	Pore opens when more material is needed (frequency-modulated control)	--	1. the injection rate is uncorrelated with the amount of time that material is entering the flagellum
(b) border checkpoint	Larger trains take longer to enter because more cargo must be checked	1. injection magnitude is correlated with the length of the time interval preceding the injection	1. injection magnitude is correlated with the length of the time interval following the injection 2. bursting is not explained 3. periodicity is not explained
(c) constant accumulation rate and random release timing	Material accumulates at the entry point at a constant rate. The gate opens at random time intervals and lets all of the accumulated material in.	1. injection magnitude is correlated with the length of the time interval preceding the injection	1. injection magnitude is correlated with the length of the time interval following the injection 2. bursting is not explained 3. periodicity is not explained 4. a standing load of material is present at the flagellar base
(d) biochemical clock	A biochemical oscillator at the base controls entry timing.	1. periodicity	1. bursting 2. the frequency changes as the injection rate changes 3. larger accumulation gives slower dynamics 4. no explanation for the regulation of IFT train size

Supplementary Table 1: Several alternative biochemical models do not explain our results. Dishinger *et al* (Dishinger et al., 2010) presented evidence that several biochemical regulators of the nuclear import system are at work in the mammalian cilium. Thus, a potential model for the injector is that of **a**, a regulated entry channel, with open and close times set by a flagellar length-dependent control system (i.e. the channel opens more often when the flagellum needs more material). This model predicts a strong positive correlation between the injection rate and the percentage of time where IFT trains are flowing through the pore. In fact, we observe an insignificant negative correlation ($r=-0.12$, $p=0.09$, $N=218$ flagella). Another nuclear import-type model is **b**, a border crossing model, where larger trains take a longer time to transit the pore because each subunit in the IFT train takes a finite time to transit the pore. So, longer trains take longer to enter. That type of model correctly predicts the correlation between the injection size and the time interval preceding an injection (Fig. 2b,c; Supplementary Fig. 4). However, such a model does not account for the bursting behavior (Supplementary Fig. 1), the correlation between injection size and the time interval following an injection (Fig. 2c), or the periodicity that we observe (Fig. 2a). The same is true for a trivial model in which **c**, IFT material accumulates at a constant rate and then releases into the flagellum at random times. Such a mechanism could explain the correlation between injection size and preceding time interval but cannot explain the bursting, periodicity, or correlation between injection size and following time interval. Similarly, we believe that **d**, a simple biochemical oscillator does not explain the apparent periodicity due to the

bursting dynamics (Supplementary Fig. 1), the broad distribution of time intervals between injections (Supplementary Fig. 7) and overall inconsistent timing behavior.

Chapter 4

**Microscopy methods for
amputating single flagella from
biflagellate *Chlamydomonas
reinhardtii* cells and observing
their subsequent recovery**

Collaborators: **Linda Shi¹, Qingyuan Zhu¹, Michael Berns^{1,2}**

1. Dept. Bioengineering, University of California, San Diego
2. Beckman Laser Center, University of California, Irvine

Synopsis:

As stated in the introduction section, it became desirable to amputate single flagella from biflagellate cells and watch them recover. This chapter describes the methods I developed to do that. First, there are methods to perform laser microsurgies using the microscopes built by Qingyuan Zhu and Linda Shi in Michael Berns' lab at UC San Diego. Second, there are the methods using CellASIC microfluidics to immobilize many wildtype *Chlamydomonas* cells for hours at a time while maintaining them happy and healthy. The Introduction of this chapter covers the motivation for developing these methodologies. The Results and Discussion section covers how these methods were developed and observations that could be of use to future investigators.

Introduction:

Chlamydomonas reinhardtii cells possess two flagella of roughly 12 microns length, which emanate from a pair of basal bodies that are docked at the plasma membrane as well as to each other through connecting fibers. Experiments performed by Rosenbaum *et al* (Rosenbaum et al., 1969) showed that severing of one of the two flagella induced shortening of the remaining one. This response was termed the “long-zero” response because after amputation, there is one long flagellum and one zero-length flagellum. In the ensuing recovery, the long flagellum shortens as the zero flagellum regenerates. When the two flagella are equal in length (roughly 9 microns at 20 minutes post-amputation), the long flagellum begins growing at the same rate as the zero flagellum, and the two equilibrate at steady state length (roughly 12 microns) after around three hours (Figure 1a).

There are two main interpretations of this result. The first suggests that an active shortening program initiates in the long flagellum when its pairmate is amputated (Baldwin et al., 1984; Pan et al., 2004). The second interpretation suggests that the shortening of the long flagellum is due to competition for components between the two flagella (Coyne and Rosenbaum, 1970; Marshall and Rosenbaum, 2001; Marshall et al., 2005; Rosenbaum et al., 1969). The three main pieces of evidence in favor of the active shortening hypothesis are (1) “overshoot” behavior, where the long flagellum shortens to a shorter length than the regenerating zero flagellum. This behavior apparently occurs quite frequently, though Rosenbaum *et al* (1969) fail to state precisely how frequently. The

overshoot is interpreted to be due to a failure to terminate the shortening program at the proper time (Baldwin *et al* 1984). The second (2) piece of evidence in favor of the active shortening hypothesis comes from cells that possess more than just the single pair of flagella. Baldwin *et al* (1984) found that in *vfl3* cells, which have more than two flagella, there was no induction of shortening when flagella that were not paired at their base were severed. This experiment seems to indicate that rather than sharing structural proteins through the cytoplasmic pool of protein, which would not depend on flagellar pairs, instead the flagella in a pair are programmed to be the same length, so that when one flagellum in a pair is amputated, it's pairmate tries to shorten to equilibrate length (Baldwin *et al* 1984). Note that this would be an important functional program because cells with unequal-length flagella have greatly impaired swimming efficiency.

The last (3) evidence comes from Junmin Pan and Bill Snell's groups, where a build up of a kinesin13 homolog has been observed at tips of shortening flagella (Pan and Snell, 2005). Kinesin13s induce microtubule shortening from the plus (+) end. In their studies, Pan and Snell found that kinesin13 localized to flagella when shortening was induced.

The competition [or sharing] hypothesis can account for overshoot by imposing some sort of lag in sharing material between the flagella. I carried out simulations using delay differential equations to show this basic behavior occurs (Figure 1b-c). The lag can be interpreted as due to damage incurred by the long flagellum base as the amputation occurred. Amputations by previous investigators were performed by either slowly squishing cells between two pieces of coverglass until

one but not both flagella popped off (Rosenbaum *et al* 1969), or subjecting them to mechanical shearing in a Waring Blender (Baldwin *et al* 1984). A possibility is that these conditions cause damage to the cells beyond the pop off of one flagellum (e.g. cytoskeletal filaments that help deliver IFT particles to the flagellar base could be ruptured as well). When I repeated the initial 1969 experiments using their methods, the squishing had to be quite severe (changing cell diameter by approx 2x) before any flagella would pop off (data not shown), suggesting that this method may be somewhat invasive for the cell.

The competition model cannot explain result (2) from Jarvik's group, where unpaired flagella on *vfl3* cells do not show the long-zero response. The third result from Pan and Snell (2005) can be explained in the competition model if the kinesin13 is always at the flagellar tip. However, I attempted to repeat Pan and Snell's (2005) results using the kinesin13 antibody they used in their paper. The antibody they sent showed very poor localization and only slight, diffuse staining at the flagellar tips. Essentially, I could not repeat these results.

Because of results (1) and (2), "overshoot" and the case of unpaired flagella provide difficulty for the competition hypothesis, I sought to study them further in order to determine how they arise. My first step was to repeat the original long-zero experiments. There were two experimental improvements that I made. First, I used motile, wildtype cells to conduct my experiments. The Rosenbaum 1969 paper used paralyzed mutants, which have defects in axonemal structure and therefore could introduce genetic artifacts. To this end I developed a microfluidic trap, which keeps mobile cells immobile and healthy for at least 14 hours. The

second improvement I made was to use a minimally invasive amputation system. To do this, I collaborated with the Berns lab at UC San Diego and used their laser microsurgery system, which they routinely use to sever microtubule bundles and chromosome tips in mitotic mammalian cells with no detriment to cell viability. The Results and Discussion section details my efforts to these methodological ends. Chapter 4 covers the main biological results.

Results and Discussion:

Laser severing produces “pop off”

I used two different custom-built, robotically controlled, laser cutting microscopes in the Berns lab, RobolaseIII and RobolaseIV. Cutting on RobolaseIII is powered with a 490 nm picosecond laser while RobolaseIV is powered with a variable wavelength 700-800 nm IR femtosecond laser (Figure 3).

When I targeted the flagella on a cell by either laser, they popped off of the cell. Individual flagella were also targeted, generating healthy long-zero cells that regrew their missing flagella in 1-2 hours. This “pop off” response held regardless of where the flagellum was targeted along its length from the base, just outside the cell wall, all the way to the very tip. Pop off was not triggered when the media adjacent to the flagellum was hit, nor did cell body targeting trigger pop off. Notably, most hits to the cell body, particularly those in the chloroplast region, caused cell death within 20 minutes if not instantaneously, as assayed by cessation of contractile vacuole pumping.

It was possible to sever a flagellum, but pop off followed within a split second. The laser power required to pop off a flagellum was roughly half of that required for cutting, though the exact power after objective was not measured for severing on Robolase III.

Laser power and duration required to induce pop off

We measured the laser power after objective to induce the pop off response on RobolaseIV at 110mW at 730 nm with a 30 ms shutter opening time. Pop off was

reliably triggered at this level, but less power did induce pop off with lower effectiveness.

Fa1 does not pop off but dies when it is severed

In an attempt to induce regeneration of half length flagella, as was done by Tamm (Tamm, 1967) in *Peranema*, we surveyed a range of mutants for their ability to not pop off flagella hit by the laser. It was my original hope to measure the regeneration rates in flagella of different lengths to determine whether the rate was length-dependent or time-dependent as Tamm had done in *Peranema*. With the Berns lab, I tried many mutants as well as CC125 and CC124 wildtype cells in calcium-free media. Severing without pop off was only possible in the *fa1* mutants, but these cells died within about 20 minutes of severing. No long zero response was observed in these cells. Cells in calcium free media became sickly, and while we could cut their flagella, the cells all resorbed their flagella on their own without laser perturbation. Therefore we could not study the long-zero response in these cells either. No other strains that we checked could have their flagella severed without inducing the pop off response. These strains include *lf4*, *lf1*, *lf2-1*, *lf2-5*, *lf3*, *asq2*, *vfl1*, *vfl2*, *vfl3*, *ptx2*, *ptx8*, *eye2*, *eye3*, *pfl6*, *pfl8*, *KAP-GFP rescue of fla3-1*, *wt CC124*, *wt CC125*, *wt CC1009*.

CellASIC Y2 microfluidic chamber holds cells in place with flow and cells recover normally from pH shock deflagellation

Chlamydomonas cells swim at roughly 100 microns per second. Because I wanted to measure the flagellar length recovery kinetics in live, motile, wildtype cells, I tested many strategies to immobilize wildtype cells. These methods included

trapping between two coverslips as in Rosenbaum *et al* 1969, mounting in 0.5% agarose, and using a CellASIC microfluidic chamber. The microfluidic chambers worked the best because they maintained cells in continuous good health by constantly perfusing fresh media over them. When media flow was shut off, cell health began to deteriorate, as evidenced by flagellar resorption and/or failure to regenerate flagella after pH shock. The Y2 plates from CellASIC, which were designed for yeast, worked best. Cells accumulated along the borders between chamber heights, specifically at the 4 to 4.5 micron border and at the 4.5 to 5 micron border (Figure 4). Working in the Berns lab, these cells maintained good health and grew in diameter for as long as we imaged them, and we even found freshly divided cells in the chambers when we allowed the culture to continue overnight.

We induced deflagellation by pH-shock and found that the flagellar recovery kinetics in the chamber are normal (Figure 5).

Cells slide along the chamber boundaries, making them difficult to follow

A flaw in the CellASIC design is that accumulated cells along the dividers between different chamber heights slide along the boundary, perpendicular to the flow direction. Though the cells do not leave the chamber and can be followed, it makes it difficult to determine which cell is which and occasionally obscures flagella. Therefore, I worked with CellASIC to design a custom, *Chlamydomonas*-specific trapping plate (Figure 6a).

Custom design holds motile cells in place while maintaining cell health

Cells in the custom plate, called the CHLAMY plate, stay in place and are easier to image and perturb than in the Y2 plate (Figure 6b).

Flow induces minor but quantifiable length changes

In order to test what effect trapping has on *Chlamydomonas* flagellar length, I worked with a summer student, Jay Serebrenick, to quantify changes in flagellar length at different flows over time. A note of caution should be taken in interpreting the following results because there was contamination of the CellASIC plates during the manufacturing process. Therefore, the flows may have been influenced and more importantly, secondary metabolites from the large mats of bacterial contaminants were present in the microfluidic channels.

That note of caution taken, we found a small 1.4 micron decrease in flagellar length at low and high flow velocities (3 mm/s and 10 mm/s respectively). We found a small, insignificant 0.3 micron increase in flagellar length at 7 mm/s after 2 hours. Flow velocity was calculated by imaging the speed of 1 micron beads flowing through the chamber. Briefly, we took images of the beads under flow with a fixed shutter speed. The length of the tracks made by the beads allowed calculation of the flow speed.

In order to test whether flagellar calcium channels were responsible for the length changes, we repeated the experiments in the *ptx2* mutant (Pazour et al., 1995), provided in collaboration with George Witman's group. In this mutant we found starkly different length changes, namely a significant ~3 micron decrease in

length at 3, 7, and 10 mm/s, indicating that flagellar calcium channels may influence the flagellar length change in response to flow.

In order to test whether flagellar motility played a role, we tested the *pf16* mutant under the same 3 flow conditions. *pf16* cells increased flagellar length by an insignificant 0.6 microns at 3 mm/s, and they decreased their length by ~3 microns at 7 and 10 mm/s. Though these results do not paint a clear picture of the flagellar length response to flow, they do indicate that *pf16* has a different response to flow than does the wildtype CC125 strain and suggest caution in using mutants by these methods.

We also checked whether the drag influences flagellar length response to flow. If flagellar calcium channels open in response to drag from the media flowing past the flagella (Pan et al., 2005), increasing the viscosity of the media should induce these same length responses at a lower flow rate. In accordance with the hypothesis, when we doubled the viscosity to 2 centiPoises using methylcellulose, we saw a large decrease in flagellar length by 3.5 microns on average. Control cells not subjected to flow had no significant length change in the 2 centiPoises media ($p > 0.97$, $N = 50$ cells each in 1cP and 2cP M1 media).

Overall, our results indicate that caution should be taken in setting the flow rate through the CellASIC chambers and that control cells should be left with intact flagella during regeneration in order to rule out flow-induced length changes influencing the results. Note, however, that in subsequent experiments in chambers free of contamination, we have not observed a significant length change in control cells, indicating that our current methods are good and reliable.

Our results also indicate that flagellar calcium channels in *Chlamydomonas*, such as *ptx2* may be a good model for studying the ciliary length response to fluid flow in the CellASIC CHLAMY chamber.

Good quantification of long-zero response

The initial reason for developing these methods was to study the long-zero response in greater detail. To that end I used laser severing combined with microfluidic trapping to amputate single flagella from over 100 cells, and I imaged their kinetics of recovery. The results of those experiments are presented in Chapter 4. The methods allow good quantification of the long-zero response, however, improvements could be made to the trapping design to allow better clearance of debris, and many problems have been encountered due to manufacturing defects that are not readily apparent until the plate is put to use.

Problems encountered due to CellASIC manufacturing defects

The first of these defects is poor adhesion of the PDMS to the coverglass, which causes spillage of fluid between channels. This defect is most readily apparent after running fluid through the chamber for about 30-90 minutes at which point liquid begins to collect on the top of the PDMS, having traveled through the gas exchange channels.

The next most common defect is a clogging of channels, presumably due to use of excess adhesive. This defect is readily apparent, as cells cannot be loaded due to the low pressure in the plate.

The last common plate defect is debris from manufacturing stuck in the chambers or channels (Figure 7). This defect is most apparent during cell loading. Cells enter the chamber but they are not able to distribute in the imaging area due to flow blockage by the debris. The debris can often be seen before loading, but sometimes it is not visible in the chamber until the loading flow is switched on. It appears as clear, smooth, irregularly-shaped beads as well as fibers.

Therefore, it has been necessary to work around the defects and use the plates that have the least-problematic defects. Debris limits the number of cells that can be imaged simultaneously, and poor adhesive material makes the plates last around 2 hours. Both of these defects still allow the plates to be used. When plates have minimal defects, they work excellently.

Materials and methods

Strains and culture methods:

All strains were acquired from the *Chlamydomonas* stock center (University of Minnesota) except *asq2*, which was made by Jessica Feldman and available in the Marshall lab, and the KAP-GFP rescue of *fla3*, which was a generous gift of Mary Porter.

Cells were grown in either standard TAP or M1 liquid media (see *Chlamydomonas* Sourcebook).

Microscopy:

Light microscopy was performed on a Zeiss Axiovert 200 using the custom configuration shown in Figure 2. Imaging was performed using a 40x NA 1.4 lens and Phase contrast 3 filters and a Hamamatsu CCD camera with 6 pixels per micron. Measurement of flagella was performed by hand-tracing in ImageJ (various versions).

Microfluidics:

CellASIC microfluidics were operated per manufacturer instructions with the following modifications in the Y2 plate. After cell loading, the cell loading well (C) was cleaned out using fresh media. The flow rate was then set at 0.1 psi and cells were held in place against the barriers in the chamber by perfusing media from the cell loading well (C), rather than from the normal media wells (A and B). To do pH shock, the low pH media was loaded into well C then washed out in order for regeneration to proceed.

References

- Baldwin, D.A., M.R. Kuchka, B. Chojnacki, and J.W. Jarvik. 1984. Approaches to flagellar assembly and size control using stumpy- and short-flagella mutants of *Chlamydomonas reinhardtii*. *In* Molecular biology of the cytoskeleton. D.W.C. Gary G. Borisy, Douglas B. Murphy, editor. Cold Spring Harbor Laboratory, Cold Spring Harbor, New York. 245-255.
- Coyne, B., and J.L. Rosenbaum. 1970. Flagellar elongation and shortening in *Chlamydomonas*. II. Re-utilization of flagellar proteins. *J Cell Biol.* 47:777-781.
- Marshall, W., and J. Rosenbaum. 2001. Intraflagellar transport balances continuous turnover of outer doublet microtubules: implications for flagellar length control. *Journal of Cell Biology.* 155:405-414.
- Marshall, W.F., H. Qin, M. Rodrigo Brenni, and J.L. Rosenbaum. 2005. Flagellar length control system: testing a simple model based on intraflagellar transport and turnover. *Mol Biol Cell.* 16:270-278.
- Pan, J., and W.J. Snell. 2005. *Chlamydomonas* shortens its flagella by activating axonemal disassembly, stimulating IFT particle trafficking, and blocking anterograde cargo loading. *Developmental Cell.* 9:431-438.
- Pan, J., Q. Wang, and W.J. Snell. 2004. An aurora kinase is essential for flagellar disassembly in *Chlamydomonas*. *Developmental Cell.* 6:445-451.

- Pan, J., Q. Wang, and W.J. Snell. 2005. Cilium-generated signaling and cilia-related disorders. *Lab Invest.* 85:452-463.
- Pazour, G.J., O.A. Sineshchekov, and G.B. Witman. 1995. Mutational analysis of the phototransduction pathway of *Chlamydomonas reinhardtii*. *J Cell Biol.* 131:427-440.
- Rosenbaum, J.L., J.E. Moulder, and D.L. Ringo. 1969. Flagellar elongation and shortening in *Chlamydomonas*. The use of cycloheximide and colchicine to study the synthesis and assembly of flagellar proteins. *J Cell Biol.* 41:600-619.
- Tamm, S. 1967. Flagellar development in the protozoan *Peranema trichophorum*. *Journal of Experimental Zoology.* 164:163-186.

Figures

Figure 1a: Long-zero flagellar length kinetics

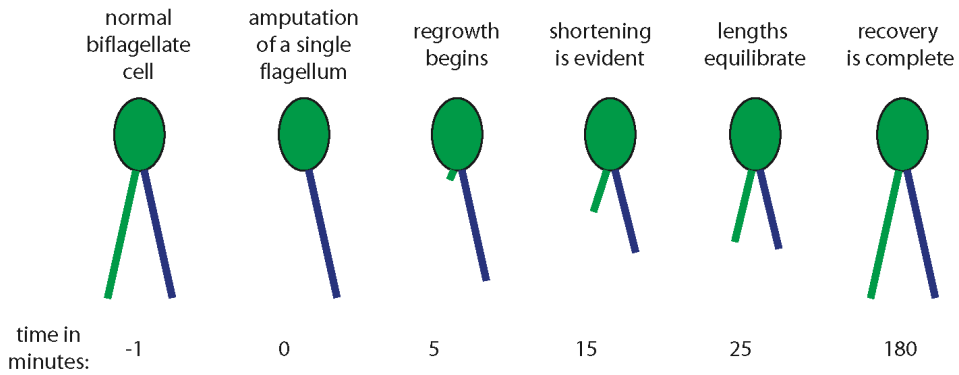


Figure 1b: Model prediction of flagellar length recovery after single flagellum amputation

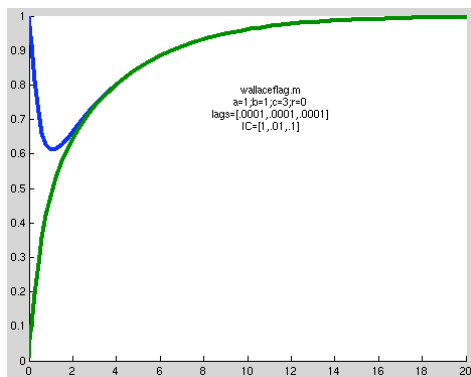


Figure 1c: Model prediction with a lag factored in produces “overshoot” behavior

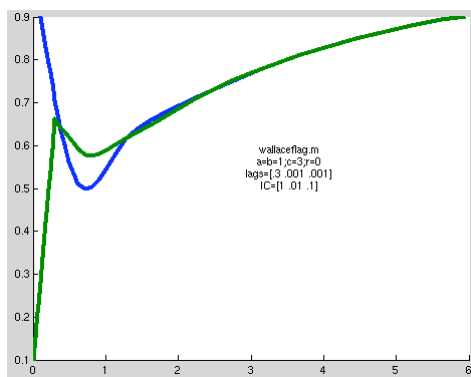
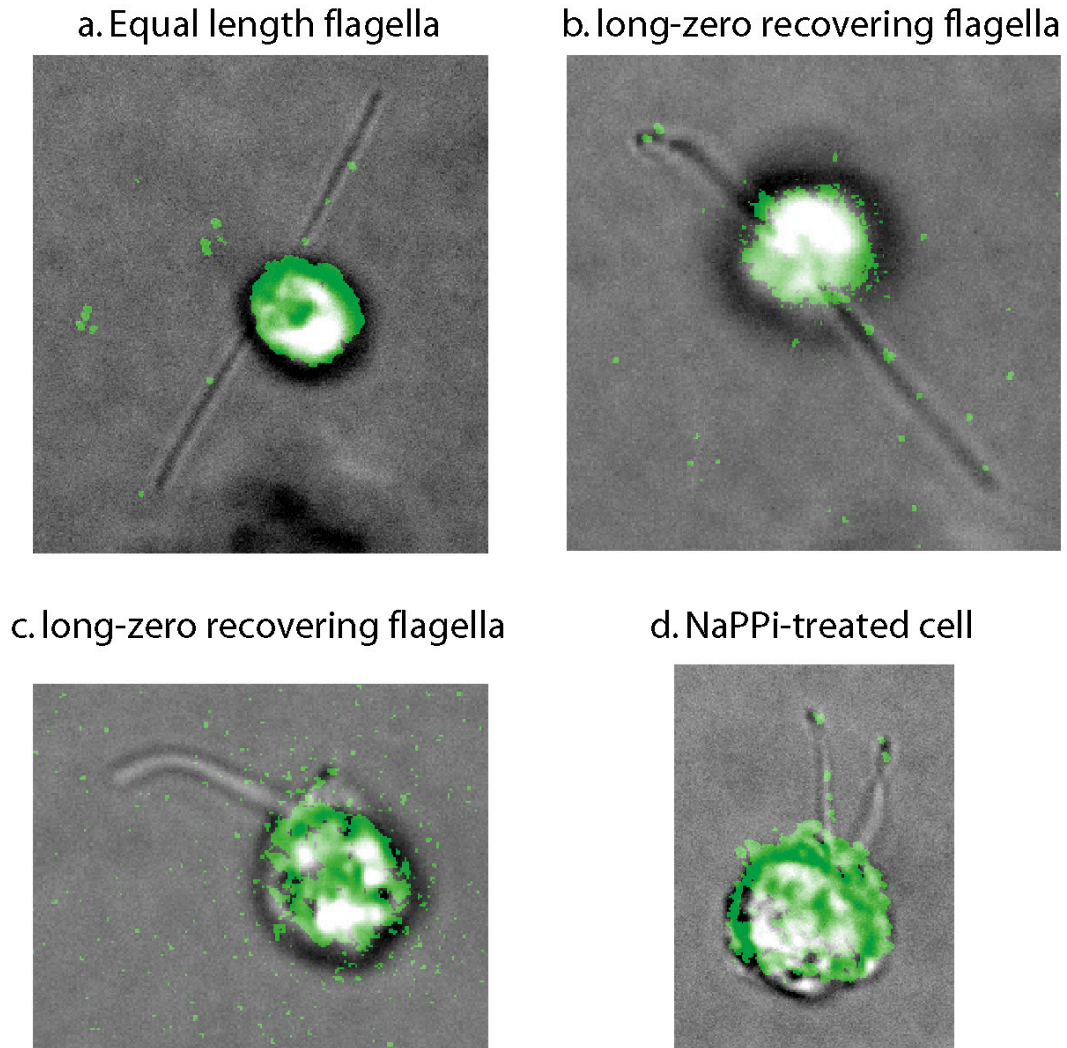


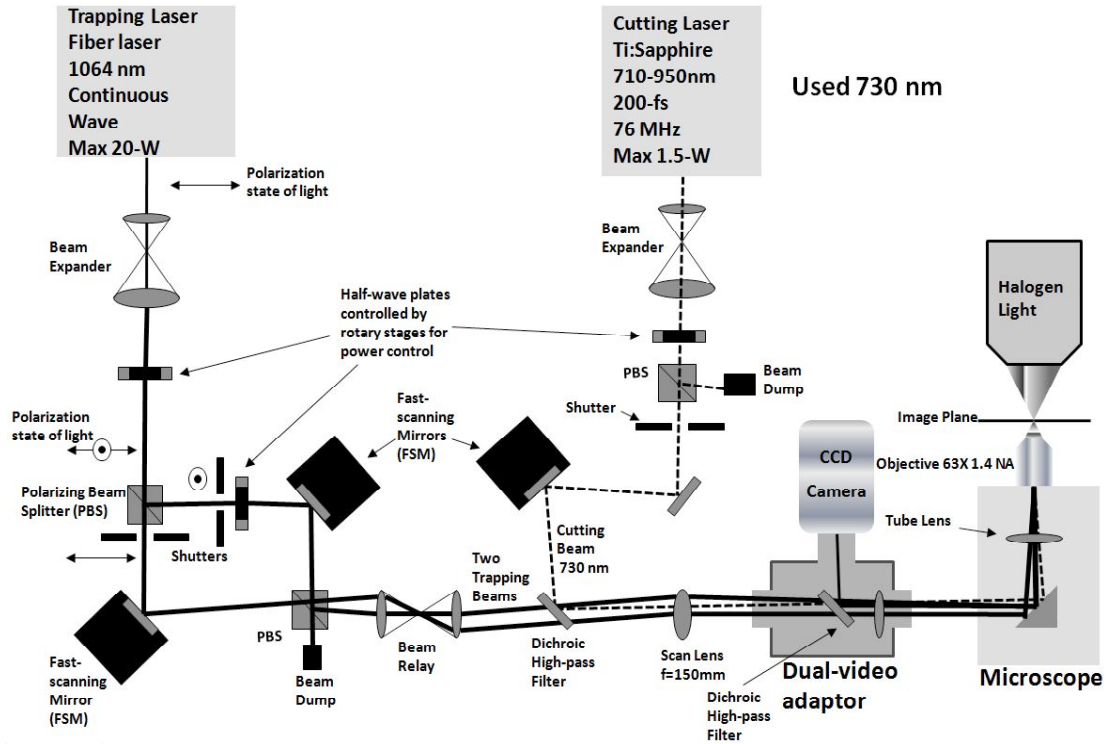
Figure 2: Results with CrKinesin13 antibody are inconclusive



CrKinesin13 antibody was a generous gift of Bill Snell's lab. Attempts to repeat the localization experiments were not fruitful. Although some diffuse staining is visible at the tips of the NaPPi flagella, the signal had to be increased above reasonable gain in order to observe this staining. No staining could be seen at the tips of shortening long-zero flagella, indicating that even if the kinesin13 is responsible for shortening when NaPPi is added, it is not present during long-zero-induced shortening.

Figure 3: Berns lab at UC, San Diego, Robolase IV

Optical Setup of the System



Qingyuan Zhu designed and built the microscope hardware. Linda Shi designed and built the microscope software. We cut and imaged using a 40x 1.4 NA lens.

Figure 4a: CellASIC Y2 yeast microfluidic chamber design layout © CellASIC.

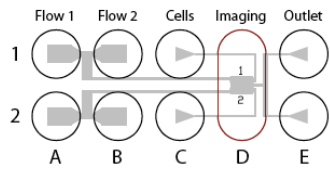


Figure 1 Well Layout

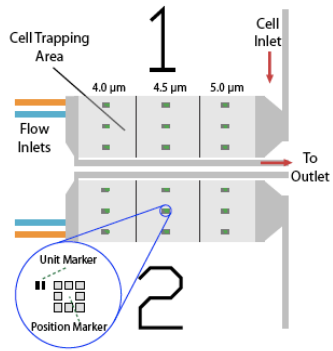


Figure 2 Trap Area

Figure 4b: *Chlamydomonas* wildtype CC125 cells in the Y2 chamber at the boundary between 4.5 and 5 microns. Cutting is performed and regeneration is apparent. The cells are tracked for 4 hours in this particular experiment.

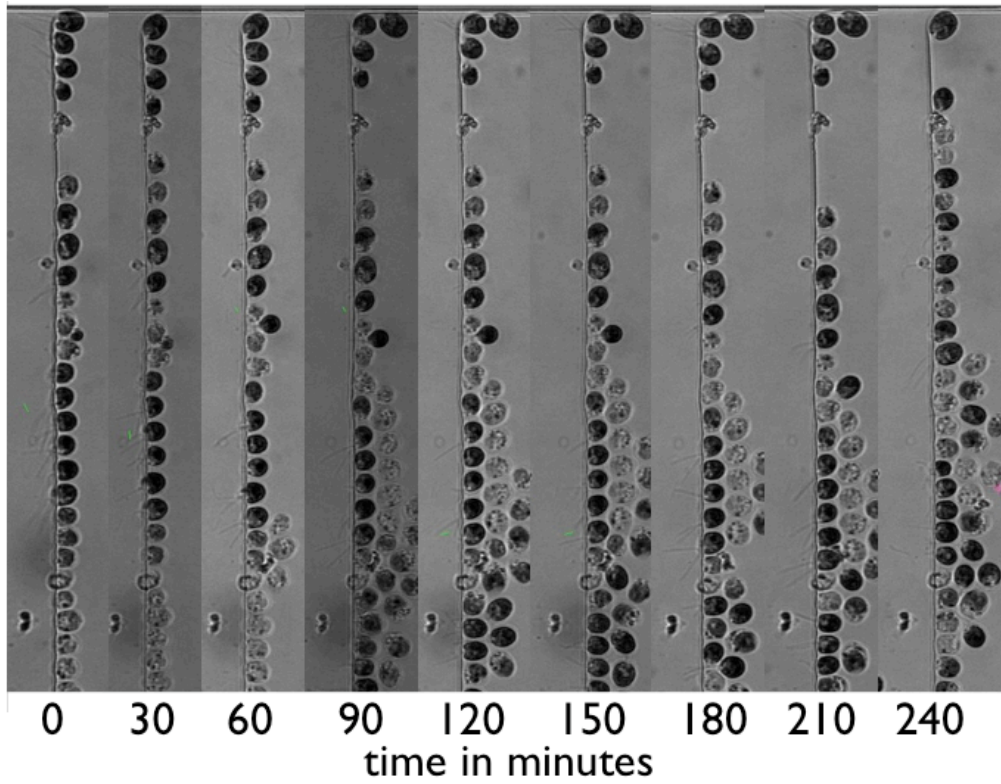
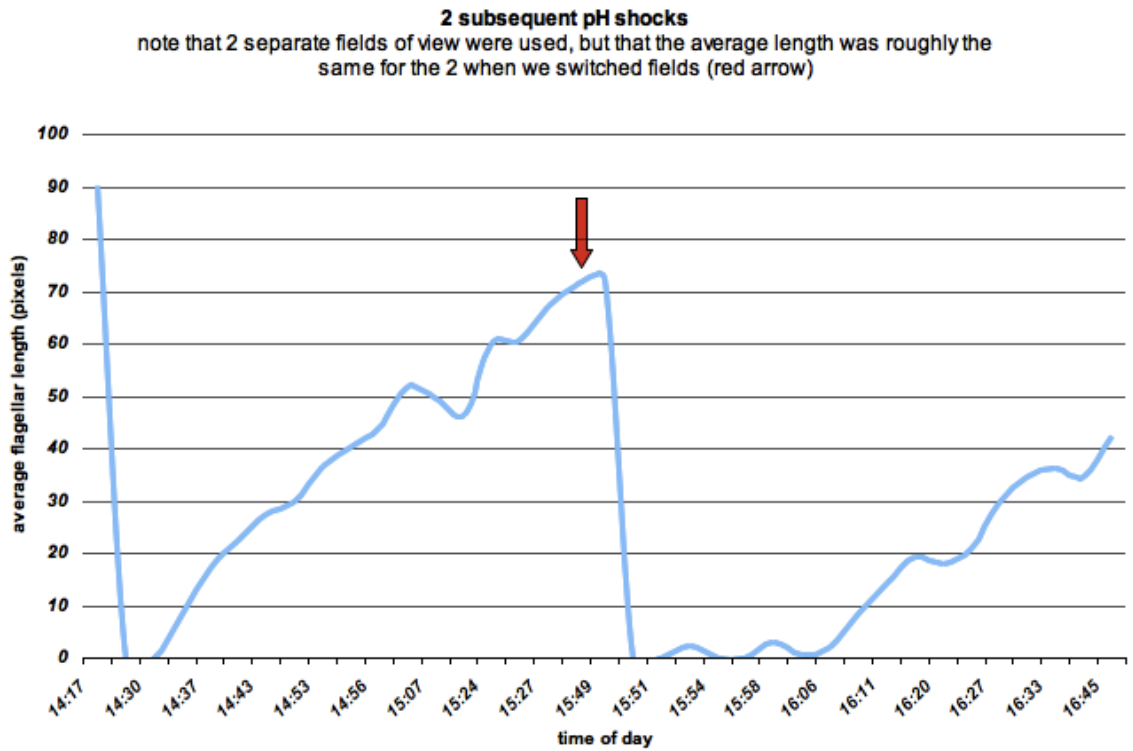


Figure 5: pH shock regeneration is normal in the Y2 chamber



pH shock was induced in synchronous cells by flow switching from TAP media at pH 7.4 to pH 4.5 for 100 seconds, at which point deflagellation was evident.

Median of least 10 flagella from 10 cells is given for each time point. When 75% length recover was reached after 1 hour and 20 minutes, deflagellation was again induced by pH shock.

Figure 6a: A custom CellASIC plate was designed to facilitate better trapping and flow switching © CellASIC.

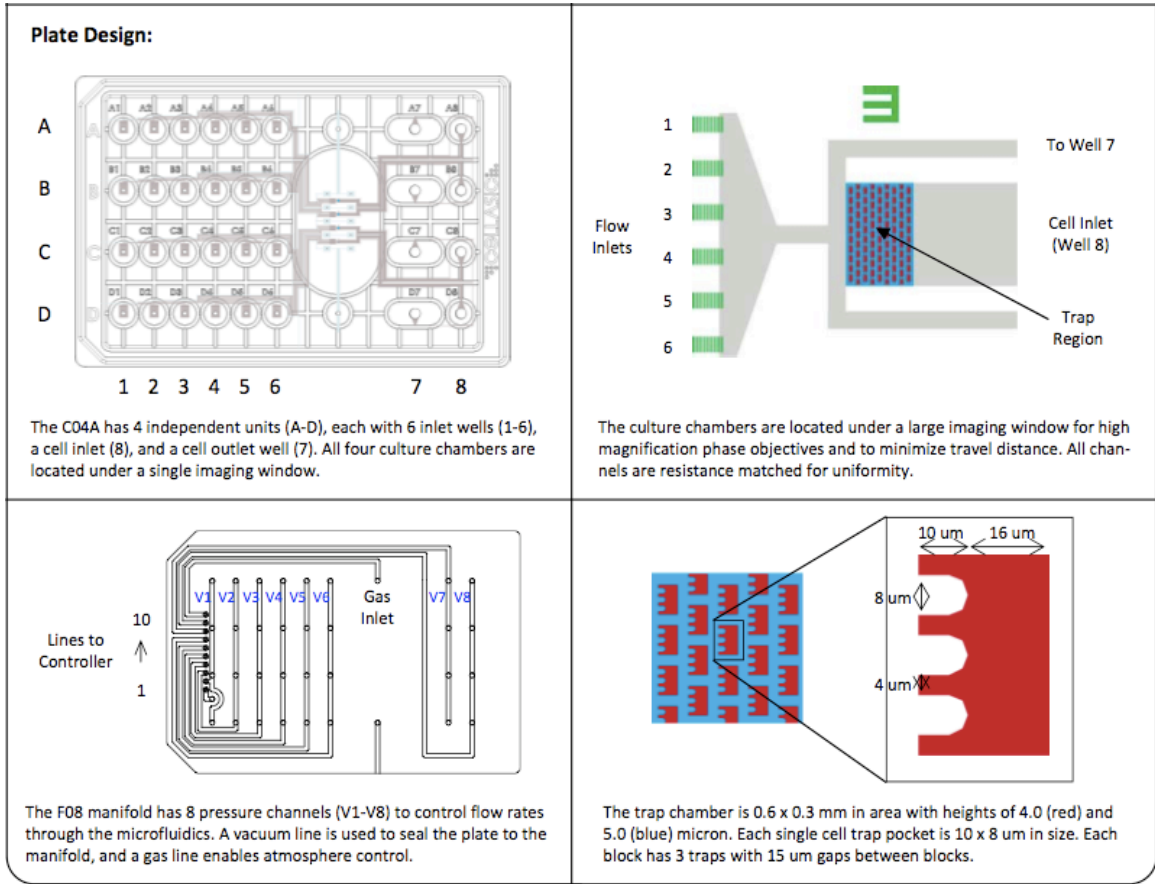


Figure 6b: wt CC125 *Chlamydomonas* cells were loaded into the custom plate

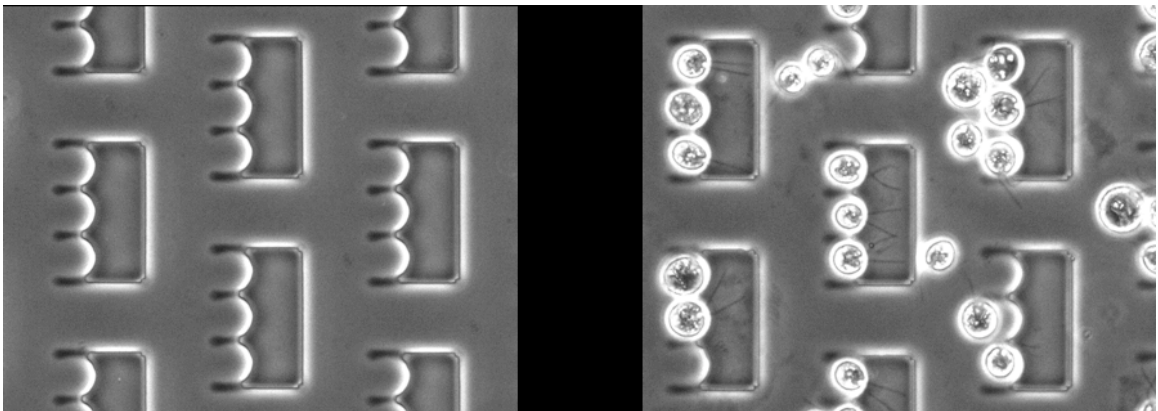
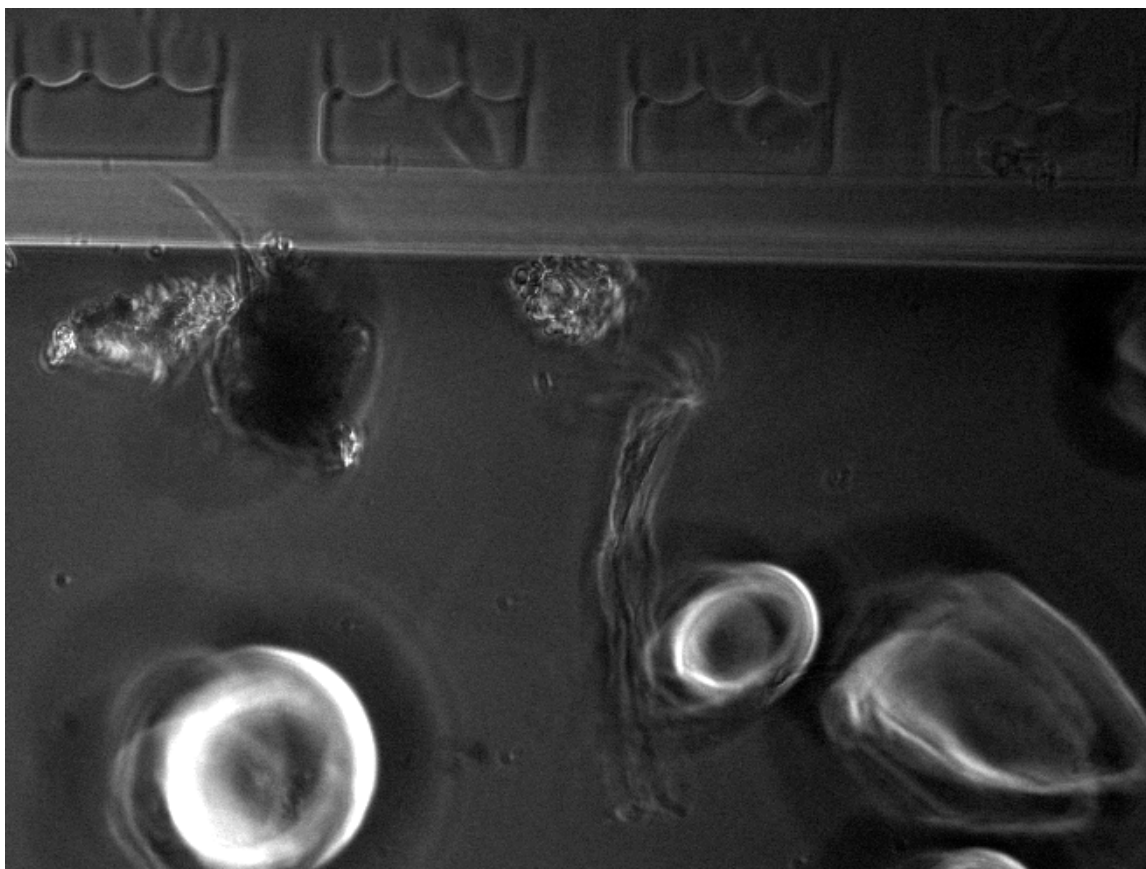


Figure 7: Debris in the CellASIC CHLAMY plate due to ongoing manufacturing problems



Chapter 5

A general model for dynamic organelle size control based on laser microsurgical perturbation studies of cilia

Collaborators: **LZ Shi**¹, **Q Zhu**¹, **MW Berns**^{1,2}

Affiliations:

1. Dept of Bioengineering. University of California, San Diego
2. Beckman Laser Institute. University of California, Irvine

Synopsis: This chapter describes the flagellar length control system. Using methods developed in Chapter 3, I show that the system manages length by a simple consistent method, which does not comprise separate ciliogenesis, maintenance, and shortening programs. The results inspire a general model for dynamic organelle size control in which organelles semi-autonomously self-assemble, but ultimate size control is regulated by the availability of precursor material.

Abstract:

Cilia and flagella are microtubule-based organelles that make a filamentous projection from the cell body. Length defects in these organelles generate a wide range of congenital human defects ranging from polydactyly, polycystic kidney disease, and blindness to mental retardation (Badano, Mitsuma et al. 2006).

Though cilia and flagella appear to be static structures, it has been shown that they are subject to continuous turnover of their structural components (Stephens 1997; Stephens 2000). Therefore, understanding how these dynamic organelles maintain a constant length is fundamental to cilia, flagella, and how they work in our body. Classical experiments in *Chlamydomonas reinhardtii* showed that when one of the two flagella was amputated, the other flagellum began to shorten while the amputated flagellum regenerated, a behavior known as the "long-zero response" that was interpreted as the activation of a special flagellar shortening response in the longer flagellum (Rosenbaum, Moulder et al. 1969). Here we developed microfluidic trapping and laser microsurgery techniques in *Chlamydomonas* to repeat the classical long-zero experiments under more controlled conditions. We see that cells consistently recover from the perturbation by shortening the unperturbed flagellum and regenerating the amputated one until the two reach equal length, at which point they both grow back to almost full length. This result held true for wildtype strains CC125, CC124, and CC1009, as well as in unpaired flagella in the mutants, *vfl2* and *asq2*, and in wildtype cells that possess four flagella due to incomplete cell division. In contrast to earlier reports of long-zero response, the longer flagellum never became shorter than the

regenerating flagellum during the response, suggesting that such "overshoot" behavior was a byproduct of reduced cell viability, which our microfluidic system overcame. We used our results to build a computational model of the flagellar maintenance system that allowed us to calculate the turnover rate of flagellar components at 0.5 microns/minute, a previously undetermined parameter. Our results suggest that all flagella on a cell share components out of a common cytoplasmic pool. Furthermore, we show that a model with continuous turnover of components provides the simplest explanation for the flagellar growth and maintenance system. The implication for ciliogenesis is that flagellar growth and maintenance are not separate processes but rather are part of a single length control system. Overall our findings support a general model for dynamic organelle size control.

Introduction:

Cilia, and the structurally homologous flagella, are microtubule-based organelles that project out from the cell body, forming a filamentous appendage that is enclosed by the cell membrane. In humans, many forms of congenital disease result from mutations in the genes that build the cilium and affect its length (Badano, Mitsuma et al. 2006). Therefore, it is important to understand how the length of these organelles is set.

The majority of the work on flagellar length control has been carried out in *Chlamydomonas reinhardtii*, a biflagellate, motile, green alga. In one of the classical experiments on this system, Rosenbaum *et al* (1969) documented the “long-zero” response, whereby amputation of a single flagellum results in shortening of the remaining flagellum. This result was interpreted to mean that the two flagella may be under separate, active, length control programs, whereby the short flagellum is actively induced to grow and the long flagellum is actively induced to shorten (Pan and Snell 2005). This hypothesis is supported by the “overshoot” response, whereby a long-zero cell shortens its long flagellum to a length shorter than that of its short flagellum (Rosenbaum, Moulder et al. 1969), clearly showing that the two flagella must be in distinct operational states at the point where their lengths become equal, since one continues to shorten and one continues to grow after reaching that point. In support of this idea, Baldwin *et al* (Baldwin, Kuchka et al. 1984) reported that in the *vfl2* mutant, which can have more than two basal bodies and flagella, the extra flagella do not shorten in

response to amputation of their neighbors suggesting that the activation of the shortening response requires some physical communication between basal bodies.

The idea that the long-zero response requires activation of distinct growth and shortening activities in the two flagella was challenged by reports that flagella are dynamic structures. It has been well-shown that there is continuous turnover of the structural components of the flagellum at its distal tip (Stephens 1997; Stephens 2000; Marshall and Rosenbaum 2001; Song and Dentler 2001). Thus, rather than being a static structure, the flagellum remains dynamic when it is at fixed length. The steady state length therefore results from the balance between assembly and disassembly processes, such that when the assembly process is shut down, as in the *fla10^{ts}* mutant (Huang, Rifkin et al. 1977), the flagellum begins to shorten. The disassembly process is thought to be passive and length-independent, resulting from remodeling of the structural components, i.e. the axoneme, at the flagellar tip. However, the assembly process depends on the active transport rate of axonemal precursors to the flagellar tip by intraflagellar transport (IFT). The fact that flagella undergo continuous turnover balanced by length-dependent assembly raised an alternative explanation for the long-zero response, whereby the long flagellum shortens not because a special disassembly pathway is activated, but rather because the regrowing, amputated flagellum consumes precursor proteins faster than the normal steady state assembly rate, thus, out-competing the long flagellum for precursor and causing it to shorten (Marshall and Rosenbaum 2001; Marshall, Qin et al. 2005). Computational modeling

showed that a competition between the two flagella for a limited precursor supply, combined with an inherent length dependence of intraflagellar transport, was sufficient to explain the equalization of flagellar lengths in long-zero experiments (Marshall and Rosenbaum 2001; Marshall, Qin et al. 2005). This type of model cannot, however, account for the overshoot that was sometimes reported, because it postulates that the different flagellar behaviors during the long-zero response result from the different lengths, such that if they attain equal lengths their subsequent behavior should be identical.

To distinguish the two possible explanations for the long-zero response, we term the model based on competition for precursor pool the “competition model” and the previous model based on activation of distinct growth and shortening mechanisms in the two flagella the “active control model.”

In order to distinguish between the competition model and the active control model, we repeated the classical long-zero experiments under more controlled conditions, using a custom-designed microfluidic trap combined with laser microsurgery in wildtype, *vfl2*, and *lf4* cells. In agreement with the competition model, we never observed the overshoot response, and we observed shortening of unamputated, long flagella in *vfl2* as well as in wildtype cells with four flagella sharing a common cytoplasm due to incomplete cell division. Based on these results we formulated a mathematical model of the flagellar growth and maintenance system, which gives good agreement with the experimental results reported by others and us. We then used this model to calculate, for the first time,

the disassembly rate of flagella in the presence of active IFT, which is equivalent to the assembly rate at steady state length.

Results and Discussion

Microfluidic trapping keeps motile cells immobile and healthy for many hours

Visualizing the long-zero response requires measurements of flagellar lengths over a period on the order of 1 hour. However, *Chlamydomonas* cells swim at ~100 microns per second and are notoriously difficult to image for long periods of time. Therefore, for long time lapse imaging, previous investigators have used paralyzed strains and trapping devices such as a rotocompressor. Such approaches raise a number of potential concerns including reliance on strains with structurally altered axonemes as well as poor gas exchange and artifacts due to mechanical pressure in cells compressed by a coverslip. To overcome the obstacle of long term imaging, we built a microfluidic trapping system with the CellASIC company that allows simultaneous imaging of up to 100 motile, wildtype *Chlamydomonas* cells in PDMS wells, without compressing the cells and under continuous fluid flow conditions that ensure a constant supply of fresh aerated media (Fig 1). In tests, the cells remained healthy and able to regenerate their flagella for over 18 hours and even underwent cell division in the chamber. This was in contrast to cells trapped under a tightly pressed coverslip, in which both flagellar regeneration and cell division were increasingly impaired over time (data not shown). We imaged cells with a 40x lens that allowed us to track up to 48 cells at a time, though typically closer to 35 cells were trapped. Cells still moved their flagella while trapped in the chamber, but due to the flow the cells could not escape by swimming. Occasional gliding behavior allowed cells to escape from the traps, but >90% of the cells that were trapped at the start of

imaging remained trapped after 10 hours. Divided cells tended to escape more frequently because their smaller size lets them slip past the trap wells.

Laser microsurgery induces cells to sever their flagella at the base

Induction of the long-zero response requires a way to amputate one of the two flagella. Prior studies used finger-pressure tapping on the coverslip to induce the “pop off” of a flagellum at the base, or else fluid shearing with blenders or syringes prior to mounting under the coverslip. Such approaches suffer from a key limitation that the experimenter cannot choose which flagellum will be amputated. As an alternative approach, we used a femtosecond infrared (IR) laser to cut individual flagella on trapped cells. Initial laser severing of the flagellum was followed by immediate detachment of the remaining stump at the base of the flagellum (Fig 2). This detachment behavior resembles that induced during pH shock: the site of severing is near the base of the flagellum. In order to prevent this detachment behavior, we attempted to use the *fa1* mutant, which lacks pH shock deflagellation behavior. Consistent with our earlier observation, *fa1* cells did not detach the injured flagellar stump after laser severing of the distal portion of the flagellum. However, we found that, in contrast to wild-type cells, *fa1* mutant cells treated with laser microsurgery subsequently died before any regeneration of the amputated flagellum or shortening of the long flagellum occurred. This result held true whether the flagellum was severed at the base or at the tip, suggesting that the flagellar detachment program encoded by the *fa* genes has a functional role in recovery from flagellar injury. We attempted flagellar amputation on several other mutant and wildtype strains (*lf4*, *lf1*, *lf2-1*, *lf2-5*, *lf3*,

asq2, vfl1, vfl2, vfl3, ptx2, ptx8, eye2, eye3, pf16, pf18, KAP-GFP rescue of fla3-1, wt CC124, wt CC125, wt CC1009), all of which detached injured flagella at the flagellar base in a similar manner.

Overshoot behavior does not occur

One of the intriguing findings of the original long-zero papers was that while most cells with an amputated flagellum would directly equilibrate the lengths of the regenerating and uninjured flagella at roughly 2/3 full length, some fraction of the cells with an amputated flagellum would shorten their uninjured flagellum to a length significantly shorter than the regenerating flagellum, “overshooting” the length before recovering. One possible interpretation of this behavior was that an active shortening program had been initiated in the long flagellum that, if not stopped in time, would cause the long flagellum to overshoot the length of the regenerating flagellum. The overshoot phenomenon is the strongest piece of evidence in favor of the active control model compared to the competition model, since the latter model cannot explain overshoot at all. We examined 100 cells by our methods and never saw the overshoot behavior, indicating at $p < 0.00002$ (Binomial statistic), that the overshoot behavior does not occur in microfluidically trapped cells, and may therefore have been an experimental artifact. Because the single amputations performed by Rosenbaum *et al* (1969) involved crushing the cell bodies until the flagellum popped off, there exists the possibility that some other damage was done to the long flagellum or the cytoplasm in the overshoot circumstances. Because our alternate methodology induces deflagellation from the flagellar side of the cytoplasm, it is possible that we do not cause such damage

to the unamputated flagellum. By this logic, we believe our method to be less prone to artifacts. Using our method we saw typical long-zero response in all 100 cells (Fig 3). Because we do not observe the overshoot behavior in our experimental setup, our results favor the competition model.

vfl2 and asq2 cells shorten uninjured flagella in response to amputation of flagella that grow from a separate base

Another piece of evidence in support of the active shortening hypothesis was the lack of long-zero behavior of *vfl3* cells (Baldwin, Kuchka et al. 1984). While wildtype cells have two flagella that are joined by connective fibers at the basal bodies, the *vfl* and *asq* mutants can have up to six flagella that emanate from separate bases. Baldwin *et al* (1984) reported that flagella emanating from disconnected bases do not undergo the long-zero response; rather, the uninjured flagella maintain their length while the amputated flagellum regrows. This supported the idea of an active shortening system where flagella emanating from a common base are induced to shorten when their mate is damaged. In contrast, according to the competition model, the flagella should all be competing for the same cytoplasmic precursor pool regardless of how their associated basal bodies happen to be arranged. Hence, the loss of long-zero response in *vfl3* mutants is more consistent with active control than with the competition model. We therefore repeated the analysis of long-zero response in *asq2* (a.k.a. *vfl3*) and *vfl2* mutants. In contrast to the results reported by Baldwin *et al* (1984), we observed that flagella emanating from separate bases undergo long-zero kinetics, although

sometimes with a longer lag time in the response of disconnected flagellar bases (N=20 *asq2* cells and N=15 *vfl2* cells). This result supports the competition hypothesis, whereby shortening is induced by a drop in the cytoplasmic pool of precursor material required for flagellar maintenance. We also observe the same results when we performed the long-zero experiment in wild-type cells that had failed to complete cytokinesis, such that the cells had two pairs of flagella emanating from a common cytoplasmic pool. In dynamics mimicking the long-zero response, the long pair of flagella shortened in response to amputation of the sister pair (Fig. 4). This result supports the competition model because long flagella shorten in response to amputation of other flagella sharing the same cytoplasmic pool of material.

A mathematical model of the flagellar growth and maintenance system accurately fits the observed dynamics

A key difference between the active shortening and competition models is that while the active shortening model explains flagellar growth and flagellar maintenance states separately, the competition hypothesis must explain both states with a single consistent mechanism. We therefore formulated a mathematical model of the flagellar growth and maintenance system in order to test it. We used the basic assumptions from Marshall and Rosenbaum (2001; 2005) but modified their model in order to use known IFT rates (see Chapter 2, Fig. 3) and a dynamic cytoplasmic pool (Appendix 1). We then tested the model response to pH shock and long-zero perturbation. The model accurately accounts for all of the experimentally observed dynamics (Fig 5), thus indicating that one does not need

to invoke special distinct states in order to explain the long-zero response. We therefore suggest that this simple model explains flagellar growth and maintenance more parsimoniously than the active length control model.

The flagellar growth and maintenance model determines the disassembly rate to be ~0.5 microns/second

A key parameter in the previously proposed "balance point" model for length control was the rate of axonemal disassembly at steady-state. Previously, this parameter was estimated from the shortening rate of flagella following the inactivation of IFT using the *fla10* conditional mutant shifted to the non-permissive temperature (Marshall and Rosenbaum 2001). However, there is prior evidence that retrograde IFT may play a role in flagellar disassembly (Pan and Snell 2005). Hence, we expect that the prior estimate of disassembly rate based on shortening in *fla10* mutants is probably a gross under-estimate.

Because the mathematical model for two flagella gives two equations and two unknowns, we solved for the parameters and plugged in the time course regeneration data for the long-zero response to determine the disassembly rate (Appendix 2). This yielded a disassembly rate of 0.50 microns/second (Fig. 6), which is substantially greater than the estimate based on shortening in *fla10* (Marshall and Rosenbaum 2001) and slightly greater than the maximum shortening rate of 0.45 microns/second observed in live cells during the long-zero response and prior to cell division (Rosenbaum, Moulder et al. 1969; Parker 2008). Comparing the *fla10*^{ts} data and the shortening prior to cell division data,

the disassembly rate appears to be much higher when IFT is active than when IFT is shut down. We hypothesize that in the absence of IFT the breakdown products cannot be transported away from the assembly site at the flagellar tip and could, therefore, be free to reincorporate into the flagellum. Thus the slow disassembly rate observed in *fla10^{ts}* may be due to diffusion of disassembly products out of the flagellum. Incorporating a photoactivatable fluorophore into the axoneme could test such a hypothesis.

Implications for size control of dynamic organelles

All cells face the problem of organelle size control. In order to operate with optimal metabolism and behavior, the size of the organelles must be modulated to meet the instantaneous environmental conditions that a cell is experiencing. Our results provide a simple model for dynamic organelle size control that could be extended to many other organelles (e.g. mitochondria, endoplasmic reticulum, nucleus, vacuole, etc). In this model, dynamic, self-assembling organelles are controlled through the available pool of organelle precursor in the cytoplasm. The organelles thus operate semi-autonomously through self-assembly, but ultimate control over their size remains with control over precursor availability.

Materials and methods

Strains and cell culture

All strains were acquired from the *Chlamydomonas* stock center (University of Minnesota) except *asq2*, which was made by Jessica Feldman and available in the Marshall lab, and the KAP-GFP rescue of *fla3*, which was a generous gift of Mary Porter.

Cells were grown in either standard TAP or M1 liquid media (see *Chlamydomonas* Sourcebook).

Microscopy:

Light microscopy was performed on a Zeiss Axiovert 200 using the custom configuration shown in Figure 2. Imaging was performed using a 40x NA 1.4 lens and Phase contrast 3 filters and a Hamamatsu CCD camera with 6 pixels per micron. Measurement of flagella was performed by hand-tracing in ImageJ64.

Microfluidics:

CELLASIC microfluidics were operated per manufacturer instructions.

Analysis and mathematical modeling:

All analysis and mathematical modeling was carried out using custom software in MATLAB

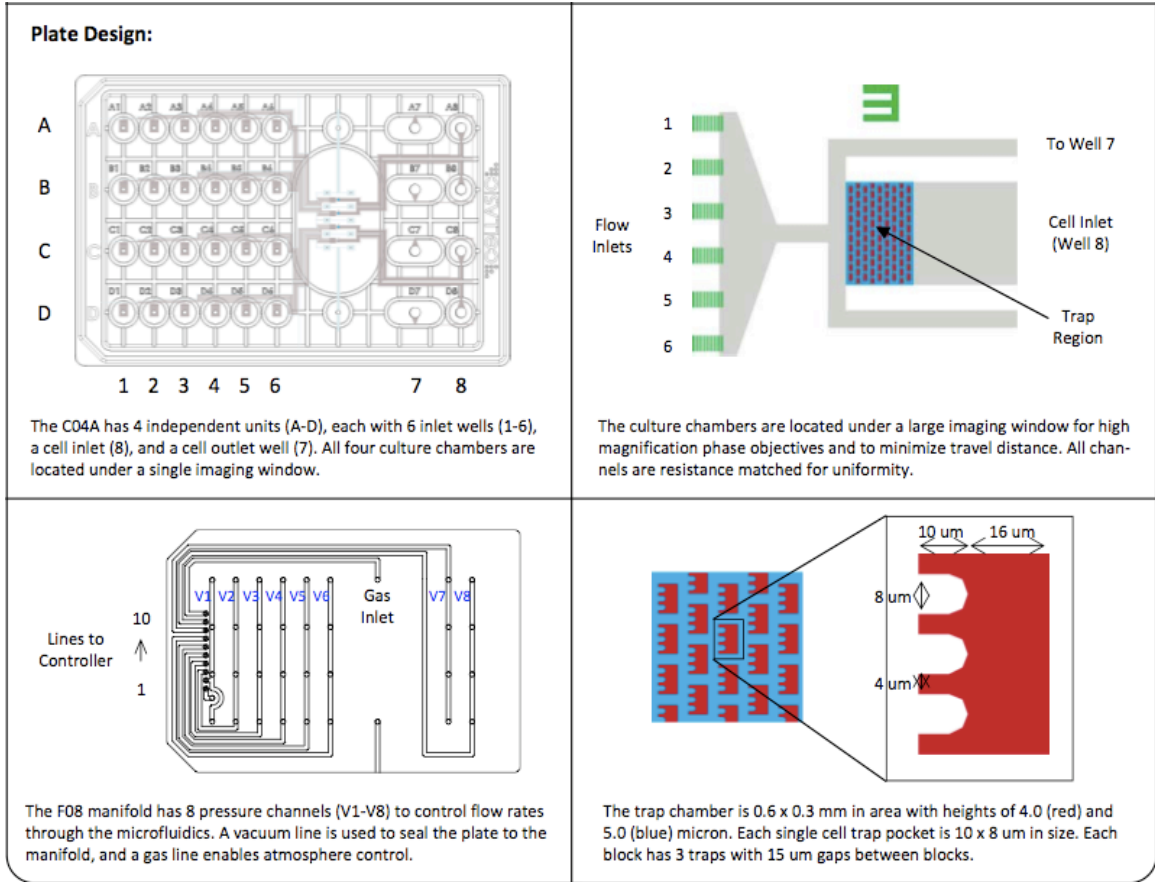
References

- Badano, J. L., N. Mitsuma, et al. (2006). "The ciliopathies: an emerging class of human genetic disorders." Annu Rev Genomics Hum Genet **7**: 125-148.
- Baldwin, D. A., M. R. Kuchka, et al., Eds. (1984). Approaches to flagellar assembly and size control using stumpy- and short-flagella mutants of Chlamydomonas reinhardtii. Molecular biology of the cytoskeleton. Cold Spring Harbor, New York, Cold Spring Harbor Laboratory.
- Huang, B., M. R. Rifkin, et al. (1977). "Temperature-sensitive mutations affecting flagellar assembly and function in Chlamydomonas reinhardtii." J Cell Biol **72**(1): 67-85.
- Marshall, W. and J. Rosenbaum (2001). "Intraflagellar transport balances continuous turnover of outer doublet microtubules: implications for flagellar length control." Journal of Cell Biology **155**: 405-414.
- Marshall, W. F., H. Qin, et al. (2005). "Flagellar length control system: testing a simple model based on intraflagellar transport and turnover." Mol Biol Cell **16**(1): 270-278.

- Pan, J. and W. J. Snell (2005). "Chlamydomonas shortens its flagella by activating axonemal disassembly, stimulating IFT particle trafficking, and blocking anterograde cargo loading." Developmental Cell **9**(3): 431-438.
- Parker, J. (2008). "Co-ordinate regulation of cilia and the cell cycle in Chlamydomonas reinhardtii." summit.sfu.ca.
- Rosenbaum, J. L., J. E. Moulder, et al. (1969). "Flagellar elongation and shortening in Chlamydomonas. The use of cycloheximide and colchicine to study the synthesis and assembly of flagellar proteins." J Cell Biol **41**(2): 600-619.
- Song, L. and W. L. Dentler (2001). "Flagellar protein dynamics in Chlamydomonas." J Biol Chem **276**(32): 29754-29763.
- Stephens, R. E. (1997). "Synthesis and turnover of embryonic sea urchin ciliary proteins during selective inhibition of tubulin synthesis and assembly." Mol Biol Cell **8**(11): 2187-2198.
- Stephens, R. E. (2000). "Preferential incorporation of tubulin into the junctional region of ciliary outer doublet microtubules: a model for treadmilling by lattice dislocation." Cell Motil Cytoskeleton **47**(2): 130-140.

Figures

Figure 1a:



Design of the CellASIC CHLAMY plate ©CellASIC

Figure 1b: CellASIC CHLAMY chamber empty (top) and with cells loaded (bottom). Cell diameter is about 5 microns.

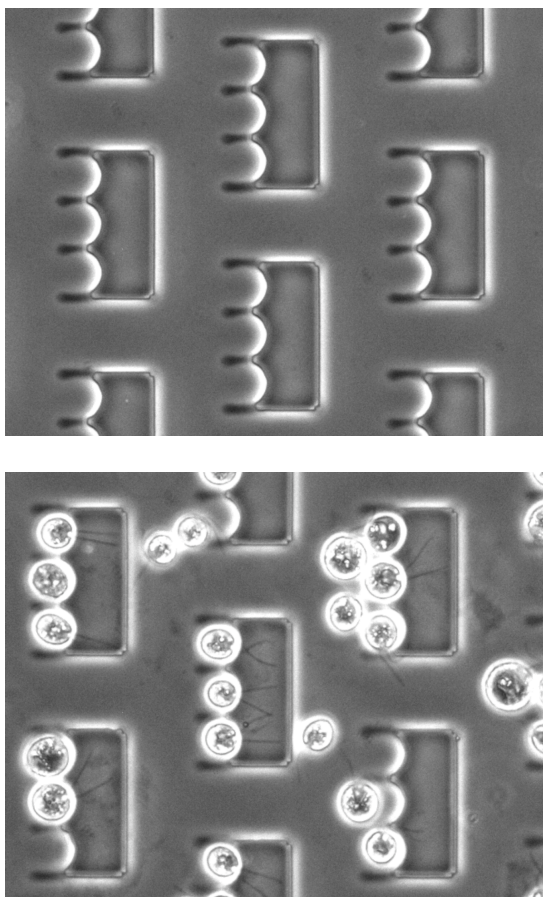
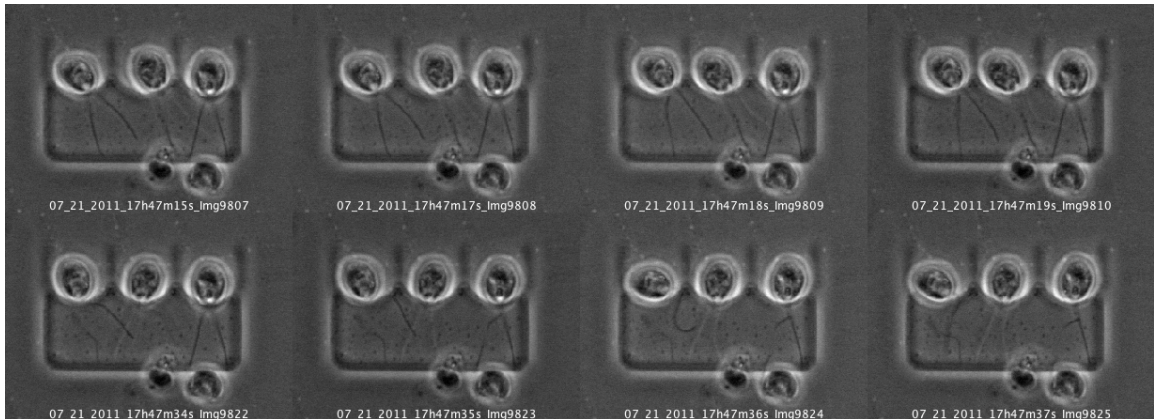
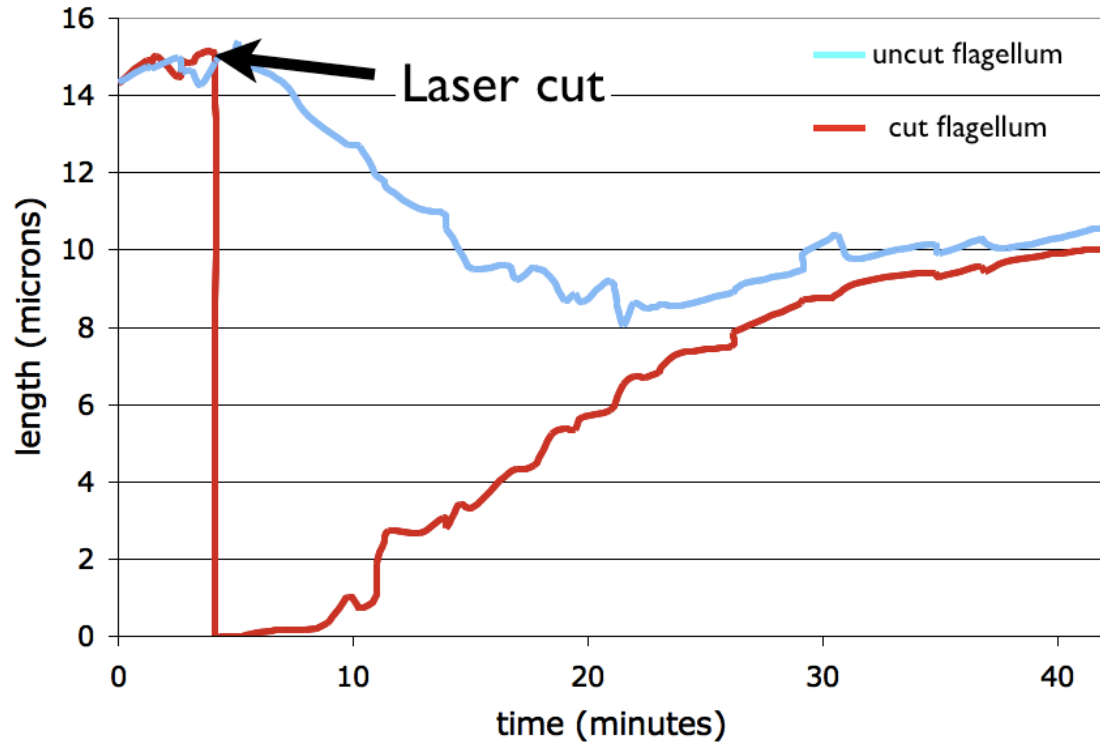


Figure 2: laser severing induces “pop off”



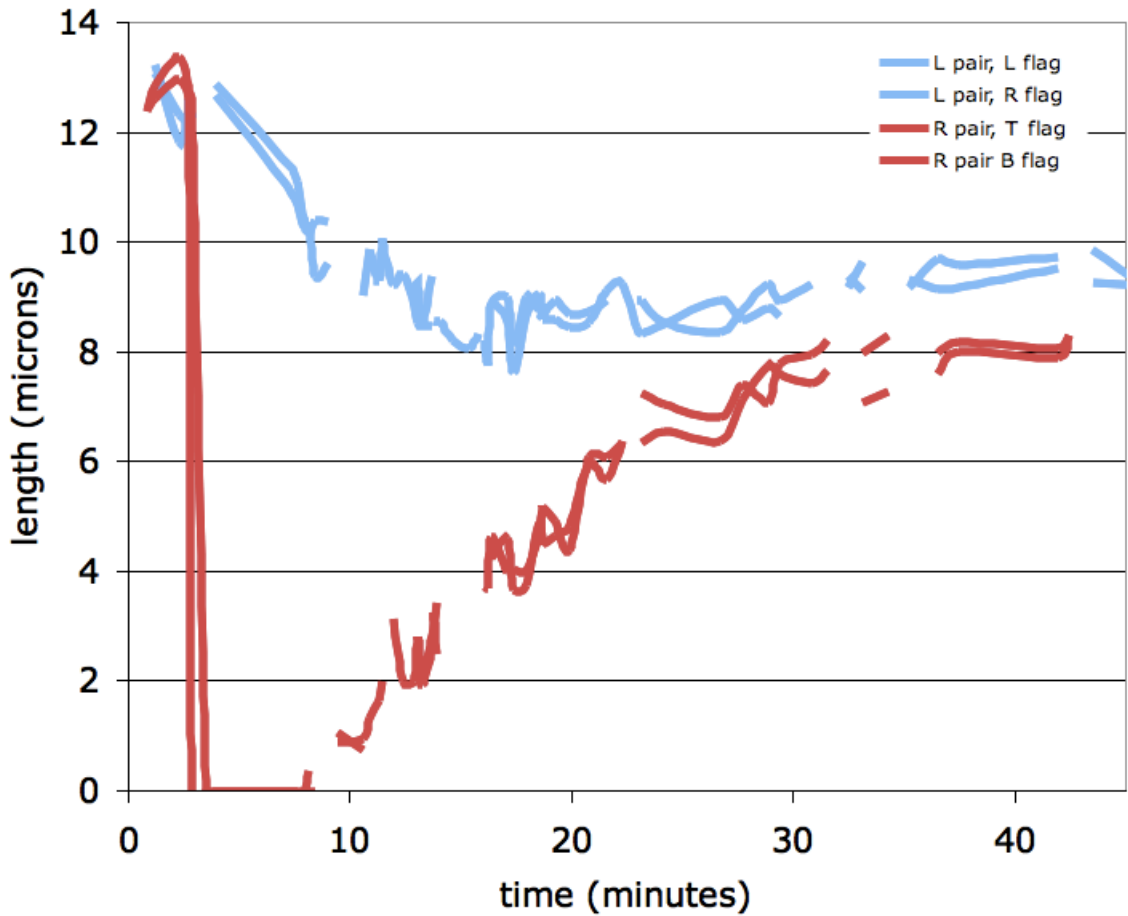
An image montage during laser ablation. In Img9809, the left-most cell’s left flagellum is hit. The disconnected flagellum is evident later in Img9824. In Img9823, the right-most cell’s left flagellum is severed. “Pop off is noticeable immediately. The middle cell is used as a control for flagellar length changes during regeneration.

Figure 3: the long-zero response as observed in a typical wildtype cell



In typical long-zero regeneration kinetics, the uncut flagellum shortens as the regenerating flagellum lengthens.

Figure 4: the long-zero response in cells with unconnected basal bodies follows the same pattern as in cells with connected basal bodies.



In a wildtype CC125 cell with two pairs of flagella due to incomplete cell division, the right (R) pair of flagella was amputated. The left (L) pair was left alone. Shortening of the left pair of flagella is obvious as is regeneration of the top (T) and bottom (B) flagella from the right pair.

Figure 5: model predictions for regeneration kinetics after long-zero perturbation

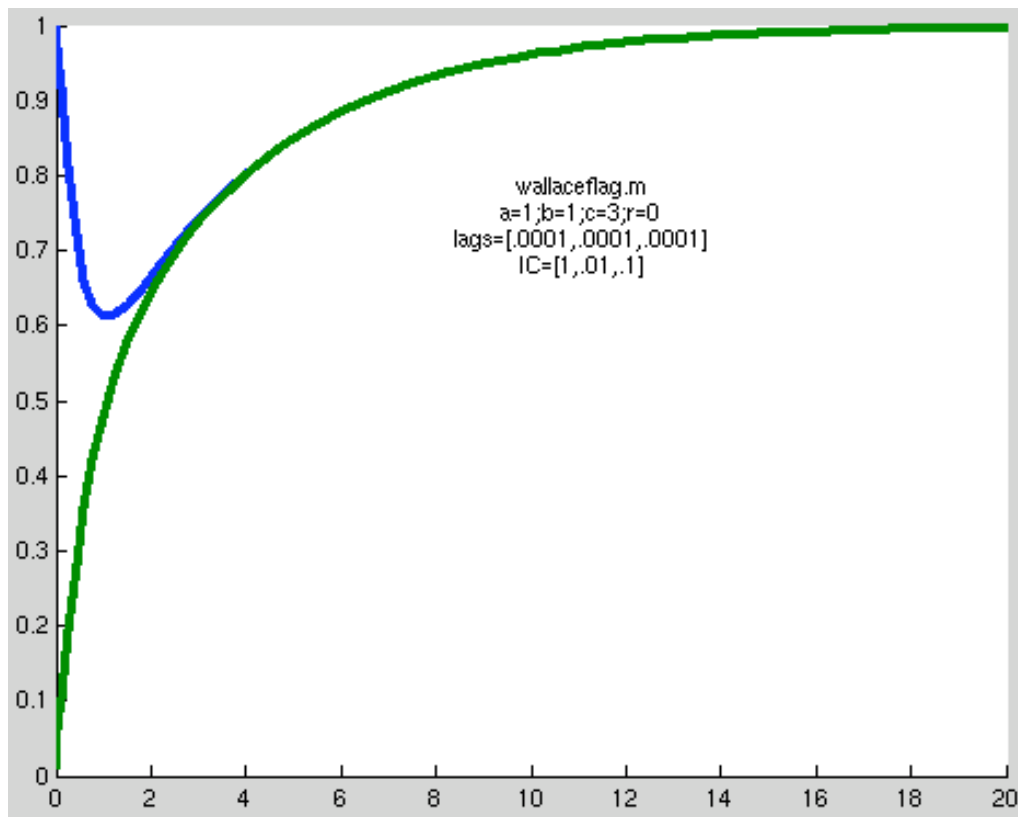
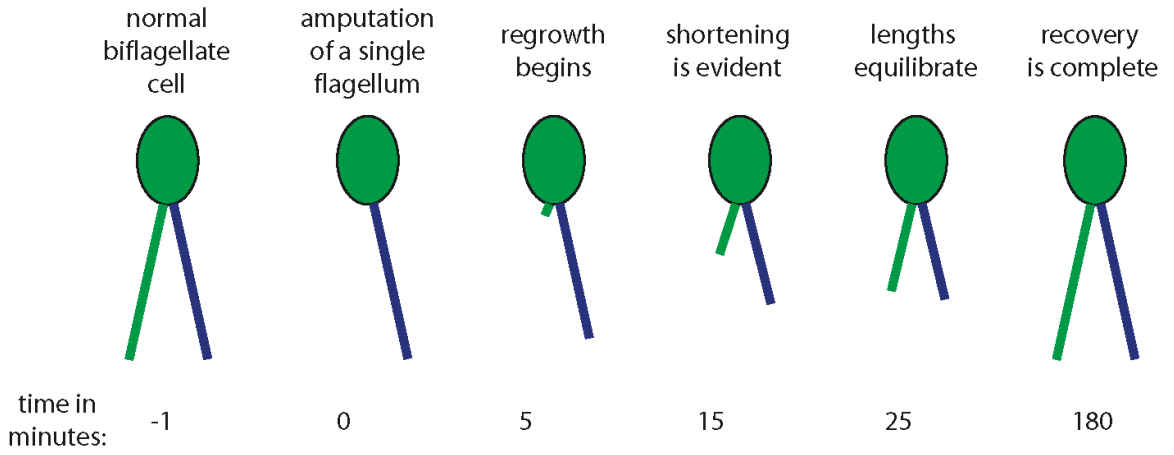
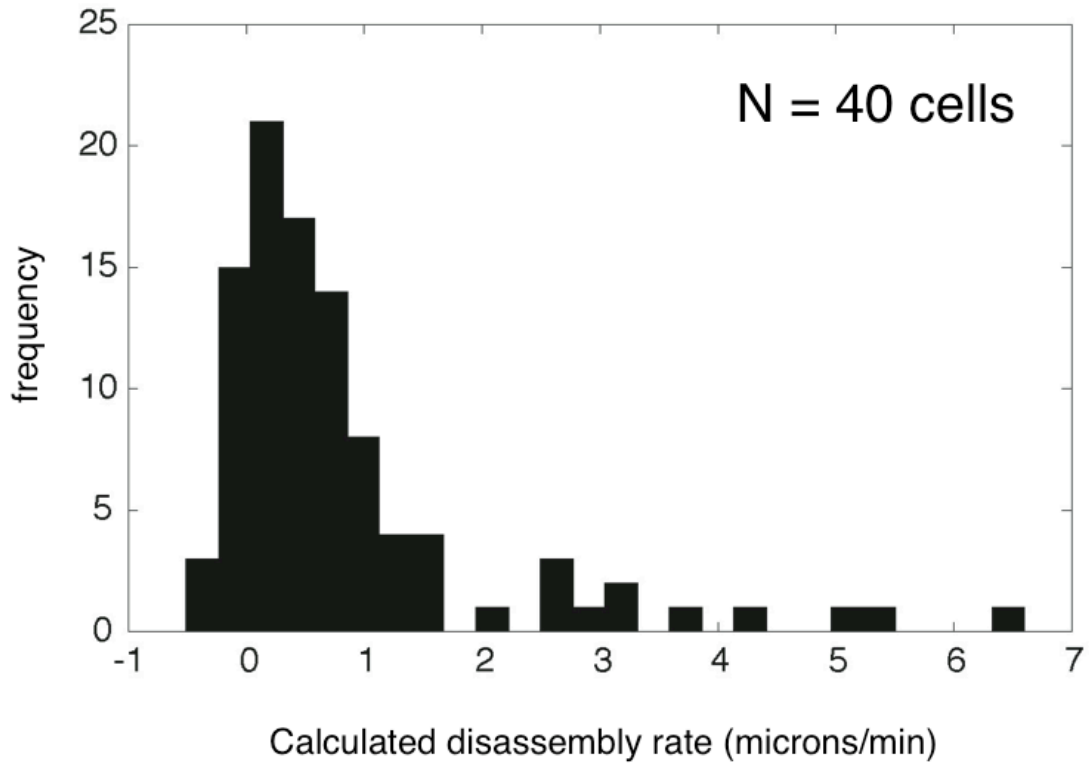


Figure 6: histogram of the calculated disassembly rate. The disassembly rate was calculated for all pairs of time points possible according to the scheme set up in Appendix 2. Though there is a lot of measurement noise, which leads to a large spread in the calculation, the median calculated rate is 0.50 microns per minute.



Appendix 1: model of flagellar length control

$$\frac{dL_1}{dt} = k_1 C_t IFT(L_{1t}) - k_2$$

$$\frac{dL_2}{dt} = k_1 C_t IFT(L_{2t}) - k_2$$

$$\frac{dC}{dt} = 2k_2 - k_1 C_t (IFT(L_{1t}) + IFT(L_{2t})) + k_3(1 - C_t)$$

Variables and parameters:

L = length

k_1 = assembly constant

C_t = cytoplasmic pool

IFT(L) = transport rate

k_2 = disassembly constant

k_3 = cytoplasmic pool constant

Length change, $\frac{dL}{dt}$, is due to IFT-dependent growth, $k_1 * C_t * IFT(L)$, and to

length-independent disassembly, k_2 . The cytoplasmic pool changes size based on

flagellar growth and flagellar disassembly as well as protein synthesis and decay.

Appendix 2: scheme for calculating the disassembly rate. measured quantities are marked in red and the two unknowns are circled in green in each equation.

$$\frac{dL_1}{dt} = k_1 C_t IFT(L_{1t}) - k_2$$

$$\frac{dL_2}{dt} = k_1 C_t IFT(L_{2t}) - k_2$$

Variables and parameters:

L = length
k ₁ = assembly constant
C _t = cytoplasmic pool
IFT(L) = transport rate
k ₂ = disassembly constant
k ₃ = cytoplasmic pool constant

Chapter 6

How a cell can measure length and volume

Synopsis:

I approach the subject of ciliary length control from a theory angle, deriving quantitative versions of popular models and proposing two of my own. I then compare best fits of the models to experimental data using a model selection with the Akaike Information Criterion (Akaike, 1974). The model with the best fit to the available data is one based on a diffusion gradient between the organelle and the cytoplasmic compartment. From a practical standpoint, the model is attractive because it fits well with previous models of nuclear import control and a GTPase gradient as well as with a prominent report (Dishinger et al., 2010) on ciliary import control. The model is attractive from a theoretical standpoint because it can be generalized to allow the cell to measure organelle volume as well as length.

Introduction:

Cells are bags of matter that somehow perform elaborate feats of organization (Bak, 1996). For example, the many organelles in a cell are maintained in precise size, shape, and position to maximize cellular function. We study the problem of size control in the *Chlamydomonas reinhardtii* flagellum, a proven model system for mammalian cilia.

The problem of size control is particularly perplexing for a cell because an absolute measurement must be established without a standard ruler. Ask a person how tall they are, and they will answer in calibrated units (metric or imperial). But a cell must make a ruler from scratch. Several examples of these rulers have been described, including a molecular ruler system in bacteriophage tails and muscle thin-filament actin and a measuring cup for bacterial flagellar hook growth (Marshall, 2004). However, none of these systems represents a standard system of measurement that could easily apply generally. In the eukaryotic cilium, the measurement problem has not been answered, although it is a much-studied system; therefore, we hope that by studying another example of size control we will gain new perspective on the problem.

In this chapter I develop quantitative versions of popular theories for a ciliary length ruler and compare the predictions of these theories with intraflagellar transport (IFT) particle injection data as well as fluorescence recovery after photobleaching (FRAP) data. The models I will discuss are (1) constant IFT (Marshall and Rosenbaum, 2001; Marshall et al., 2005), (2) time of flight (Lefebvre, 2009), (3) membrane channels (Beck and Uhl, 1994; Johnson and

Rosenbaum, 1993; Pazour et al., 2000; Rosenbaum, 2003), (4) linear diffusion (presented here), (5) volumetric diffusion (presented here), as well as (6) constant IFT injection rate, and (7) ideal swimming speed feedback (Marshall *pers. comm.*). See Tables 1 and 2 for a summary.

The constant IFT model was proposed by Marshall and Rosenbaum (2001) as part of their “balance point” model. It postulates that the flagellar length is set by an interplay between a constant disassembly rate and a length-dependent growth rate. The flagellar length is set by the balance point where the growth rate exactly cancels out the disassembly rate. A corollary of the balance point model was that the amount of intraflagellar transport (i.e. the rate of transport) sets the growth rate. Marshall and Rosenbaum supported this corollary with evidence that the total amount of IFT particles remains approximately constant as a function of flagellar length. Therefore they reasoned that the amount of transport is actually much higher in short flagella, where the set amount of IFT particles is spread out over a much shorter distance. This model goes a long way in explaining how length is controlled and makes a very important observation that the amount of IFT particles is roughly constant as a function of flagellar length, however, it creates the new problem of how the amount of IFT particles is kept constant. Chapter 2 shows that the accumulation of IFT particles appears to be regulated, but again, this still leaves open the question of how. Thus, the cell’s measuring mechanism has yet to be defined. One possibility proposed by Marshall *et al* is the initial bolus model, where a precisely measured initial bolus of flagellar precursor material is set aside to build a flagellum, and no additional material is

provided. Though an initial bolus model can build many flagella at a precise length, data in *Chlamydomonas* do not support the model because there is turnover of material in the flagellum, and it can change length over time.

The time of flight model makes a beautiful and internally consistent theoretical ruler. It proposes that length is measured by sending a signal molecule in the excited state (e.g a GTPase) on IFT particles entering the flagellum. The longer the flagellum, the longer the signal molecule spends in the flagellum, and the higher likelihood that the signal molecule reverts to the ground state before exiting the flagellum. The length of the flagellum can then be determined by the ratio of excited to ground state signal molecules exiting the flagellum. Several candidate signal molecules exist in the flagellum, yet none of them show an appropriate pattern of phosphorylation for the model to be proven.

The membrane channels model comes from work in mammalian kidney cells. As a cilium lengthens, it is more apt to be bent by fluid flows. In mammalian cells, this bending by fluid flow has been shown to induce ciliary shortening through a Ca^{++} signal setting off a MAP kinase cascade (Besschetnova et al., 2010), set off by a ciliary membrane mechano-sensitive channel (Abdul-Majeed and Nauli, 2011). Rosenbaum (1993; 2003) proposed that mechano-sensitive membrane channels could represent a general model for ciliary length control. Some evidence has been found for this behavior in *Chlamydomonas* (Beck and Uhl, 1994), but it is not widely accepted as a general length control model. Rather, Ca^{++} seems to be one factor that can perturb ciliary length. However, a

quantitative model that could use membrane channels to sense length is formulated here (see Results).

The linear diffusion and volume diffusion models are presented here for the first time. Both models are based on a diffusion gradient of a signal produced in the flagellum and consumed in the cytoplasm. The magnitude of the gradient between the flagellar and cytoplasmic compartments tells the flagellar length. In the linear diffusion model, a signal is produced at a constant rate at the flagellar tip. That signal is sensed on the flagellar side of the flagellum:cytoplasm junction. When the flagellum is short, the signal is high, and when the flagellum is long, the signal is low. The linear diffusion model relies on a stable shape of the gradient being maintained, which may be an unreliable assumption.

The volume diffusion model shares some of these ideas but also borrows concepts from the nuclear import Ran-GTP gradient concept. It measures volume of the cytoplasmic compartment rather than length specifically. The volume diffusion specifies that a signal is produced in the flagellar compartment. That signal is degraded while in the flagellum, so that a longer flagellum degrades more signal. The length is sensed as the concentration in the flagellar compartment, therefore there is no requirement for a shape of the gradient.

The constant injection rate model states that the injection rate is constant as a function of flagellar length. It runs into trouble empirically because this has been shown not to be the case (Engel et al., 2009) as well as theoretically because it would lead to unstable length.

The ideal swimming speed feedback model says that *Chlamydomonas* changes flagellar length to match with the ideal length for swimming in its environment. Regardless of how the cell senses its swimming speed, this model predicts that length should change in response to a change in media viscosity. I present findings by a summer student, Jay Serebrenick, that show this not to be the case. In the results section I present quantitative derivations of the constant total IFT, time of flight, membrane channels, diffusion, and constant IFT injection rate models and then compare their predictions with IFT particle injection rate data. I also present some preliminary FRAP data, which prove that there is turnover of IFT particles in the flagella. And I present Jay Serebrenick's data, which show that *Chlamydomonas* flagella do not change length in response to viscosity change of their media, unless they are subjected to fluid flow while not swimming (i.e. in the CellASIC chamber).

Results:

First, I present the derivations of the models, then discuss their fit to the data and the implications.

Constant IFT model derivation according to Marshall and Rosenbaum (2001; 2005):

The cell allocates a fixed or constant amount of IFT machinery to each flagellum as an initial bolus.

Assumptions:

1. each flagellum has a constant amount of IFT machinery, independent of length, so that the total number of IFT proteins, \mathbf{N} remains fixed.
2. the injection rate is proportional to the amount of IFT machinery at the base.

Take a short, fixed length, \mathbf{m} , of the flagellum. The amount of IFT machinery in this segment of the flagellum is $\frac{mN}{L}$, which is then proportional to the injection rate. So the injection rate is

$$S(L) \propto \frac{k}{L}.$$

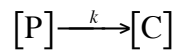
The total IFT as a function of flagellar length is defined as constant, N , based on the assumption that the cell allocates a fixed pool of IFT machinery to each flagellum and there is no turnover with the cytoplasm.

Time of flight model derivation:

Time of flight model for injection signal, where injection rate is proportional to signal.

Assumptions:

1. precursor, P, is injected into flagellum
2. P is converted to C at a constant rate while in the flagellum
3. time in flagellum is proportional to flagellar length
4. Signal is sensed at ejection.
5. remaining P decreases signal
6. C increases signal



therefore,

$$\frac{dP}{dt} = -k[P], \text{ so } \ln(P) = -kt + D_0, \text{ or}$$

$$P(t) = De^{kt}.$$

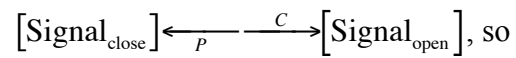
Because we assume that 't' is proportional to flagellar length, 'L', we have

$P(L) = De^{kL}$. And assume steady state for a given length.

The converted precursor, 'C' is just $P_0 - P(L)$, so

$$C(L) = P_0 - De^{kL}.$$

The signal is measured as



$$\frac{d[\text{Signal}_{\text{open}}]}{dt} = C[\text{Signal}_{\text{close}}] - P[\text{Signal}_{\text{open}}], \text{ and}$$

$S_{eq} = \frac{P}{C}$, which is equivalent to

$$S_{eq} = \frac{De^{kL}}{P_0 - De^{kL}}.$$

The total IFT is just the residence time multiplied by the signal, or

$$IFT_{ToF} = L \cdot \frac{De^{kL}}{P_0 - De^{kL}}.$$

Membrane channel model:

Ion channels in the flagellum produce a current through the flagellar pore that informs the pore of the flagellar length.

Assumptions:

1. voltage-dependent calcium channels occur at constant density on the flagellar surface, independent of flagellar length, L , and act as resistors to current flow across the flagellar membrane
2. the flagellum and the cell body are not at equilibrium with one another
3. ion pumps on the cell body maintain a voltage, V_{cell}
4. current passes through the flagellar pore
5. all the flagellar channels have the same resistance and the probability of the channels being open is fixed, independent of the number of channels
6. $V_{cell} = IR_f$, we assume that the product of the current, I , and the flagellar resistance, R_f , equals the voltage across the flagellar membrane.
7. The flagellar resistance can be attributed to the open channels

Flagellar resistance is calculated from $\frac{1}{R_{flagellum}} = \sum_{i=1}^n \frac{1}{R_i}$, or $\frac{n}{R_i}$, where n is the

number of open channels on the flagellum. n is proportional to the flagellar length

because we assume a constant channel density and a constant likelihood of being open. Therefore, $I_{pore} = \frac{nV_{cell}}{R_i}$. Because V_{cell} and R_i are constants and n is proportional to the flagellar length,

$$I_{pore} \propto L.$$

If we assume that the current is directly proportional to the negative of the injection signal, then

$$S = k_1 - k_2L$$

and

$$IFT_{total} = k_1L - k_2L^2 + k_3.$$

However, the model established by Rosenbaum (2003) does not specify that the current directly signals the IFT injector but rather that the current could modify a biochemical pathway that instead regulates the IFT injector. Therefore, the expressions given for signal and total IFT in this paper are not the only possible behaviors of this model.

Linear diffusion gradient model:

Model for IFT content in a flagellum as a function of length with the following assumptions:

- (1) the flagellar tip produces of a diffusible factor that regulates flagellar pore opening
- (2) the cytoplasm is a sink with constant concentration, $C_{cytoplasm}$
- (3) the basal body sits a distance, b towards the tip from the cytoplasm
- (4) normal diffusion occurs
- (5) the system reaches steady state much faster than the length changes
(Levy, 1974)

Note that this is a similar scenario to that proposed by Levy (1974) before IFT was known to exist. The primary differences are first, that here it is assumed that the diffusible substance originates at the tip rather than at the base and second that the diffusible substance is a regulator of IFT injection into the flagellum rather than some material that directly regulates the assembly of the flagellum, such as a structural component. Levy proposed solely that such a factor required for assembly diffuses from the cytoplasm and is consumed at the flagellar tip.

$$\frac{\partial C}{\partial t} = D \cdot \nabla^2 C$$

set this = 0 because we are looking at a steady-state

then integrate twice with respect to t and solve for $C(L)$:

$$C(L) = \frac{A_1}{D}L + \frac{A_2}{D}.$$

We use the boundary conditions,

$$C(0) = C_{tip} \text{ and } C(X_L) = C_{cytoplasm}.$$

Thus,

$$C(L) = C_{tip} - \frac{C_{tip} - C_{cytoplasm}}{X_L}L$$

The function gives the concentration anywhere along the length of the flagellum, a length L from the tip. The basal body is the primary area of interest, so set $L = X_L - b$, then:

$$C(X_L - b) = C_{tip} - \frac{C_{tip} - C_{cytoplasm}}{X_L}(X_L - b)$$

Simplifying, the concentration at the basal body as a function of flagellar length is:

$$C(X_L)_b = C_{cytoplasm} + b \frac{C_{tip} - C_{cytoplasm}}{X_L}.$$

If it is assumed that the concentration of the diffusible substance regulates the injection rate, and that the injection rate is equal to the ejection rate at steady state, then the total IFT content in a flagellum is just the sum of the constant injection rate times the residence time of an injection in the flagellum:

$$\int_0^{X_L} C(X_L)_b dL = C(X_L)_b \cdot X_L + IFT_0,$$

and L is set equal to X_L , so the total IFT per flagellum is:

$$IFT(X_L) = X_L \cdot C_{cytoplasm} + b \cdot (C_{tip} - C_{cytoplasm}) + IFT_0.$$

Volumetric diffusion model derivation:

This model makes the following basic assumptions:

- (1) signal is produced at a constant rate k_1 in the flagellar compartment
- (2) signal dissipates out of the flagellum at a rate proportional to the concentration difference between the flagellum and the cell body ($k_2*[S]$)
- (3) signal degrades in the flagellar compartment at a constant rate, so that the longer time the signal molecule spends in the flagellar compartment, the more likely it goes to the degraded state ($k_3*L^2*[S]$)

$$\frac{d[S]}{dt} = k_1 - k_2[S] - k_3L^2[S]$$

we normalize by the constant k_3 , making new k_1 and k_2

$$\frac{d[S]}{dt} = k_1 - k_2[S] - L^2[S]$$

$$[S] = \frac{e^{-(k_2+L)} - k_1}{-k_2 - L^2}$$

we assume that the signal stabilizes faster than the length changes, so

$$\lim_{t \rightarrow \infty} [S] = \frac{k_1}{k_2 + L^2},$$

giving us the theoretical injection [or accumulation] rate

$$\lim_{t \rightarrow \infty} [S] = \frac{k_1}{k_2 + L}.$$

After deriving each of the models, I compared them to the IFT injection rates as a function of flagellar length. First, I found the best fit to the data using the NLINFIT function in MATLAB. Then I took a model selection approach, using the Akaike Information Criterion (AIC) (Akaike, 1974) to determine which model gives the best fit to the data (Figure 1). The diffusion models clearly give the best fit to the data according to the AIC, but constant total IFT and time of flight still look like decent fits by eye. Clearly the constant IFT injection rate model can be ruled out by this assay of fit.

As mentioned earlier, the constant total IFT model does not specify how the amount of IFT particles is maintained at a constant level, but one possible way would be to recycle them, by allocating specific particles to one flagellum. If recycling occurs, then photobleaching IFT proteins should permanently bleach the flagellum. Therefore, we tested the recycling hypothesis using FRAP. Flagellar fluorescence made a complete recovery after ~1 minute (Figure 2). Similar results were shown by Huang *et al* (Huang et al., 2007) for the PKD2 protein. Therefore, recycling likely is not a primary mechanism of maintaining a constant amount of IFT proteins in a flagellum. Alternately an initial bolus during flagellar initiation could provide a constant amount of IFT, but again, the FRAP data shows that turnover occurs, so the initial bolus model is not supported in *Chlamydomonas*. However, studies in trypanosomes have shown extremely low or no turnover of IFT proteins, so this mechanism still holds promise in those organisms and cannot be ruled out as a general mechanism.

The time of flight model is elegant and appealing. Even though it does not make the best fit to the data, it still makes a good one and is worth considering further. Therefore we calculated what the predicted amount of total IFT protein would be in the flagellum under the time of flight model. As seen in Figure 3, the time of flight model does a poor job of predicting the total flagellar IFT protein, which has been shown by a variety of methods to remain roughly constant as a function of flagellar length. Though these data should not be the sole test of this attractive model, they do present an obstacle to proving it.

The swimming speed model has no mathematical form at present, but it does make the prediction that changes in the fluid properties of the media should change the flagellar length. Specifically, increasing the media viscosity should significantly shorten the ideal flagellar length. In order to test this hypothesis, Jay Serebrenick grew wildtype CC125 cells side by side in 1 centiPoises (normal) and 2 centiPoises TAP media for 24 hours. The cells maintained the same mean flagellar length (Student's t-test, $p < 0.97$, $N = 50$ each treatment), indicating that cells do not modulate their flagellar length in response to higher viscosity media.

With respect to the flagellar current model, good evidence has been found that the flagellar current amplitude correlates with flagellar length (Beck and Uhl, 1994). If the current serves to inhibit the growth rate, as modeled here, then this provides a plausible model for flagellar length control. However, after Beck and Uhl's (1994) paper, there was never a follow up report showing that perturbing the flagellar current could affect flagellar length. Even a negative result would be informative.

Both the diffusion models have a similar form and a good fit to the data.

However, there are some practical problems with the linear diffusion model. The maintenance of a real linear gradient in a moving flagellum may be implausible. The model also predicts that the injection rate goes to infinity approaching zero length. In addition to being implausible, this approach to infinity makes the model sensitive to small movements of the gradient at low flagellar length. Averaged over time, these factors may not matter, but the simplicity of the volume diffusion model is appealing.

The volume diffusion model has a tidy mathematical form, with no infinite limits or other unrealistic terms. In cellular terms, it requires only the production of a signal molecule in the flagellum at a constant rate, a flagellar compartment that is separate from the cytoplasm, and degradation of the signal in the cytoplasm (Figure 4). This scenario resembles that of the Ran GTP gradient that regulates nuclear import. Ran, a GTPase, is converted to its excited state in the nucleus and exits the nucleus, where it degrades in the cytoplasm to the ground state (Becksei and Mattaj, 2003). The volume diffusion model proposes a similar scenario that agrees with data and intuition and resembles an already proven system. The mathematical form of the model could be derived in several ways, yielding slightly different slopes to the predicted curves. Here, I specify that the ciliary length is sensed as the concentration difference between the ciliary compartment and the cytoplasm, but in practice, it could be sensed in a variety of ways, including the absolute concentration in the compartment or the flux into the cytoplasm. Another part of the derivation that can be changed is how the RanGTP

is activated and how it degrades. Regardless of the specific assumptions, the overall trends of the model do not vary under these different derivations. The basic rule that as the volume of the organelle increases, its concentration of signal decreases holds under many different assumptions.

Dishinger *et al* (Dishinger et al., 2010) proposed that the ciliary import system works by the same basic molecular steps as the nuclear import signal, using a Ran-GTP gradient to facilitate flagellar entry of IFT particles. In light of the findings presented in Chapter 2, that signal would regulate IFT particle accumulation at the flagellar base in a length-dependent manner but could also license entry. Note that the complex dynamics reported in Chapter 2 would arise as an emergent property of the accumulating particles crowding for entry. The volume diffusion model thus meshes well with what cell biologists already know about how a cell works.

On a final note, the volume diffusion model has the additional appeal of being a more general measurement mechanism. Rather than measuring length specifically, it measures organelle volume. In the case of a linear organelle like the cilium, length is proportional to volume, but the model could equally measure an organelle like the nucleus, a vacuole or the irregularly-shaped endoplasmic reticulum. The generality of the model thus gives it potential for broad application and invites testing from outside the field of cilia.

Materials and methods

All simulations and analysis was done in MATLAB. Model selection was performed using custom-written code.

FRAP experiments

FRAP experiments were conducted on a Nikon ti2000 custom fitted by Andor with a Yokogawa CSU22 spinning disk and a separate bypassing FRAP laser. The laser launch and microscope software were custom Andor products at the Woods Hole Physiology course (Marine Biological Laboratories, Wood Hole, MA) in 2009.

Chlamydomonas reinhardtii strains used were a KAP-GFP rescue of the *fla3* strain (Mueller et al., 2005) and an IFT20-GFP rescue of an IFT20 Δ strain (Lehtreck et al., 2009). Cells were grown and imaged in standard liquid TAP media.

References

- Abdul-Majeed, S., and S.M. Nauli. 2011. Calcium-mediated mechanisms of cystic expansion. *Biochim Biophys Acta*. 1812:1281-1290.
- Akaike, H. 1974. A new look at the statistical model identification. *Automatic Control, IEEE Transactions on*. 19:716 - 723.
- Bak, P. 1996. How nature works: the science of self-organized criticality. Springer-Verlag, New York, NY.
- Beck, C., and R. Uhl. 1994. On the localization of voltage-sensitive calcium channels in the flagella of *Chlamydomonas reinhardtii*. *The Journal of Cell Biology*. 125:1119-1125.
- Becskei, A., and I.W. Mattaj. 2003. The strategy for coupling the RanGTP gradient to nuclear protein export. *Proc Natl Acad Sci USA*. 100:1717-1722.
- Besschetnova, T.Y., E. Kolpakova-Hart, Y. Guan, J. Zhou, B.R. Olsen, and J.V. Shah. 2010. Identification of Signaling Pathways Regulating Primary Cilium Length and Flow-Mediated Adaptation. *Current Biology*. 20:182-187.
- Dishinger, J.F., H.L. Kee, P.M. Jenkins, S. Fan, T.W. Hurd, J.W. Hammond, Y.N.-T. Truong, B. Margolis, J.R. Martens, and K.J. Verhey. 2010. Ciliary

entry of the kinesin-2 motor KIF17 is regulated by importin-beta2 and RanGTP. *Nat Cell Biol.* 12:703-710.

Engel, B.D., W.B. Ludington, and W.F. Marshall. 2009. Intraflagellar transport particle size scales inversely with flagellar length: revisiting the balance-point length control model. *J Cell Biol.* 187:81-89.

Huang, K., D.R. Diener, A. Mitchell, G.J. Pazour, G.B. Witman, and J.L. Rosenbaum. 2007. Function and dynamics of PKD2 in *Chlamydomonas reinhardtii* flagella. *J Cell Biol.* 179:501-514.

Johnson, K.A., and J.L. Rosenbaum. 1993. Flagellar regeneration in *Chlamydomonas*: a model system for studying organelle assembly. *Trends Cell Biol.* 3:156-161.

Lehtreck, K.-F., E.C. Johnson, T. Sakai, D. Cochran, B.A. Ballif, J. Rush, G.J. Pazour, M. Ikebe, and G.B. Witman. 2009. The *Chlamydomonas reinhardtii* BBSome is an IFT cargo required for export of specific signaling proteins from flagella. *J Cell Biol.* 187:1117-1132.

Lefebvre, P. 2009. Flagellar length control. *In* The *Chlamydomonas* Sourcebook: Cell motility and Behavior. Vol. 3. G.B. Witman, editor. Academic Press, Elsevier, Oxford. 115-129.

Levy, E. 1974. Flagellar elongation as a moving boundary problem. *Bulletin of Mathematical Biology.*

- Marshall, W. 2004. CELLULAR LENGTH CONTROL SYSTEMS. *Annual Review of Cell and Developmental Biology*.
- Marshall, W., and J. Rosenbaum. 2001. Intraflagellar transport balances continuous turnover of outer doublet microtubules: implications for flagellar length control. *Journal of Cell Biology*. 155:405-414.
- Marshall, W.F., H. Qin, M. Rodrigo Brenni, and J.L. Rosenbaum. 2005. Flagellar length control system: testing a simple model based on intraflagellar transport and turnover. *Mol Biol Cell*. 16:270-278.
- Mueller, J., C.A. Perrone, R. Bower, D.G. Cole, and M.E. Porter. 2005. The FLA3 KAP subunit is required for localization of kinesin-2 to the site of flagellar assembly and processive anterograde intraflagellar transport. *Mol Biol Cell*. 16:1341-1354.
- Pazour, G.J., B.L. Dickert, Y. Vucica, E.S. Seeley, J.L. Rosenbaum, G.B. Witman, and D.G. Cole. 2000. Chlamydomonas IFT88 and its mouse homologue, polycystic kidney disease gene *tg737*, are required for assembly of cilia and flagella. *J Cell Biol*. 151:709-718.
- Rosenbaum, J. 2003. Organelle size regulation: length matters. *Curr Biol*. 13:R506-507.

Figures

Figure 1: model fits to IFT injection data and model selection scores indicate the diffusion models to be the best.

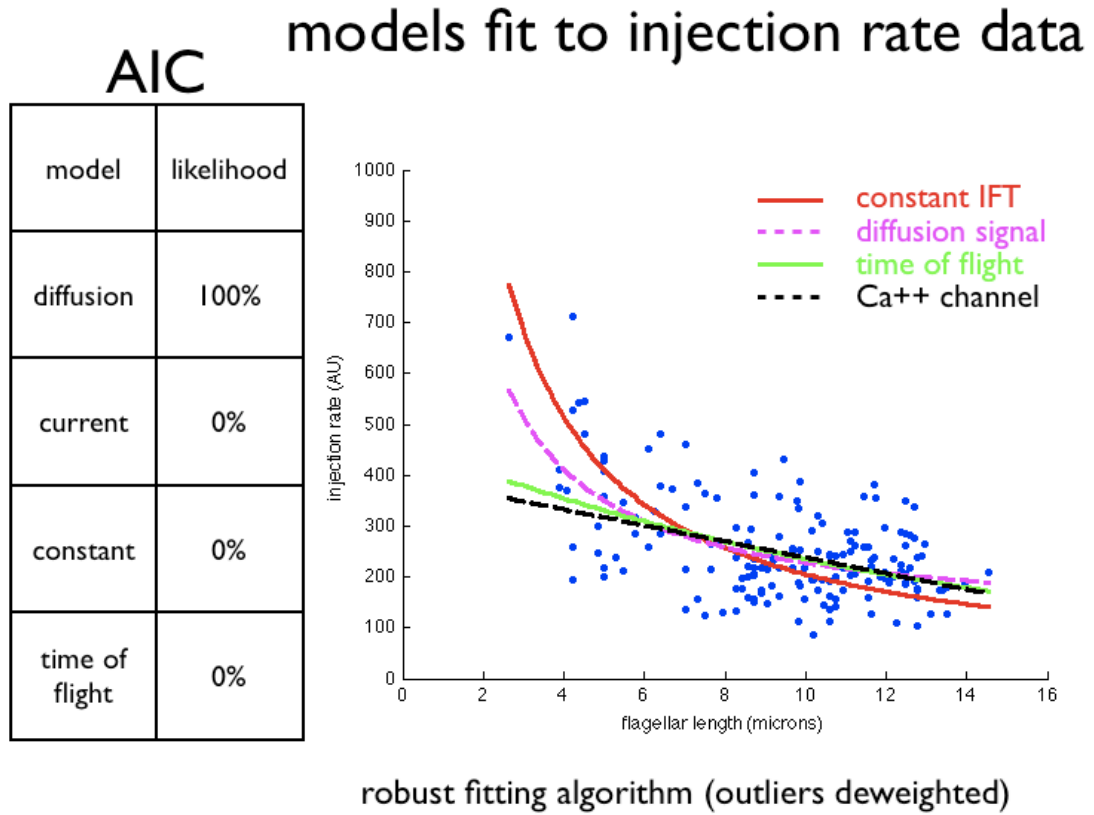
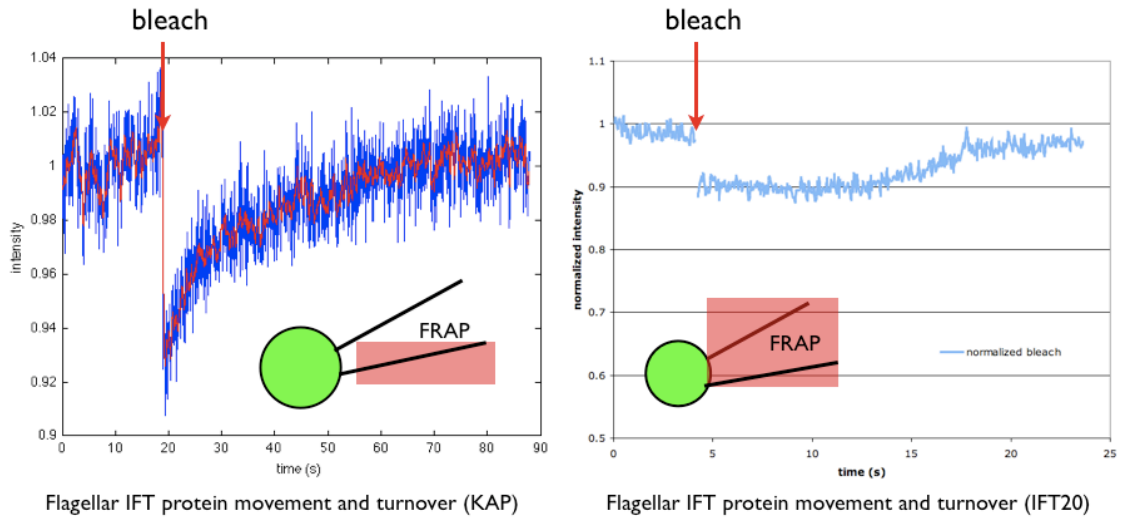


Figure 2: FRAP of IFT proteins reveals turnover at different rates for different proteins



1. flagella recover full fluorescence of IFT proteins
2. extensive turnover occurs with the cytoplasm

Figure 3: model best fits to total IFT data and model selection indicate the diffusion models to be the best

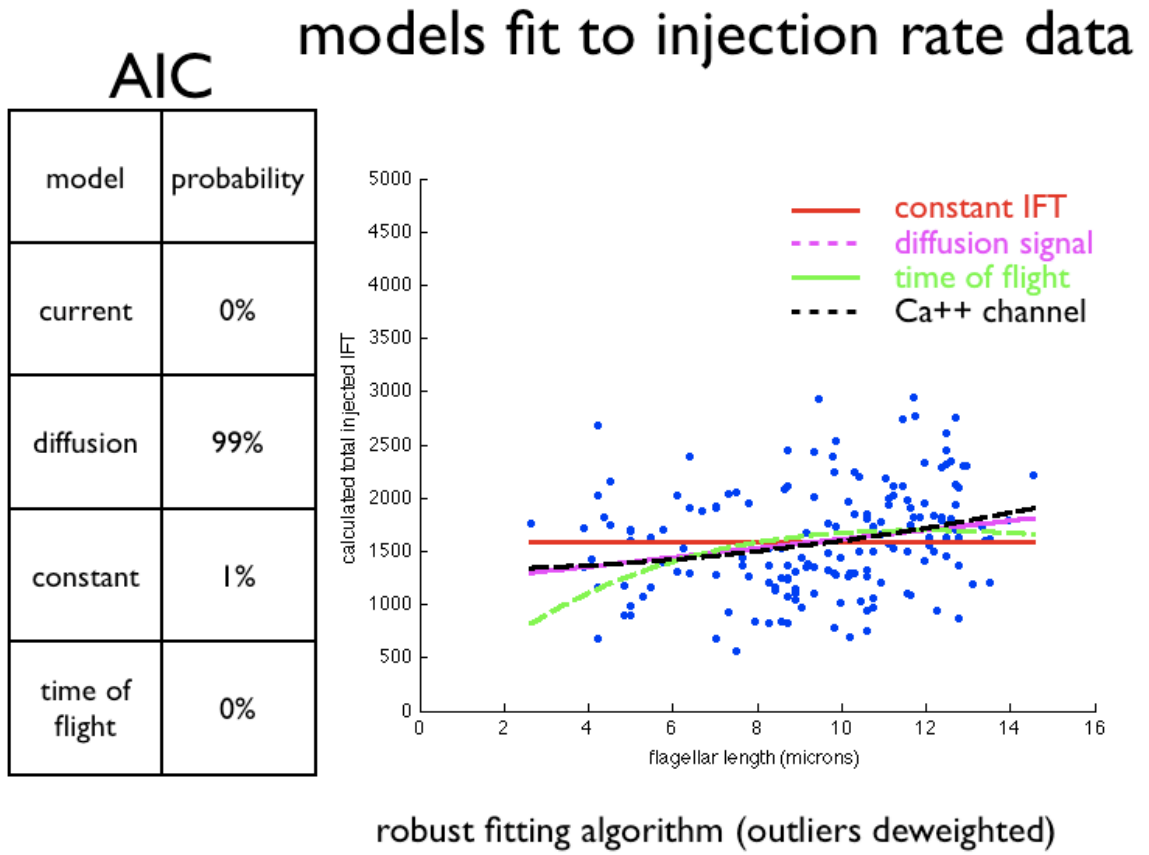
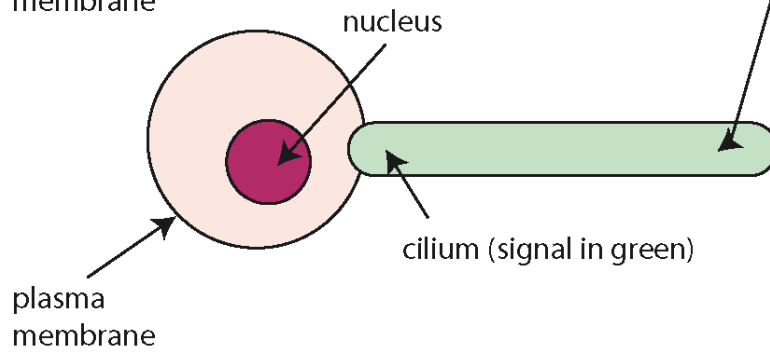
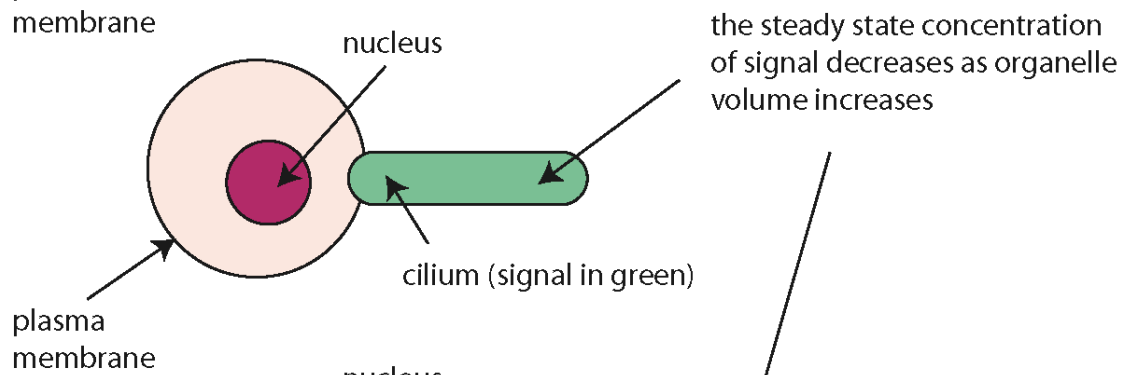
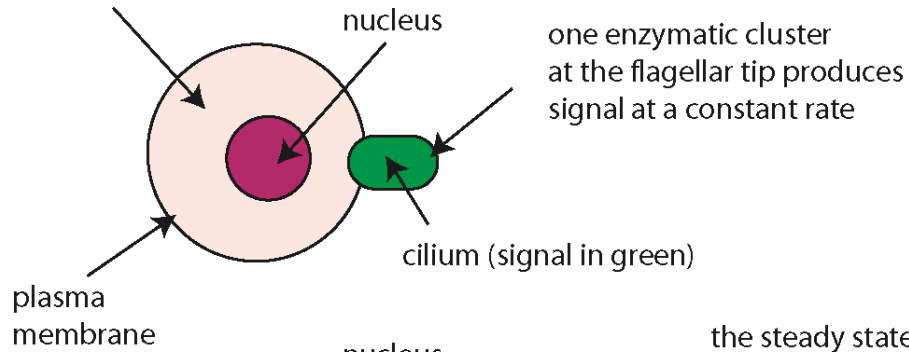


Figure 4: cartoon of the volumetric diffusion model

cytoplasm serves as a sink for the signal















Tables

Table 1

Models:	IFT injection rate vs length	total IFT vs length	length-determining mechanism
linear diffusion	$\frac{k_1}{L} + k_2$	$k_1 + k_2L + k_3$	slope of diffusion gradient
volume diffusion	$\frac{k_1}{k_2 + L}$	$\frac{k_1L}{k_2 + L} + k_3$	Δ conc between flagellum and cytoplasm
time of flight	$k_1e^{-k_2L}$	$k_1Le^{-k_2L} + k_3$	excitation state of exiting signal molecules
ion channels	$k_1 - k_2L$	$k_1L - k_2L^2 + k_3$	amount of current flow
constant injection	k_1	$k_1L + k_2$	nothing
initial bolus	$\frac{k_1}{L}$	k_1	density of IFT

Table 2: same as Table 1 but with the characteristic shapes of the curves drawn

Models:	IFT injection rate vs length	total IFT vs length	length-determining mechanism
linear diffusion			slope of diffusion gradient
volume diffusion			Δ conc between flagellum and cytoplasm
time of flight			excitation state of exiting signal molecules
ion channels			amount of current flow
constant injection			nothing
initial bolus			density of IFT

Appendix 1

**Changes in IFT speed do not
affect flagellar length control**

IFT speed does not affect the arrival rate of material at the flagellar tip

As a matter of clarity, I would like to address an issue that has caused some confusion in the recent literature. Many papers are now coming out quantifying changes in intraflagellar transport speed as it relates to ciliary length defects and human disease. I will not cite examples out of respect, but a simple search on Pubmed will affirm this fact for the reader. Here, I briefly explain why IFT speed is a meaningless parameter to quantify in terms of ciliary length control if the size and frequency of IFT are not quantified simultaneously.

The “balance-point” model shows that the ciliary [or flagellar] length is stable when the growth rate is exactly offset by the shortening rate (Marshall and Rosenbaum, 2001; Marshall et al., 2005). Since the shortening rate is length-independent, the cell can control ciliary length by modulating the growth rate. The amount of cargo transport by the IFT machinery controls this growth rate in a length-dependent manner (*see* Chapter 3).

It has previously been established that the growth rate of the flagellum is determined by the amount of flagellar precursor available for incorporation at the flagellar tip (Rosenbaum et al., 1969). A higher IFT injection rate delivers more material to the tip and must take into account the frequency as well as the size of injections in order to determine the amount of material per unit time that arrives at the flagellar tip. The speed of transport does not affect this number so long as it does not vary significantly between injections, which it does not, and so long as injections occur frequently enough so that the flagellum is continually occupied with IFT material in transit, which they do.

To explain my argument for why this is the case, consider two identical conveyor belts 10 meters long, side-by-side, one moving at high speed (2 m/s) and the other at lower speed (1 m/s). These will represent our flagella, one with fast IFT, and one with slow IFT. If particulate material is loaded at a set rate (1 piece/s) onto both the conveyor belts, once the belts are fully loaded (i.e. the belts are running and the material has been loading for more than 10 seconds), the arrival rate of material at the end of the two conveyor belts will be equal to the loading rate (1 piece/s). The speed will not affect the arrival rate. Only the loading rate affects the arrival rate. However, the distance between the particulates on the belts will be twice as long (2 m vs. 1 m) on the faster conveyor versus the slower one, and the transit time will be twice as long for the slower conveyor (10 s vs. 5 s). These attributes will be readily apparent to the investigator, but they will not make a difference to the growth rate of the flagellum unless they are extreme. In the extreme case of slow transport, IFT particles would become clogged in the flagellum and fail to reach the tip due to traffic jams inside the flagellum. Indeed, certain IFT mutants, such as cytoplasmic dynein, the retrograde motor, cause a phenotype of flagella swollen with IFT particles (Pazour et al., 1999).

An exception where the IFT speed would matter comes in the theoretical case of the “time of flight” model (Lefebvre, 2009), whereby the cell is postulated to measure ciliary length based on the transit time of individual IFT proteins.

Though a beautiful model, it has not found support from empirical data.

Therefore, in attempting to quantify changes in IFT, investigators should take care to measure both the size and the frequency of IFT injections rather than the speed.

Speed defects may be indicative of other anomalies in the IFT machinery, such as the ability to bind cargo, however, on their own, they should not cause a change in ciliar length except in extreme cases as mentioned. The point is not that IFT speed does not matter but that IFT speed matters only in the context of the IFT injection rate, which takes into account IFT size and IFT frequency.

References

- Lefebvre, P. 2009. Flagellar length control. *In* The Chlamydomonas Sourcebook: Cell motility and Behavior. Vol. 3. G.B. Witman, editor. Academic Press, Elsevier, Oxford. 115-129.
- Marshall, W., and J. Rosenbaum. 2001. Intraflagellar transport balances continuous turnover of outer doublet microtubules: implications for flagellar length control. *Journal of Cell Biology*. 155:405-414.
- Marshall, W.F., H. Qin, M. Rodrigo Brenni, and J.L. Rosenbaum. 2005. Flagellar length control system: testing a simple model based on intraflagellar transport and turnover. *Mol Biol Cell*. 16:270-278.
- Pazour, G.J., B.L. Dickert, and G.B. Witman. 1999. The DHC1b (DHC2) isoform of cytoplasmic dynein is required for flagellar assembly. *J Cell Biol*. 144:473-481.
- Rosenbaum, J.L., J.E. Moulder, and D.L. Ringo. 1969. Flagellar elongation and shortening in Chlamydomonas. The use of cycloheximide and colchicine to study the synthesis and assembly of flagellar proteins. *J Cell Biol*. 41:600-619.

Publishing Agreement

It is the policy of the University to encourage the distribution of all theses, dissertations, and manuscripts. Copies of all UCSF theses, dissertations, and manuscripts will be routed to the library via the Graduate Division. The library will make all theses, dissertations, and manuscripts accessible to the public and will preserve these to the best of their abilities, in perpetuity.

Please sign the following statement:

I hereby grant permission to the Graduate Division of the University of California, San Francisco to release copies of my thesis, dissertation, or manuscript to the Campus Library to provide access and preservation, in whole or in part, in perpetuity.



Author Signature

12/21/2011
Date